HAL
open science

A time dependent search for neutrino emission from microquasars with the ANTARES telescope

Salvatore Galata

To cite this version:

Salvatore Galata. A time dependent search for neutrino emission from microquasars with the ANTARES telescope. Instrumentation and Methods for Astrophysic [astro-ph.IM]. Aix-Marseille Université, 2012. English. NNT : . tel-00782883

HAL Id: tel-00782883

https://theses.hal.science/tel-00782883

Submitted on 1 Feb 2013

HAL is a multi-disciplinary open access archive for the deposit and dissemination of scientific research documents, whether they are published or not. The documents may come from teaching and research institutions in France or abroad, or from public or private research centers.

L'archive ouverte pluridisciplinaire **HAL**, est destinée au dépôt et à la diffusion de documents scientifiques de niveau recherche, publiés ou non, émanant des établissements d'enseignement et de recherche français ou étrangers, des laboratoires publics ou privés.

Aix-Marseille Université

Ecole Doctorale: Physique et Sciences de la Matière

Spécialité: Physique des Particules et Astroparticules

Thèse de Doctorat

présentée par:

Salvatore Galatà

A time dependent search for neutrino emission from microquasars with the ANTARES telescope

soutenue le 5 Avril 2012, devant le jury composé de:

M. John Carr	(directeur de thèse)
M. Damien Dornic	(examinateur)
M. Guillaume Dubus	(examinateur)
M. Jürgen Knödlseder	(rapporteur)
M. Antoine Kouchner	(rapporteur)
M. Mossadek Talby	(président)

to my family

Résumé

La Collaboration ANTARES exploite actuellement un détecteur sous-marin Cherenkov dédié à l'astronomie neutrino de haute énergie. Le but principal de cette expérience est de détecter les sources cosmiques de neutrinos, afin de révéler les sites de production des rayons cosmiques. Parmi les sources candidates figurent celles où a lieu l'accélération de ces rayons cosmiques dans les jets relativistes, comme les noyaux actifs de galaxie, les sursauts gamma et les microquasars.

Les microquasars sont des systèmes stellaires binaires formés par un objet compact accrétant la matière d'une étoile compagnon. Ce transfert de masse est responsable de l'émission de rayons X, tandis que les forces magnétiques du plasma d'accrétion peuvent causer la création de jets relativistes qui sont observés par des télescopes radio grâce au rayonnement synchrotron non thermique émis par les particules chargées accélérées dans ces jets. Dans certains systèmes, la corrélation entre les courbes de lumière des rayons X et les courbes radio indique une interaction forte entre accrétion et éjection. Certains microquasars émettent également des rayons gamma de haute et très haute énergie (jusqu'à quelques dizaines de TeV).

Dans ce travail de thèse, une recherche d'émission de neutrinos provenant de microquasars a été conduite avec une approche multi-messager (photon/neutrino). Les données des satellites RXTE/ASM et SWIFT/BAT, ainsi que du télescope gamma FERMI/LAT ont été étudiées afin de sélectionner les périodes dans lesquelles se produisent les jets relativistes. La restriction de l'analyse des neutrinos aux phases d'éjection permet de réduire drastiquement le bruit de fond de neutrinos et de muons atmosphériques et ainsi d'augmenter les chances de découverte d'une source cosmique de neutrinos.

Les recherches ont été effectuées à partir des données ANTARES obtenues entre 2007 et 2010. Une analyse statistique a été faite en utilisant une méthode "unbinned" basée sur le test du rapport de vraisemblance. Les coupures de sélection des évènements ont été optimisées à partir de simulations Monte Carlo afin de maximiser les chances de découverte. Comme aucun signal de neutrinos n'a été observé en corrélation avec ces microquasars, des limites supérieures sur les flux de neutrinos produits dans ces microquasars ont été calculées et confrontées avec des modèles de production de neutrino dans ces objets.

Abstract

The ANTARES collaboration has successfully built, deployed and is currently operating an underwater Cherenkov detector dedicated to high energy neutrino astronomy. The primary aim of the experiment is to detect cosmic sources of neutrinos in order to reveal the production sites of cosmic rays. Among the sources likely to be significant sources of neutrinos are those accelerating relativistic jets, like gamma ray bursts, active galactic nuclei and microquasars.

Microquasars are binary systems formed by a compact object accreting mass from a companion star. The mass transfer causes the emission of X-rays, whereas the onset of magnetic forces in the accreting plasma can cause the acceleration of relativistic jets, which are observed by radio telescopes via their non-thermal synchrotron emission. In some systems, a correlation between X-ray and radio light curves indicates an interplay between accretion and ejection respectively. Some microquasars are also high energy and very high energy gamma ray emitters.

In this thesis, a time dependent search for neutrino emission from microquasars was performed with a multi-messenger approach (photon/neutrino). The data from the X-ray monitors RXTE/ASM and SWIFT/BAT, and the gamma-ray telescope FERMI/LAT were used to select transient events in which the source was supposed to accelerate relativistic jets. The restriction of the analysis to the ejection periods allows a drastic reduction of atmospheric muon and neutrino background, and thus to increase the chances of a discovery.

The search was performed with the ANTARES data taken between 2007 and 2010. Statistical analysis was carried out using an unbinned likelihood method based on a likelihood ratio test. The cuts for the event selection were optimized in order to maximize the chance of a discovery. As no neutrino signal was observed in correlation with these microquasars, upper limits on the neutrino fluxes of the microquasars under study were calculated and compared with some models of neutrino production in these objects.

Contents

Résumé **v**

Abstract **vii**

Introduction **1**

1 High energy neutrino astronomy **3**
1.1 Cosmic rays . . . 3
1.1.1 Energy spectrum . . . 5
1.1.2 Composition of the cosmic ray flux . . . 6
1.1.3 Anisotropy at ultra high energy . . . 7
1.1.4 Fermi acceleration mechanism . . . 8
1.2 Astrophysical neutrinos . . . 9
1.2.1 Candidate sources . . . 10

2 Cherenkov neutrino telescopes and the ANTARES detector **13**
2.1 Detection principle . . . 13
2.1.1 Neutrino interaction . . . 14
2.1.2 Muon propagation in water . . . 16
2.1.3 Cherenkov radiation . . . 17
2.1.4 Light propagation in water . . . 17
2.1.5 Sources of background . . . 18
2.2 Neutrino telescopes . . . 20
2.2.1 Baikal . . . 20
2.2.2 IceCube . . . 21
2.3 The ANTARES detector . . . 22
2.3.1 Data acquisition system . . . 23
2.3.2 Clock system and timing calibration . . . 24
2.3.3 Positioning system . . . 26
2.3.4 Charge calibration . . . 27
2.3.5 Detector status and operation . . . 28
2.3.6 Selected physics results of ANTARES . . . 30
2.3.7 The KM3NeT project . . . 33

3 Simulation tools and muon track reconstruction in ANTARES **37**
3.1 Monte-Carlo simulation . . . 37
3.1.1 Muon neutrino generation . . . 37

3.1.2 Atmospheric muons generation . . . 38
3.1.3 Photon generation, propagation and detection . . . 39
3.1.4 Front-end electronics and trigger simulation . . . 42
3.1.5 Generation of the optical background . . . 42
3.2 Muon track reconstruction . . . 42
3.2.1 Maximum likelihood algorithm . . . 44
3.2.2 Online reconstruction (`BBfit`) . . . 47
3.3 The new software framework . . . 50
3.3.1 Implementation of `BBfit` in the framework . . . 52
3.3.2 Conclusions . . . 56

4 Microquasars 59
4.1 Classification and main properties . . . 59
4.2 Accretion process and X-ray emission . . . 62
4.2.1 Mechanisms of mass transfer . . . 62
4.2.2 Disc formation and radiation . . . 64
4.3 Other contributions to the X-ray spectrum . . . 65
4.3.1 Comptonization . . . 65
4.3.2 Reflection . . . 66
4.4 Relativistic jets . . . 66
4.4.1 Synchrotron emission . . . 66
4.4.2 Jet speeds and apparent superluminal motions . . . 67
4.4.3 Jet acceleration and collimation . . . 69
4.4.4 Jet composition . . . 70
4.5 X-ray spectral states and disc-jet coupling . . . 70
4.5.1 In black hole binaries . . . 70
4.5.2 In neutron star binaries . . . 72
4.6 HE and VHE γ-ray emission from microquasars . . . 73
4.7 Models for neutrino production . . . 74
4.7.1 Neutrinos from the jets . . . 74
4.7.2 Neutrinos from wind-jet interactions in HMXBs . . . 74

5 Multi-wavelength study 77
5.1 Detectors used . . . 78
5.1.1 Rossi X-ray Tming Explorer - All Sky Monitor . . . 78
5.1.2 Swift - Burst Alert Telescope . . . 78
5.1.3 Fermi - Large Area Telescope . . . 78
5.2 Outburst selection using X-rays . . . 80
5.2.1 Cir X-1 . . . 85
5.2.2 GX 339−4 . . . 88
5.2.3 H1743−322 . . . 91
5.2.4 IGR J17091−3624 . . . 92
5.2.5 Cyg X-1 . . . 92
5.3 Outburst selection for Cyg X-3 using γ-rays . . . 95
5.3.1 Analysis of Fermi/LAT data . . . 95
5.3.2 Outburst selection . . . 96

6 Analysis of the ANTARES data **99**
6.1 ANTARES Data processing 99
6.1.1 Selection of the data set 99
6.1.2 Track reconstruction and event selection 101
6.2 Data - Monte Carlo comparison 102
6.3 Unbinned search method 107
6.3.1 Pseudo-experiment generation 110
6.3.2 Neutrino flux calculation 113
6.3.3 Discovery potential and choice of the cut on Λ 115
6.3.4 Limit setting method 116
6.4 Results of the data unblinding 118
6.5 Sensitivity expectations for KM3NeT 123

Summary and conclusions **127**

Acknowledgements **139**

Introduction

After a century since their discovery, Cosmic Rays are still one of the unsolved problems in physics, since neither their production sites nor the acceleration mechanisms are known. Their energy spectrum extends up to ultra high energies (UHE, $>5\times10^{19}$ eV), suggesting that they could originate in the most extreme cosmic environments. The techniques developed to study the "high energy" universe involve the detection of cosmic rays, gamma rays and neutrinos, all complementary in order to understand the origin of cosmic rays. In the domain of UHE cosmic rays, important results have been recently obtained by extensive air shower experiments. Taking into account the confirmed suppression of the cosmic ray flux above the energy of the GZK[1] cutoff, the observed anisotropy of the arrival directions of UHE cosmic rays could be related to the inhomogeneous distribution of matter within the "GZK horizon". The detection of TeV gamma ray sources by the last generation of Imaging Atmospheric-Cherenkov Telescopes has opened up a previously unexplored window on the very high energy universe. More than 100 sources are currently registered in the TeV catalogue, although it cannot be established yet whether part of their radiation is of hadronic origin. The discrepancies between leptonic and hadronic models are expected to be more evident at low energies and can be tested by high energy gamma ray telescopes. In this framework, the contribution of high energy neutrino astronomy would be of crucial importance, since the detection of a cosmic neutrino source would be an unambiguous proof of cosmic ray acceleration in dense environments.

The challenge of detecting sources of high energy neutrinos lies in the low cross section of charged current interactions, the low expected fluxes from cosmic sources and the irreducible background constituted by atmospheric neutrinos. A neutrino telescope must thus meet the requirements to offer a sufficiently high effective area of detection, which must be $>$0.1-1 km^2, and the highest possible screening from the intense flux of atmospheric muons. These requirements are met by placing the detector under a thick layer of water or ice, in a way to reduce the atmospheric muon flux from above. This allows the detection of neutrinos by looking at upgoing tracks, the atmospheric muons being completely absorbed by the Earth in that direction. Moreover, placing the detection units in natural environments like seawater or the ice in Antarctica allows huge sensitive volumes to be reached at (relatively) reduced costs. At present, the two neutrino telescopes IceCube, at the South Pole, and ANTARES, in the Mediterranean Sea, are setting the most stringent upper limits on the fluxes of possible neutrino sources, in the northern and in the southern sky

[1]From the physicists Greisen (1966), Zatsepin and Kuzmin (1966) who first theorized it.

respectively.

The ANTARES telescope was completed in 2008 and is currently taking data in its full configuration comprising 12 detection lines of 380 m height, each equipped with 75 optical sensors. It is situated offshore the French coast, on a plateau at 2475 m depth. Physics data taking started earlier in 2007, when the detector was composed of only 5 lines.

This work presents a search for neutrino emission from microquasars with ANTARES. Microquasars are galactic X-ray binaries in which a compact object drives the accretion of matter from a companion star. The gravitational energy of the infalling matter can be converted and released in the form of relativistic jets, observed via their non-thermal synchrotron emission by ground based radio telescopes. The broad band electromagnetic emission from these sources, which spans from radio to gamma rays, is subject to time variability, with periods of quiescence alternated with luminous outbursts. The X-ray and the radio emission, which are related to the accretion and ejection respectively, are shown by simultaneous observations to be correlated. The acceleration of relativistic particles in the jets is of particular interest for neutrino astronomy since a component of hadrons could also be accelerated.

The search for neutrino emission from these sources has been performed using a multi-messenger approach. The data from the X-ray monitors RXTE/ASM and SWIFT/BAT, and the gamma ray telescope FERMI/LAT have been used together with detailed X-ray and radio observations found in the literature, in order to select the time periods when the microquasars were expected to accelerate relativistic jets. The neutrino search in the ANTARES data was then restricted to those times, hence reducing the background and increasing the chances of a discovery.

This thesis is organized in 6 chapters. The main motivations for neutrino astronomy, the possible mechanism of neutrino production in astrophysical sources and the classes of candidate sources are described in the first chapter. Chapter two is focused on the detection of neutrinos by means of underwater/ice Cherenkov telescopes and on the physics governing the detection principle. Also in this chapter, the main technical features of the ANTARES telescope are described. The third chapter describes the software tools used in the ANTARES collaboration for the Monte Carlo simulation and the data analysis. The features of microquasars, the main mechanisms driving their electromagnetic emission and the coupling between different bands are presented in chapter four, together with the models describing the neutrino production from these sources. Chapter five presents a multi-wavelength (X-rays, gamma) study aimed to select a list of candidate microquasars for the neutrino search and the time periods used for the neutrino search. The analysis of the ANTARES data is presented in chapter six. In this last chapter the data reduction and processing are described, as well as the optimization of the quality cuts, the statistical method used in the search and the final results. Conclusions are drawn in the last section.

Chapter 1

High energy neutrino astronomy

1.1 Cosmic rays

Cosmic rays have been puzzling physics for almost a century since their discovery by Victor Hess in 1912 (Hess, 1912). By means of aerostatic balloons equipped with Wulf electrometers Hess found that the amount of ionizing radiation in the atmosphere up to 5000m increased with the altitude. An analogous result had been obtained by Wulf two years before, when he measured a level of radiation at the top of the Eiffel Tower higher than that at the bottom.

This discovery gave a strong stimulus to research in this new field, notably with the campaigns of experiments with aerostatic balloons conducted by Millikan and Compton, which represented the first systematic studies of the nature of the cosmic radiation. A crucial experiment towards this goal was that of Bothe and Kolhörster in 1929, who measured the rate of coincidences between two Geiger counters separated by a thick absorber of lead and gold. The high rate observed suggested that the penetrating radiation could not be composed of γ's, as was thought, but of charged particles able to penetrate the absorber. The nature of the primary radiation was revealed with the experiments by Schein et al. (1941), who discovered that the charged primary particles were mostly protons, and by Bradt et al. (1948), who first detected high-Z nuclei in the cosmic radiation by measuring their stopping power in photographic emulsions.

In 1938 Pierre Auger conducted the first experiments on atmospheric showers, by measuring the rate of coincidences of cosmic rays at different distances up to 300 m. From the data he collected, he estimated that the energy of the primary particles generating the showers had to be of the order of 10^{15} eV (Auger et al., 1939). Since the 1960s, the extensive air shower technique has been used to study cosmic rays at the highest energies. This enabled the detection of the first shower with an energy of 10^{20} eV with the MIT Volcano Ranch station, an air shower detector equipped with scintillation counters (Linsley, 1963). Other extensive air shower detectors were built more recently to investigate the cosmic ray flux at energies beyond 10^{18} eV.

In the first decades after their discovery, mainly between the 1930s and the 1950s, Cosmic Rays were used as an indirect mean to discover new particles, such as the positron, the pion and the muon, and they allowed the observation of the first decays of strange particles.

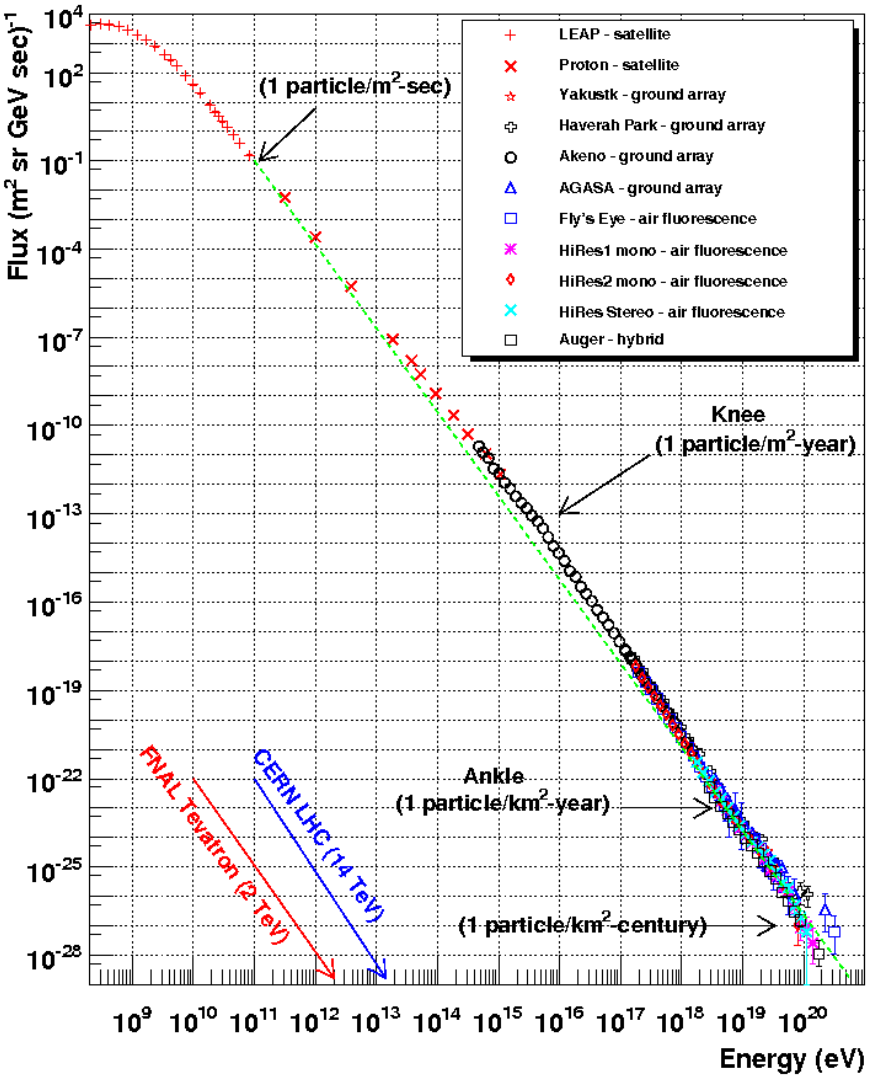

Figure 1.1: *Cosmic ray energy spectra compiled from various experiments. From (Hanlon, 2008).*

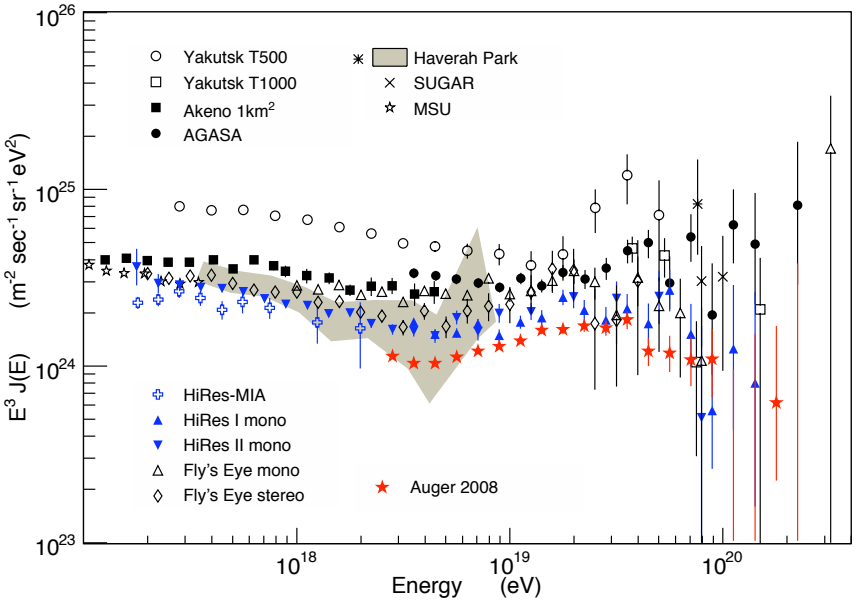

Figure 1.2: *Measured flux of UHE cosmic rays compiled from various experiments. The flux is multiplied by E^3. From (Blümer et al., 2009).*

1.1.1 Energy spectrum

The energy spectrum of cosmic rays (Figure 1.1) spans about 12 orders of magnitude in energy, up to 10^{20} eV, and about 32 orders of magnitude in flux, up to a few particles per km^2 per century at the highest energies. At low energies, up to ~ 1 GeV, the flux is strongly modulated by the solar wind. At higher energies the inclusive spectrum is well approximated by a power law:

$$\frac{dN}{dE} \propto E^{-\gamma} \tag{1.1}$$

with the spectral index γ varying between 2.7 and 3. In more detail, a spectral index $\gamma = 2.7$ well reproduces the spectrum up to $\sim 10^{15}$ eV. At this energy, the so called *knee*, the spectrum becomes steeper with a spectral index $\gamma = 3$ and the composition of the cosmic rays becomes less rich in protons in favour of heavier elements. The steepening of the spectrum at the knee is explained in different ways in the literature (Hörandel, 2004). Some models relate the knee to the maximum energy attainable in the acceleration process, for example in supernova explosions, others to the leakage of cosmic rays from the Galaxy. At energies above 5×10^{18} eV the spectral index changes again to a value ~ 2.7, the so called *ankle*, and the composition becomes proton dominated. At these energies the Larmor radius of protons in the galactic magnetic field is of the order of 1 kpc, which is larger that the thickness of the galaxy. Protons above the ankle are thus thought to be of extragalactic origin.

Greisen (1966), Zatsepin and Kuzmin (1966) (GZK) first theorized that the spectrum of cosmic rays should be suppressed above 5×10^{19} eV due to the interaction of the primaries with the cosmic microwave background radiation during their propagation. The GZK cutoff has been studied by various extensive air shower experiments. Figure 1.2 shows a compilation of results for the spectrum of the cosmic rays in

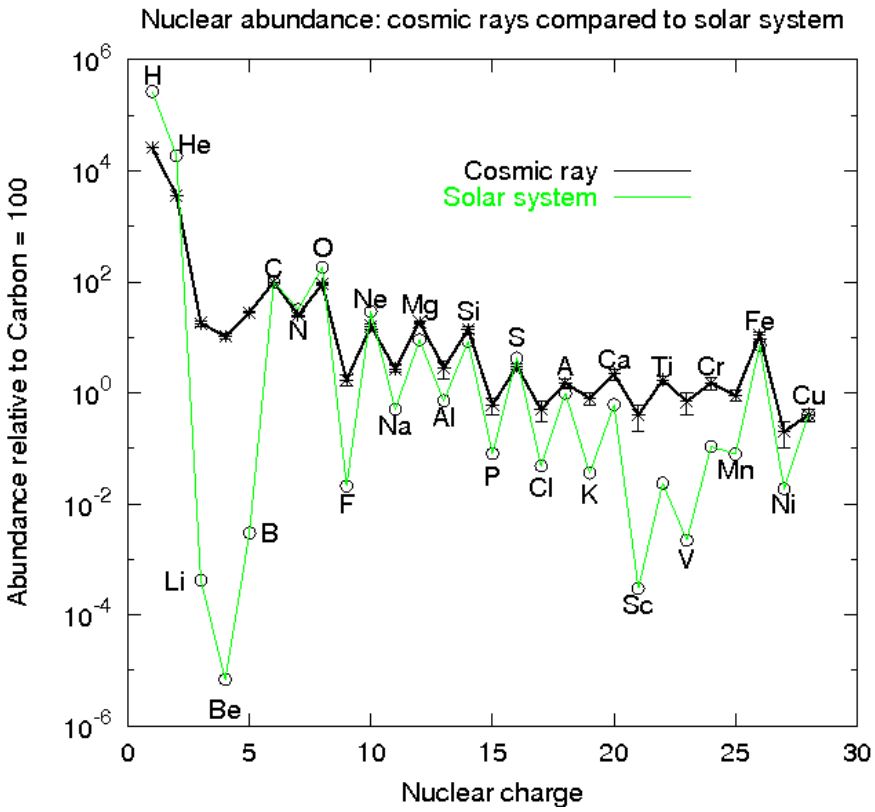

Figure 1.3: *Cosmic ray abundances relative to carbon (Simpson, 1983).*

the ultra high energy regime. Results from AGASA seem compatible with a non-suppression of the cosmic ray flux at the GZK energy, whereas a cutoff is observed by Auger and HiRes (Abraham et al., 2008; Bergman et al., 2007).

An alternative explanation to the GZK cutoff relates it to the maximum energy that can be reached at the accelerating sources.

1.1.2 Composition of the cosmic ray flux

The flux of cosmic rays is mostly composed of hadrons, with 98% of the total, with electrons and positrons the remaining 2%. The hadronic component is, in turn, composed of 87% by protons, 12% by He and the remaining 1% by heavier nuclei.

Figure 1.3 shows the elemental abundances in the cosmic radiation compared with those in the solar system (measured outside the heliosphere). The overabundances in cosmic rays of secondary nuclei like lithium, beryllium and boron, as well as of other elements lighter than iron, are due to spallation, i.e. the production of lighter elements due to the interaction of the primary with the interstellar medium.

The abundances of these secondary cosmic rays allow an estimation of the distance travelled before reaching the Earth. From the knowledge of the spallation cross section and the ratio between primaries and secondaries, an average travel path of $\sim$ 10-15 g/cm^2 is obtained at a rigidity of 4 GV. Assuming a density of one particle per cm^3 in the galaxy, this translates to a travelled distance of 1000 kpc. The travel path is also observed to diminish as the energy increases, meaning that

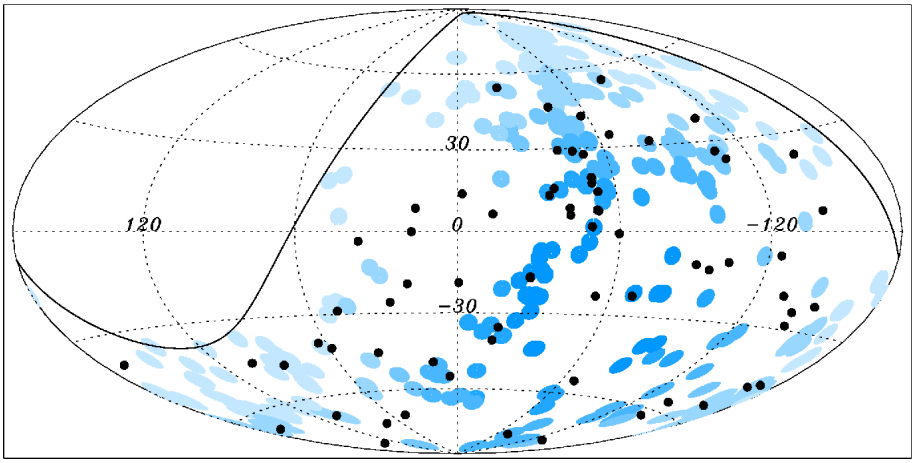

Figure 1.4: *Sky map in galactic coordinates of the arrival direction of the cosmic rays with* $E \geq 55 \cdot 10^{18}$ eV *detected by Auger up to 2009 (black dots) compared with the positions of the AGNs in the Véron-Cetty et al. (2006) catalogue, that are within 75 Mpc from Earth and in the field of view of the detector (blue circles, 3.1° each). The arrival directions of the UHE cosmic rays slightly correlate with the positions of the AGNs in the catalogue and are consistent for being non-isotropic.*

the acceleration phase takes place before the propagation, whereas if they were simultaneous the ratio between primaries and secondaries should not vary with the energy.

1.1.3 Anisotropy at ultra high energy

The trajectory of charged cosmic rays during their travel to Earth is perturbed by the galactic and extragalactic magnetic fields, as a consequence their direction of arrival at Earth cannot be used to point back the source. The only exception applies to the ultra high energy (UHE) cosmic rays with energies $\sim 10^{20}$ eV, for which the deviation angle is estimated to be $\lesssim 1°$, for protons coming from nearby galaxies, assuming an intergalactic magnetic field of 1 nG (Stanev et al., 2000). But at these energy regimes the flux of cosmic rays is expected to drop due to the GZK cutoff.

The Pierre Auger Collaboration has put in evidence the anisotropy of the directions of arrival of UHE cosmic rays. This was done by correlating of the arrival directions with the positions of the AGNs in the catalogue of Véron-Cetty et al. (2006). A $68\%^{+11}_{-13}$ correlation was found using a set of 27 UHE cosmic rays, whereas with an updated data set of 69 events, the correlation decreased to $38\%^{+11}_{-13}$ (Abreu et al., 2010). The expected correlation for an isotropic flux is 21%. Anisotropy in the arrival directions of UHE cosmic rays may reflect the non-isotropic distribution of matter within the "GZK horizon" and is an important step in the quest for the origin of cosmic rays. The sky map of the detected events and the positions of the considered AGNs are shown in Figure 1.4.

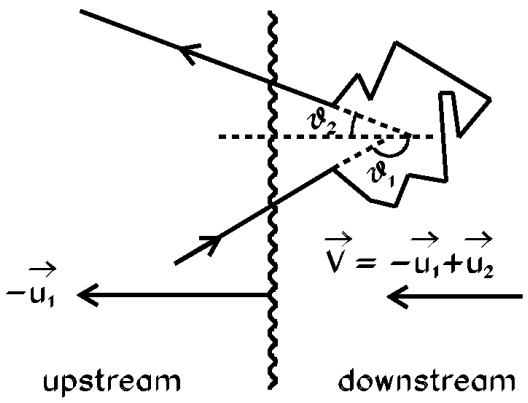

Figure 1.5: *Plane shock for the first order Fermi acceleration. The shock front propagates to the left towards the unshocked upstream gas.*

1.1.4 Fermi acceleration mechanism

One of the main issues related to the observation of high energy and ultra high energy cosmic rays concerns the acceleration mechanisms by which such energies can be reached. A first model to describe cosmic ray acceleration was presented by Fermi (1949). In its original version, particles were supposed to be accelerated by stochastic collisions with magnetized gas clouds moving in the interstellar medium. This model, though, could not easily explain the observed spectrum of cosmic rays and has been adapted by other authors (Longair, 1992) to the case of shocks.

The shock acceleration mechanism, also known as *first order Fermi acceleration*, succeeds in reproducing the expected energy spectrum of cosmic rays at the source. It supposes that in the acceleration region a plasma is expanding at supersonic velocity sweeping up some yet unshocked material, as in Figure 1.5. If the shock front propagates at a speed $-u_1$ and the shocked gas (downstream) follows it at a speed V, in the frame where the shock front is at rest the velocity of the unshocked (upstream) gas is u_1 and that of the downstream is $u_2 = V + u_1$. From the kinetic theory of gases, in the case of a highly supersonic shock (Mach number $M >> 1$), the ratio between the gas densities on both sides of the shock front is

$$\frac{\rho_2}{\rho_1} = \frac{c_p/c_v + 1}{c_p/c_v - 1} \tag{1.2}$$

where, for a monoatomic or fully ionized gas, one can set the ratio of the specific heats $c_p/c_v = \frac{5}{3}$. By further imposing the mass conservation in the flow through the shock front $\rho_1 u_1 = \rho_2 u_2$, the ratio between the upstream and downstream velocity in the frame where the shock front is at rest becomes

$$\frac{u_1}{u_2} = 4 \tag{1.3}$$

meaning that the relative velocity between the two masses of gas, upstream and downstream, is $\frac{3}{4}u_1$.

A relativistic charged particle crossing the shock front with an incident angle θ_1 and an initial energy E_1, is subject to elastic collisions due to the magnetic field, so that its average motion soon coincides with that of the new system. The energy E_1' in the new reference frame is:

$$E_1' = \gamma E_1 \left(1 - \beta \cos\theta_1\right) \tag{1.4}$$

where γ and $\beta = \frac{3}{4}\frac{u_1}{c}$ are the Lorentz factor and velocity of the new reference frame. Considering a complete cycle forth and back across the shock front, one can calculate the energy in the final state in analogy with Eq. 1.4 and compute the energy gain:

$$\frac{\Delta E}{E_1} = \frac{1 - \beta\cos\theta_1 + \beta\cos\theta_2' - \beta^2\cos\theta_1\cos\theta_2'}{1-\beta^2} - 1. \tag{1.5}$$

If the flux of particles through the shock front is isotropic, the terms $\cos\theta_1$ and $\cos\theta_2'$ average, respectively, to $\langle\cos\theta_1\rangle = -\frac{2}{3}$ and $\langle\cos\theta_2'\rangle = \frac{2}{3}$, so that, supposing a non relativistic shock, the relative energy gain becomes:

$$\xi = \frac{\Delta E}{E_1} = \frac{4}{3}\beta\,. \tag{1.6}$$

After each cycle a particle has a probability P_{esc} to escape the acceleration region, given by the ratio between the flux of particles in the downstream moving away from the shock front, $\frac{1}{4}Nu_2$, and those crossing it, $\frac{1}{4}Nc$. Thus $P_{esc} = \frac{4}{3}\beta$. After n collisions there are $N = N_0(1-P_{esc})^n$ particles left with energies $E = E_0(1+\xi)^n$, giving rise to an integral spectrum:

$$\frac{N}{N_0} = \left(\frac{E}{E_0}\right)^{\frac{\ln(1-P_{esc})}{\ln(1+\xi)}}\,. \tag{1.7}$$

The exponent $\frac{\ln(1-P_{esc})}{\ln(1+\xi)}$ can be approximated to $-\frac{P_{esc}}{\xi} = -1$ in the case of a non-relativistic shock, which leads to the desired differential spectrum:

$$\frac{dN}{dE} \propto E^{-2}. \tag{1.8}$$

The observed spectrum of cosmic rays is steeper than the one predicted by the shock acceleration mechanism. This is due to the leakage of cosmic rays from the galaxy during their propagation. This leakage term depends on the energy, since more energetic particles are less confined by the galactic magnetic field, and accounts for a term $\propto E^{-\delta}$, with $\delta \approx -0.6$.

1.2 Astrophysical neutrinos

Neutrinos are not influenced by magnetic fields, are able to pass through dense environments and are a stable product of hadronic interactions. For these reasons they are an unambiguous probe to identify the production sites of high energy cosmic rays.

Astrophysical neutrinos are produced in the interaction of the accelerated cosmic rays with a target of photons or hadrons, which can take place within the acceleration region or outside of it. Hadronic interactions produce pions that further decay into neutrinos or gammas, according to the following decay chain:

$$\begin{array}{lllll} p/A + p/\gamma \longrightarrow & \pi^0 & + \ \pi^+ & + \ \pi^- & + \ X \\ & \downarrow & \downarrow & \downarrow & \\ & \gamma + \gamma & \mu^+ + \nu_\mu & \mu^- + \bar{\nu}_\mu & \\ & & \downarrow & \downarrow & \\ & & e^+ + \nu_e + \bar{\nu}_\mu & e^- + \bar{\nu}_e + \nu_\mu & \end{array} \tag{1.9}$$

where the neutrino is expected to acquire the 5% of the initial proton energy in these reactions.

If the acceleration region is optically thick, the γ's produced by the neutral pion decay would remain trapped and such a dark source would be visible only in neutrinos. Such a scenario is expected since the density of the target would favour the reactions in Eq. 1.9 to take place. In the case of an optically thin source, in a hadronic acceleration scenario, the fluxes of high energy photons and neutrinos would be closely related. However, high energy photons can be issued from entirely leptonic scenarios involving Inverse Compton scattering (IC) of high energy electrons on ambient low energy photons, in which case no neutrinos are expected.

As can be seen from the reaction chain in Eq. 1.9, the ratio between the neutrino[1] flavours produced at the source is $(\nu_e, \nu_\mu, \nu_\tau) = (1 : 2 : 0)$. These ratios become $(1 : 1 : 1)$ at Earth due to neutrino oscillation.

1.2.1 Candidate sources

Many of the proposed sources of high energy neutrinos include the environments where very energetic processes are supposed to take place in the universe. This section presents a non-exhaustive list of possible astrophysical sources of high energy neutrinos. Reviews can be found in (Gaisser et al., 1995; Bednarek et al., 2005; Becker, 2008).

Supernova remnants (SNR)

Remnants of past supernova explosions consist of a shell of hot gas expanding in the interstellar medium at a velocity $\sim 10^4$ km s^{-1}. These systems have long been proposed as the source of the galactic cosmic ray flux. Ginzburg and Syrovatsky (Ginzburg et al., 1964) observed that if around 10% of a SNR's mechanical energy ($\varepsilon_{SN} \approx 10^{51}$ erg) went to cosmic ray acceleration, the Milky Way losses due to cosmic ray propagation would be compensated by the observed rate of one supernova explosion every 30 years. SNRs could thus account for the cosmic ray flux up to the knee.

[1]Neutrino telescopes cannot distinguish between ν and $\bar{\nu}$.

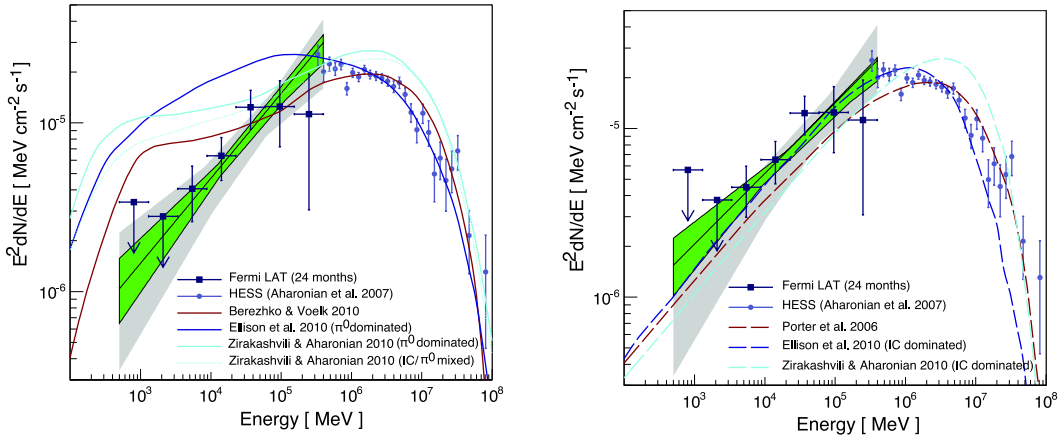

Figure 1.6: *Joint γ-ray spectrum of RX J1713−3946 as seen by H.E.S.S. and Fermi and compared with hadronic (left) and leptonic (right) models.*

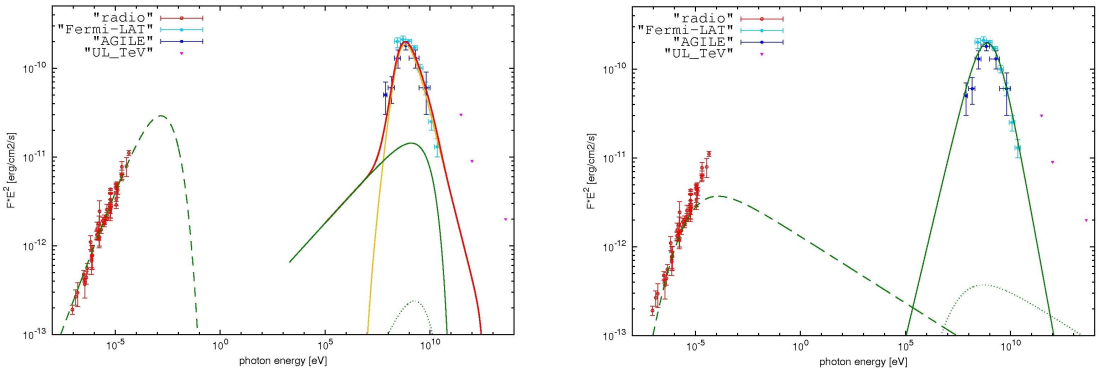

Figure 1.7: *Broad-band electromagnetic spectrum of the SNR W44 as fitted by the AGILE collaboration (Giuliani et al., 2011), considering a model in which the observed gamma rays are produced by neutral pion decay (left) and a leptonic model (right). The plots refer to the best fit obtained for each scenario.*

Some young SNRs have been observed emitting TeV photons (Albert et al., 2007a; Aharonian et al., 2006, e.g.), which confirms the presence of particle acceleration up to high energy in these environments. The observation by H.E.S.S. (Aharonian et al., 2006) of the SNR RX J1713−3946 seemed to favour the hadronic scenario, in which the observed TeV emission is produced by the interaction of relativistic protons with the interstellar gas, with the the production of π^0's. A more recent observation by the Large Area Telescope (LAT) onboard Fermi (Abdo et al., 2011) favours instead a leptonic scenario for the observed GeV emission, where photons are energized by collisions with relativistic electrons through Inverse Compton (IC) scattering.

The observations of the SNR W44 by the AGILE telescope seem to favour a hadronic origin of the detected gamma rays. A fit of the broad band spectrum is successfully modeled by the gamma-ray emission as being produced by accelerated hadrons with a spectral index ~ 3 and a cutoff energy ~ 6 GeV (Giuliani et al., 2011). The resulting fitted spectrum is shown in Figure 1.7.

Microquasars

Microquasars are X-ray binary systems formed by a compact object, i.e. a black hole or a neutron star, accreting mass from a companion star. The gravitational energy liberated by the in-falling matter is converted to accelerate collimated relativistic jets, that are observed as expanding radio knots for their non-thermal synchrotron emission. The hadronic component of the jets is still a matter of debate. A model that allows the estimation the flux of neutrinos produced in microquasar jets is presented in (Levinson et al., 2001). It assumes the energy employed in the acceleration process to be significantly dissipated through internal shocks, thus producing a non-thermal power law distribution of protons up to high energies. These protons can then interact with the X-rays from the accretion disk or with the synchrotron photons produced inside the jet by thermal electrons, thus producing neutrinos.

In high-mass microquasars, where the accretion is driven by the intense wind of the massive companion star, neutrinos and γ's could be produced by the interaction of the hadrons in the relativistic jets with the clumps of the stellar wind (Romero et al., 2003).

Active Galactic Nuclei

Active Galactic Nuclei (AGNs) are super-massive black holes of 10^4-$10^9 M_\odot$ accreting mass from their host galaxy. They are the most luminous persistent objects in the sky attaining luminosities of 10^{42}-10^{48} erg/s and are observed at all wavelengths from radio to TeV γ-rays. The accretion process onto the central black hole causes the ejection of relativistic radio jets. The high energy emission, including the TeV emission detected for many AGNs by Imaging Air Cherenkov Telescopes (IACTs), can be explained by both leptonic and hadronic models. Mannheim (1993) has shown that the addition of a component of protons to the jets of AGNs allows the production of high energy γ-rays and neutrinos.

Gamma Ray Bursts

Gamma Ray Bursts (GRBs) are intense flashes of light lasting from a fraction of second up to some minutes. These explosions can reach luminosities of $\sim 10^{51}$-10^{53} erg/s, corresponding to an emission of an entire solar mass in energy. Their origin was unknown until BeppoSAX observed one afterglow in 1997 and measured its redshift(Wijers et al., 1997), placing the source at a cosmological distance. The prompt emission from GRBs is made up by photons with energies around 100 keV, this is followed by an afterglow spanning all wavelengths. The model that best explains the observational features of GRBs is the *fireball* model (Piran, 1999). It describes the expansion of a hot plasma powered by a central engine in which the shells of the emitted gas can produce a shock front, accelerating electrons and baryons up to high energies. While the electrons would rapidly loose energy by the synchrotron process, the protons can interact with the fireball γ-rays and produce a burst of 10^{14} eV neutrinos (Waxman et al., 1997).

Chapter 2

Cherenkov neutrino telescopes and the ANTARES detector

ANTARES is the first neutrino telescope in the Mediterranean Sea and is currently taking data in its full configuration. In this chapter are presented the principles on which neutrino detection is based in a large scale telescope and the main features of ANTARES.

2.1 Detection principle

High energy neutrino telescopes consist of a sensitive volume instrumented with light sensors, to detect the Cherenkov light emitted by the relativistic charged particles (leptons or showers) produced by neutrino interactions (Figure 2.1). The distribution of light signals in space and time can be used to infer the neutrino direction. To reach a sufficiently high effective area of detection, considering the very small cross sections of charged and neutral current neutrino interactions, huge sensitive volumes must be employed, thus imposing the choice of natural environments, like seawater or the ice in Antarctica, as detector locations.

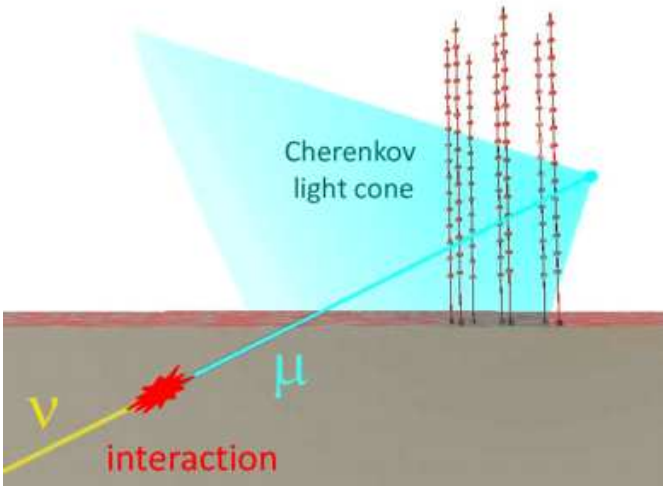

Figure 2.1: *An upgoing neutrino interacts in the proximity of the detector by charged current interaction producing a relativistic upgoing muon, which is detected via the Cherenkov radiation by a 3-dimensional array of photomultipliers.*

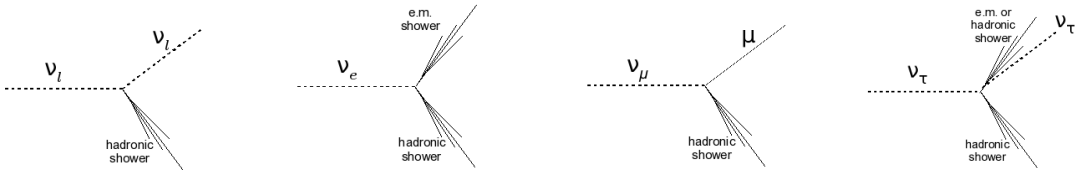

Figure 2.2: *Different topologies of neutrino interactions. At the energies of interest in neutrino astronomy the interaction with matter causes a hadronic shower. The leftmost diagram refers to neutral current interactions, the three on the right are charged current interactions with different flavours of neutrinos.*

2.1.1 Neutrino interaction

Being a neutral particle, the neutrino must interact sufficiently close to the detector volume and produce charged particles in order to be detected. Neutrinos interact only by the the weak force through exchange of $W^{\pm}$ or Z^0 bosons, which are mediators of the charged and neutral current interaction respectively, leading to the following reactions:

$$\begin{aligned} \nu_l + N &\longrightarrow l^{\pm} + X \text{ (CC)} \\ \nu_l + N &\longrightarrow \nu_l + X \text{ (NC)}. \end{aligned} \tag{2.1}$$

At the energies of interest in neutrino astronomy, i.e. $E_\nu \geq 100$ GeV, the neutrino interaction with matter causes a lepton and a hadronic shower, where the nature of the lepton depends on the flavour of the neutrino and type of interaction, as shown in Figure 2.2. At these energies, the interaction of neutrinos on hadrons is in the regime of the deep inelastic scattering, which can be interpreted in terms of elastic scattering on quarks and gluons. The differential cross section can be written in terms of the Bjorken scaling variables $x = Q^2/2M\nu$ and $y = \nu/E_\nu$ as:

$$\frac{\mathrm{d}^2\sigma^\nu}{\mathrm{d}x\,\mathrm{d}y} = \frac{2G_F^2 m_N E_\nu}{\pi}\left(\frac{M_W^2}{Q^2+M_W^2}\right)\left[xq(Q^2,x) + x\bar{q}(Q^2,x)(1-y)\right] \tag{2.2}$$

where $-Q^2$ is the invariant momentum transfer between the incident neutrino and outgoing muon, $\nu = E_\nu - E_\mu$ is the energy loss in the lab (target) frame, M and M_W are the nucleon and intermediate-boson masses and $G_F = 1.16632 \times 10^{-5} GeV^{-2}$ is the Fermi constant. The terms $q(Q^2, x)$ and $\bar{q}(Q^2, x)$ represent the parton distribution functions of quarks and antiquarks. For the theoretical calculation of the inclusive neutrino cross section at high energies, the parton distributions are obtained from data at low Q^2 and then are evolved to higher scales using the Altarelli-Parisi equations. An example cross section calculated using the HERAPDF1.5 parton distributions (Cooper-Sarkar, 2010) is show in Figure 2.3.

As the cross section increases, the earth becomes more and more opaque at higher energies. The interaction length expressed in water-equivalent-centimeters is $L_{int} = [N_A \cdot \sigma_{\nu N}(E_\nu)/cm^{-2}]^{-1}$, which becomes comparable to the Earth diameter at ~ 60 TeV[1]. Figure 2.4 shows the probability for high energy neutrinos to cross the Earth as a function of the incident angle.

[1]Supposing a uniformly dense Earth.

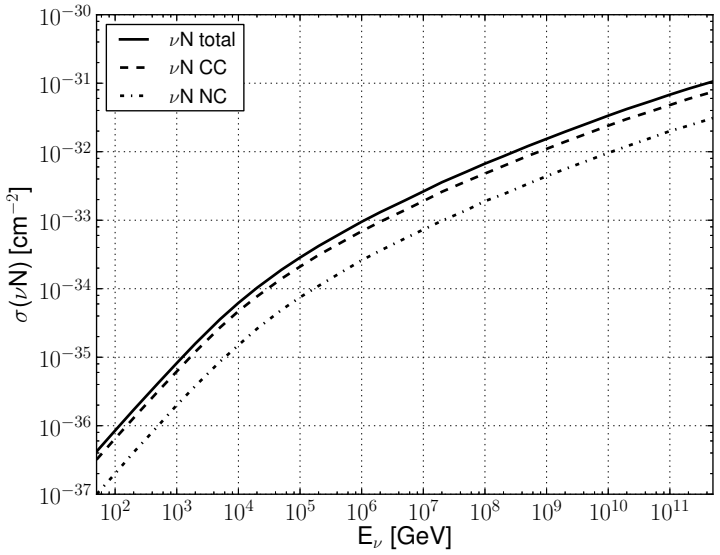

Figure 2.3: *Neutrino-nucleon inclusive cross section calculated using the HERAPDF1.5 parton distributions (Cooper-Sarkar, 2010). Data taken from (Cooper-Sarkar et al., 2011).*

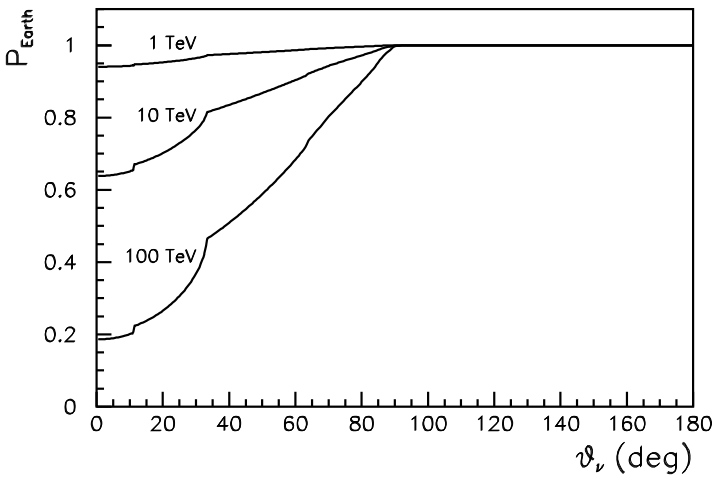

Figure 2.4: *Probability for a neutrino to cross the Earth as a function of the incident angle, for three different energies. Here $\theta_\nu = 0$ corresponds to the upgoing direction.*

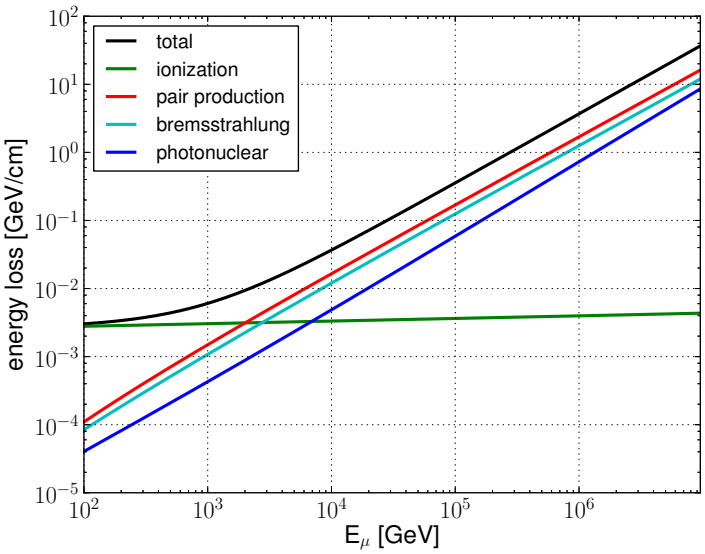

Figure 2.5: *Contributions to the specific energy loss of a muon propagating in water, obtained using the parametrization in (Klimushin et al., 2001).*

2.1.2 Muon propagation in water

The energy loss of a muon propagating in water is, in the first instance, due to ionization, which can be described as a continuous process. At a certain energy, called the critical energy, more disruptive phenomena start dominating the energy losses. These *radiative processes* that can initiate hadronic and electromagnetic showers are: electron pair production, bremsstrahlung and photonuclear interaction. The mean specific energy loss of high energy muons in water can be described by:

$$\langle -\frac{\mathrm{d}E}{\mathrm{d}x} \rangle = a(E) + b(E)E, \tag{2.3}$$

where E is the total energy, $a(E)$ is the contribution due to ionization and $b(E)$ is due to radiative processes (cf. Figure 2.5). Both $a(E)$ and $b(E)$ are slowly varying functions of E at high energies. The energy at which radiative losses equal ionization losses is referred to as the muon critical energy, $E_{\mu c} = a/b$, and occurs at 1 TeV in water.

The range, i.e. the total distance travelled by the muon, can be estimated in the "continuous slowing down" approximation as:

$$R(E) \approx (1/b)\ln(1 + E/E_{\mu c}), \tag{2.4}$$

where $b \sim 10^{-6}$ cm^{-1} (Klimushin et al., 2001), giving $R(E_{\mu c}) \approx 10$ km. The ability to propagate for such long distances in water makes the muon neutrino the preferred flavour for astronomy, since it allows in principle to achieve a good precision in track reconstruction.

2.1.3 Cherenkov radiation

A charged particle travelling in a material induces the creation of charge dipoles which depolarize immediately after its passage. The radiation resulting from the depolarization process can sum up by constructive interference if the particle travels at a speed higher than the speed of light in the material, giving rise to the Cherenkov radiation.

Cherenkov photons are emitted at a specific angle from the track and the wavefront forms a cone having the particle's track direction as symmetry axis. The Cherenkov angle can be obtained using the Huygens construction and is given by

$$\theta_C = \arccos\left(\frac{1}{\beta n}\right), \tag{2.5}$$

where $\beta = v/c$ is the speed of the particle and n is the refractive index of the material. In water $\theta_C \approx 42.5°$.

The energy loss due to the Cherenkov emission is negligible, but the emitted photons can be used in neutrino telescopes to detect the muons and reconstruct their trajectory. The number of photons emitted per track length and per wavelength interval is

$$\frac{\mathrm{d}^2 N}{\mathrm{d}x\,\mathrm{d}\lambda} = \frac{2\pi\alpha z^2}{\lambda^2}\left(1 - \frac{1}{\beta^2 n^2}\right) \tag{2.6}$$

where α is the fine structure constant, z is the charge of the particle causing the emission and λ is the wavelength of the emitted photons. Integrating Eq. 2.6 between 300 nm and 600 nm, for which Cherenkov light contributes most to the signal from a muon, yields an quantity of ~ 350 photons emitted per centimeter of track.

2.1.4 Light propagation in water

Cherenkov photons propagating in water are subject to absorption and scattering. These effects reduce the number of detected photons and smear their arrival direction at the light sensors. Both processes can be described by means of the characteristic lengths, λ_{abs} and λ_{sct} respectively, for which the probability for a photon to propagate undisturbed along a certain distance d is proportional to $e^{-d/\lambda}$. In the case of scattering, an effective length can be defined that takes into account the possibility to actually detect a photon even if one or more scatterings have taken place. This is the "effective" scattering length and is defined as

$$\lambda_{sct}^{eff} \equiv \frac{\lambda_{sct}}{1 - \langle\cos\theta\rangle} \tag{2.7}$$

where $\langle\cos\theta\rangle$ is the average cosine of the scattering angle. Eq. 2.7 holds only if $\langle\cos\theta\rangle \approx 1$, which is the case for multiple scattering in seawater. The total effect on efficiency due to both absorption and scattering can be accounted by a single parameter called the attenuation length, defined as

$$\frac{1}{\lambda_{att}} = \frac{1}{\lambda_{abs}} + \frac{1}{\lambda_{sct}^{eff}}\ . \tag{2.8}$$

Measurements of the quantities λ_{abs}, λ_{sct}^{eff} and λ_{att}^{eff} at the ANTARES site can be found in (ANTARES Collaboration, Aguilar, et al., 2005).

The velocity at which light propagates in water is a key parameter for the track reconstruction algorithms employed in data analysis. The refraction index used to calculate the Cherenkov angle in Eq. 2.5 refers to the phase velocity of light, and is here indicated as n_p

$$v_p = \frac{\omega}{k} = \frac{c}{n_p} \tag{2.9}$$

where v_p is the phase velocity, ω the frequency of the travelling wave packet and k the wave number. v_p indicates at which speed the phase propagates within the wave packet. The velocity of the light signal is given instead by the group velocity, defined as

$$v_g = \frac{\mathrm{d}\omega}{\mathrm{d}k} = \frac{c}{n_p} - \frac{ck}{n_p^2}\frac{\mathrm{d}n_p}{\mathrm{d}\omega} \ . \tag{2.10}$$

Measurements of the group refractive index as a function of the wavelength at the ANTARES site are presented in (Adrián-Martínez et al., 2011b).

2.1.5 Sources of background

An underwater/ice Cherenkov detector has to deal with several sources of noise coming either from the environment in which it is placed or from other particles mimicking the signal. In this section the most important are explained.

^{40}K decay A small concentration of potassium is naturally contained in sea water, a part of which is in the radioactive isotopic form of ^{40}K. This isotope has two main decay channels

$$^{40}K \rightarrow \ ^{40}Ca + e^- + \bar{\nu}_e \qquad B.R. = 89.3\% \tag{2.11}$$

$$^{40}K + e^- \rightarrow \ ^{40}Ar + \nu_e + \gamma \qquad B.R. = 10.7\% \tag{2.12}$$

The energy released in the first process is 1.31 MeV, thus the electrons emitted are able to produce Cherenkov light. The γ produced after the electron capture, second process, has an energy of 1.46 MeV and can then Compton scatter producing a fast electron above the Cherenkov threshold. The overall effect produces a constant count rate of low amplitude (mostly 1 p.e.) and time uncorrelated light signals at the PMTs. This process contributes to the counting rate of a PMT with about 100 Hz per cm^2 of photocathode area.

Bioluminescence Despite the harsh conditions for life, sea abysses can host a variety of organisms, some of which are able to produce light by means of chemical reactions. The resulting optical background at the PMTs is characterized by a rather stable component called *baseline*, supposedly produced by monocellular organisms, and by a burst component, probably due to multicellular organisms and characterized by light flashes. In ANTARES, the baseline count rates range between 60 kHz and few hundreds kHz, whereas during bursts the count rate can jump up to $\sim$ 1 MHz.

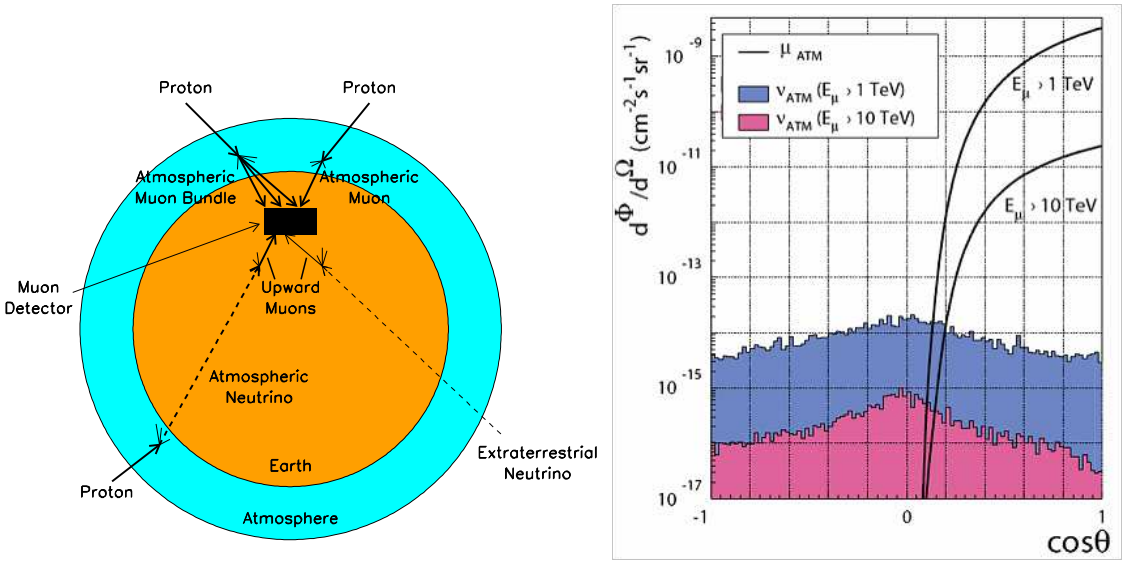

Figure 2.6: *(Left) Particle backgrounds at the detector. Cosmic rays interacting in the atmosphere create a flux of downgoing atmospheric muons and upgoing atmospheric neutrinos. (Right) Comparison between the flux of atmospheric muons and neutrinos at the detector. In the downgoing direction* ($\cos\theta > 0$) *the muon flux is* $\sim 10^6$ *times higher than the neutrino flux.*

Atmospheric muons and neutrinos Primary cosmic rays interacting in the atmosphere can initiate air showers and produce muons and neutrinos, that constitute the particle background at the detector (Figure 2.6).

The relativistic muons produced in the atmosphere, if sufficiently energetic, can travel downward and reach the detector despite the thick layer (2-3 km) of water/ice in between. The resulting muon flux at the detector is significantly higher than the expected flux of cosmic neutrinos, and even $\sim 10^6$ times higher than the atmospheric neutrino flux. This blinds the downward direction, while the shield provided by the Earth still allows to look for upgoing tracks. A single shower can produce more muons in a single bundle reaching the detector. Downgoing muon bundles can mimic the space time distribution of light signals from upgoing tracks and constitute a major background to be rejected. This rejection is accounted for by the track reconstruction algorithms.

Atmospheric neutrinos emitted from the interactions of primary cosmic rays with the atmosphere constitute an irreducible background for the detection of cosmic neutrinos, though the energy spectrum is supposed to be steeper than that expected from a cosmic source. Moreover a drastic background reduction can be performed on a directional basis when looking for point sources. At low energies the flux of atmospheric neutrinos originates mainly from pion and kaon decay. At higher energies, other shorter lived hadrons are produced, which contribute to the flux by the decay of charmed mesons. This "prompt" component dominates the atmospheric neutrino flux from energies above ~100 TeV.

2.2 Neutrino telescopes

The first studies for the construction of a neutrino telescope were carried out by the DUMAND[2] collaboration, whose project started in 1976. Its goal was to build a deep ocean high energy neutrino detector at 4800 m depth off shore the Big Island of Hawaii. After the deployment of a test optical string and a junction box cabled to shore, the project was dismissed due to technical problems, but its pioneering work was of great importance for the telescopes to come. In this section are described two of the currently working detectors: Baikal and IceCube. The entire next section is dedicated to ANTARES.

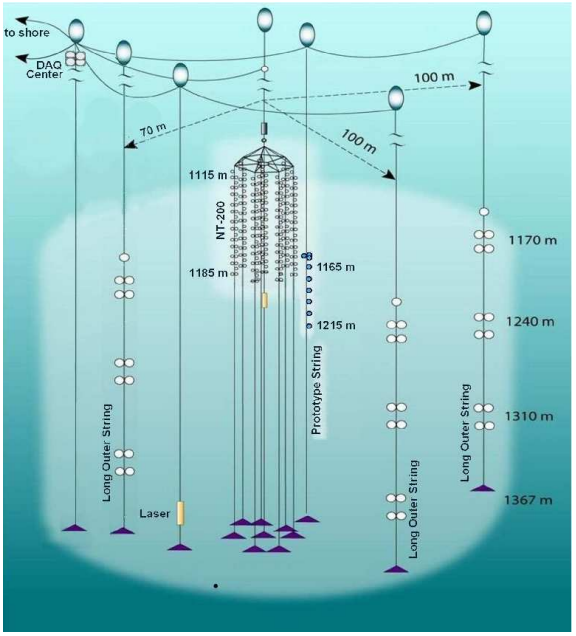

Figure 2.7: *The Baikal Telescope NT200+ as of 2008, made of the NT200 (centre) plus 3 long outer strings and the new technology km3-prototype string.*

2.2.1 Baikal

The Baikal telescope (Aynutdinov et al., 2009, and references therein), situated in the lake Baikal in Siberia at 1.1 km depth, is the first neutrino telescope operating underwater and started taking data in 1993 in its configuration named NT36 with 36 optical sensors. It was upgraded in 1998 to NT200 with 192 optical modules displaced on 8 strings, each carrying 24 pairwise arranged optical modules (central part in Figure 2.7). In 2005 3 new strings have been placed at 100 m from the NT200 core, which has increased the sensitivity to very high energy neutrinos by a factor 4. The collaboration is currently carrying on an R&D activity aimed to the construction of a km^3-detector in the lake Baikal by the extension of the actual detector.

[2]Deep Underwater Muon and Neutrino Detection

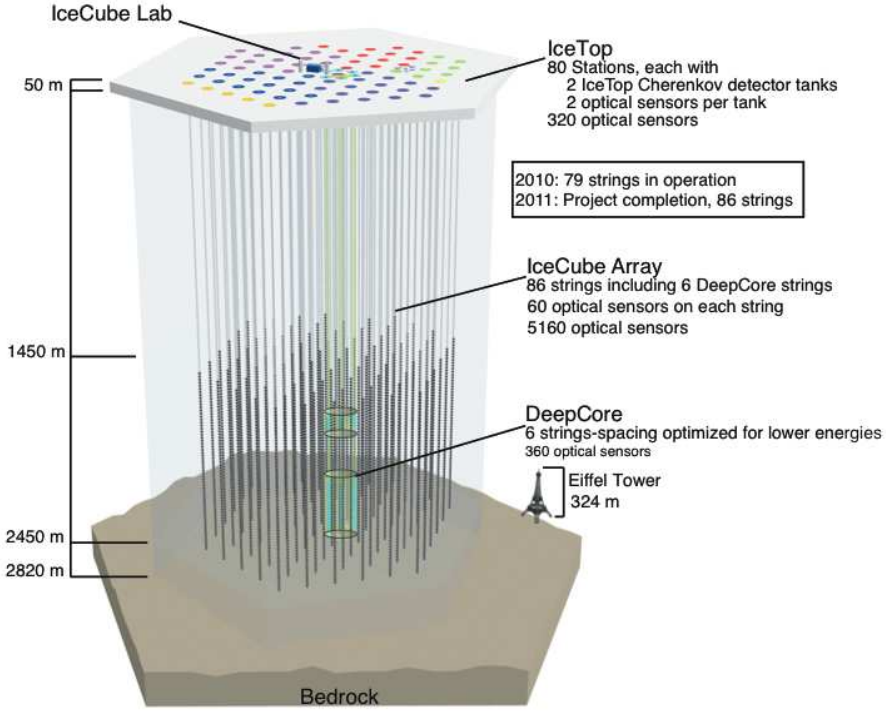

Figure 2.8: *The IceCube observatory.*

2.2.2 IceCube

The IceCube detector (Klein, 2009) is currently the largest neutrino telescope with its 79 strings holding 4800 digital optical modules in a sensitive volume of about 1 km^3 (Figure 2.8). It is placed at the geographic South Pole, between 1.45 and 2.45 km below the glacial surface, and was built following the experience of AMANDA, the smaller scale predecessor that pioneered neutrino detection in the ice. Some of the advantages of ice over water are the absence of ^{40}K and bioluminescence optical backgrounds, together with the temperature of 30-50 degrees below zero which significantly reduces the PMT dark noise. This feature allows the use of a single PMT per floor along the string, since no local coincidences are needed to discriminate the optical background.

The detector has recently been upgraded with the addition of 7 more strings that provide a higher density of PMTs at the centre of the detector. This extension is called DeepCore and its goal is to reduce the detection threshold of neutrinos down to 10 GeV. The rejection of the intense atmospheric muon background is done using the surrounding IceCube as a veto detector, thus allowing the detection of downgoing neutrinos, whose signature is the presence of a track in the DeepCore that left no trace in the rest of the detector. The low energy threshold of detection makes it well suited for dark matter searches.

The IceCube observatory is also equipped with a surface Cherenkov array, IceTop, used to provide the absolute pointing to the neutrino detector, as well as to detect cosmic rays.

2.3 The ANTARES detector

The ANTARES[3] neutrino telescope (ANTARES Collaboration, Ageron, et al., 2011) is located in the Mediterranean Sea, 40 km South-East offshore from Toulon[4], on a plateau at 2475 m depth (Figure 2.9). The general detector layout is shown in Figure 2.10. The detector is composed of 12 detection lines anchored to the seabed and kept up by a buoy at the top, each hosting 75 Optical Modules (OMs). The OMs (Figure 2.11) constitute the sensitive part of the detector and are composed by a pressure resistant glass sphere housing a 10" photomultiplier tube (PMT) with its base. On the lines the OMs are placed in groups of three in a storey, referred to as "floors", distributed with a uniform spacing of 14.5 m along the line, for a total of 25 floors per line. The three OMs of each floor are spaced by 120° around the detector-line axis. The line of sight of each OM is inclined towards the sea bottom by 45° to optimize for the detection of upgoing muons. Each floor is the assembly of a mechanical structure, called the optical module frame, which supports the OMs, and a titanium container, the Local Control Module (LCM), housing the offshore electronics and embedded processors. Five consecutive floors are grouped in a sector, which acts as an independent unit for what concerns Data AcQuisition (DAQ) and power distribution. Each sector is controlled by a special LCM called Master LCM (MLCM).

The Main Electro Optical Cable (MEOC), of 45 km length, connects the shore station at La Seyne-sur-Mer to a Junction Box (JB) placed on the seabed near the detector. The role of the JB is to split the power supply and the optical signals to 16 sockets which allow further connection to the detector-lines by means of electro-optical interlink cables, thus ensuring the complete control of the data flow to and from the detector lines.

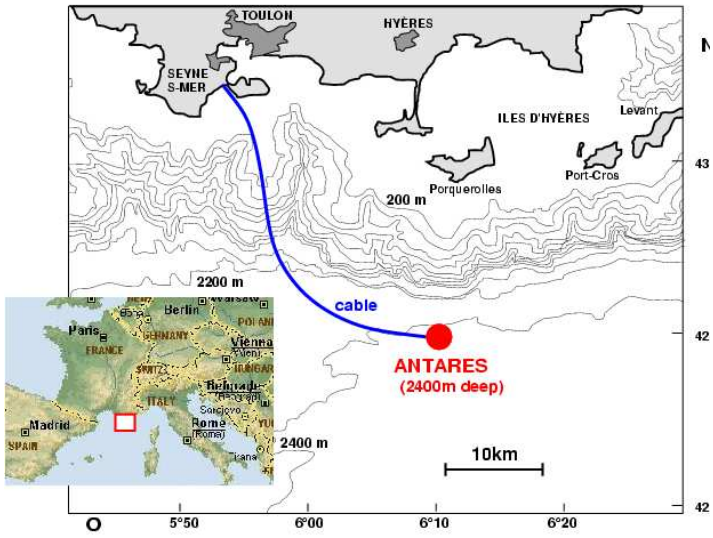

Figure 2.9: *Bathymetric map of the ANTARES site.*

[3]Astronomy with a Neutrino Telescope and Abyss environmental RESearch.
[4]42°48N, 6°10E

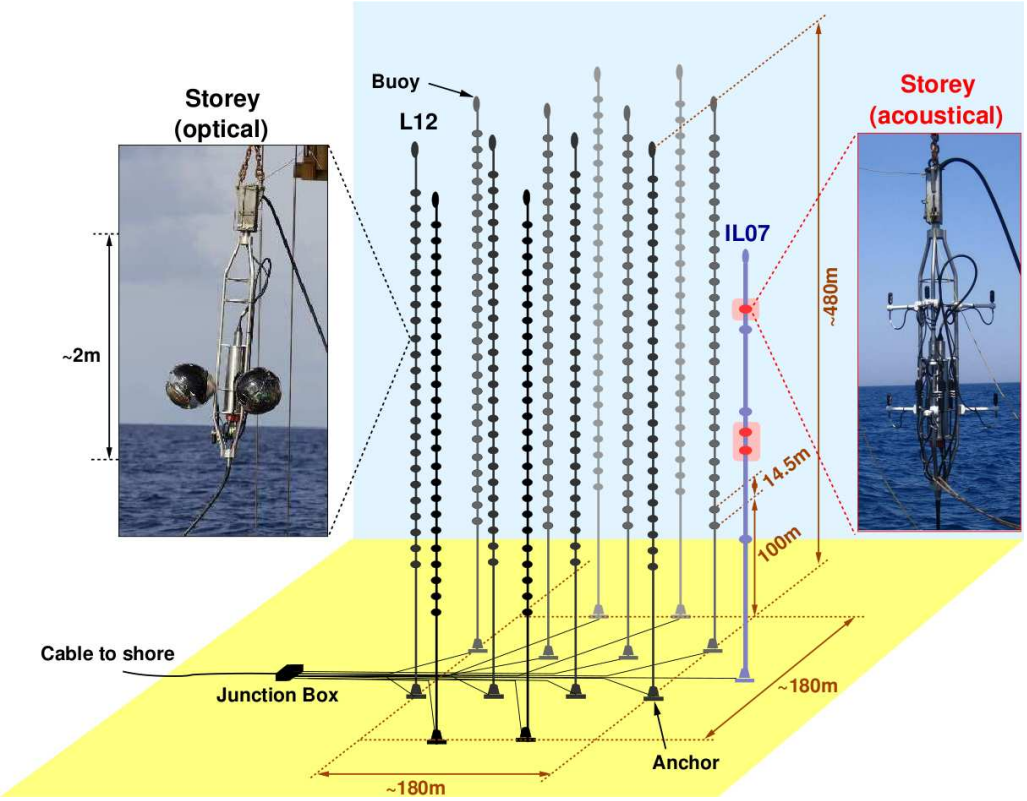

Figure 2.10: *Layout of the ANTARES detector. In black the optical detector lines. In blue the instrumentation line.*

2.3.1 Data acquisition system

A scheme of the data acquisition system in ANTARES is shown in Figure 2.12. The front-end electronics of each storey is contained in the LCM. The analog signals coming from the PMTs are treated by a dedicated chip, the Analogue Ring Sampler (ARS), which digitizes both charge and time. To obtain the charge an Amplitude to Voltage Converter (AVC) integrates the analog output of the PMT every ∼8 ns until a certain threshold is reached, normally set to 0.3 photo electrons (p.e.), after which an integration window extends by a time adjustable between 25 and 80 ns. The integrated charge is then digitized by an Analog to Digital Converter (ADC). The time of the detected signal is obtained with respect to a time stamp of a 20 MHz clock coming from shore (§ 2.3.2) by means of a Time to Voltage Converter (TVC) that provides the time with a subnanosecond precision. To reduce the dead time, the signals from a single PMT are digitized by two ARSs working in flip-flop mode.

The data flow from the instrumentation of each storey, including that of the ARSs, is conveyed to the DAQ Slow Control card, also contained in the LCM, which is equipped with an FPGA, with a buffer memory to avoid network congestion, and a 100 Mb/s Ethernet switch, that sends the data to the MLCM of the corresponding sector. The data are then sent through an Ethernet switch in the MLCM to a Dense Wavelength Division Multiplexing (DWDM) unit placed at the bottom of each line in the String Control Module (SCM) and forwarded to the JB through the interlink cable and to the shore station through the MEOC.

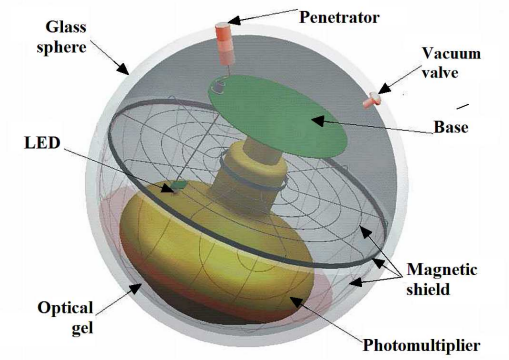

Figure 2.11: *Schematic view of an optical module.*

The flow of data onshore is handled by a computer farm which demultiplexes the data and filters the events. Several different trigger algorithms are applied for the event selection, including a general purpose muon trigger, a directional trigger, muon triggers based on local coincidences, a minimum bias trigger for monitoring the data quality and dedicated triggers for multi-messenger investigations. The general purpose trigger, which is the one used in this thesis, makes use of the causality relation between two hits

$$|t_i - t_j| < r_{ij}\frac{c}{n} \tag{2.13}$$

where $t_{i(j)}$ is the time of the hit i (j), r_{ij} is the distance between the PMTs i and j, c is the speed of light and n is the refractive index of water. The causality relation is applied only to so called L1 signals, i.e. either the coincidence within 20 ns of two hits in two neighbouring PMTs or the occurrence of large pulses higher than 3 photoelectrons. For an event to be stored a second level trigger condition has to be satisfied. The events labelled by two specific trigger logics have been used in this thesis, these are:

3N trigger : requires the presence of at least 5 casually related L1 hits in the detector,

2T3 trigger : requires at least two T3 coincidences in the detector within 2μs. A T3 coincidence is defined as a coincidence within 100 ns between two adjacent storeys, or within 200 ns between next-to-adjacent storeys of the same line.

Other trigger logics are also implemented but not always used. These comprise a Galactic Centre directional trigger and other looser triggers that can be used only during favourable conditions of the optical bioluminescence background.

2.3.2 Clock system and timing calibration

The clock system provides a common time reference to the readout of the OMs from a 20 MHz clock generator on shore, interfaced with a GPS timing system that provides the absolute time stamp. This allows a precision of 100 ns to be obtained with respect to the Universal Time Coordinates, which is enough to convert the direction of the neutrino to celestial coordinates and to correlate it to astrophysical

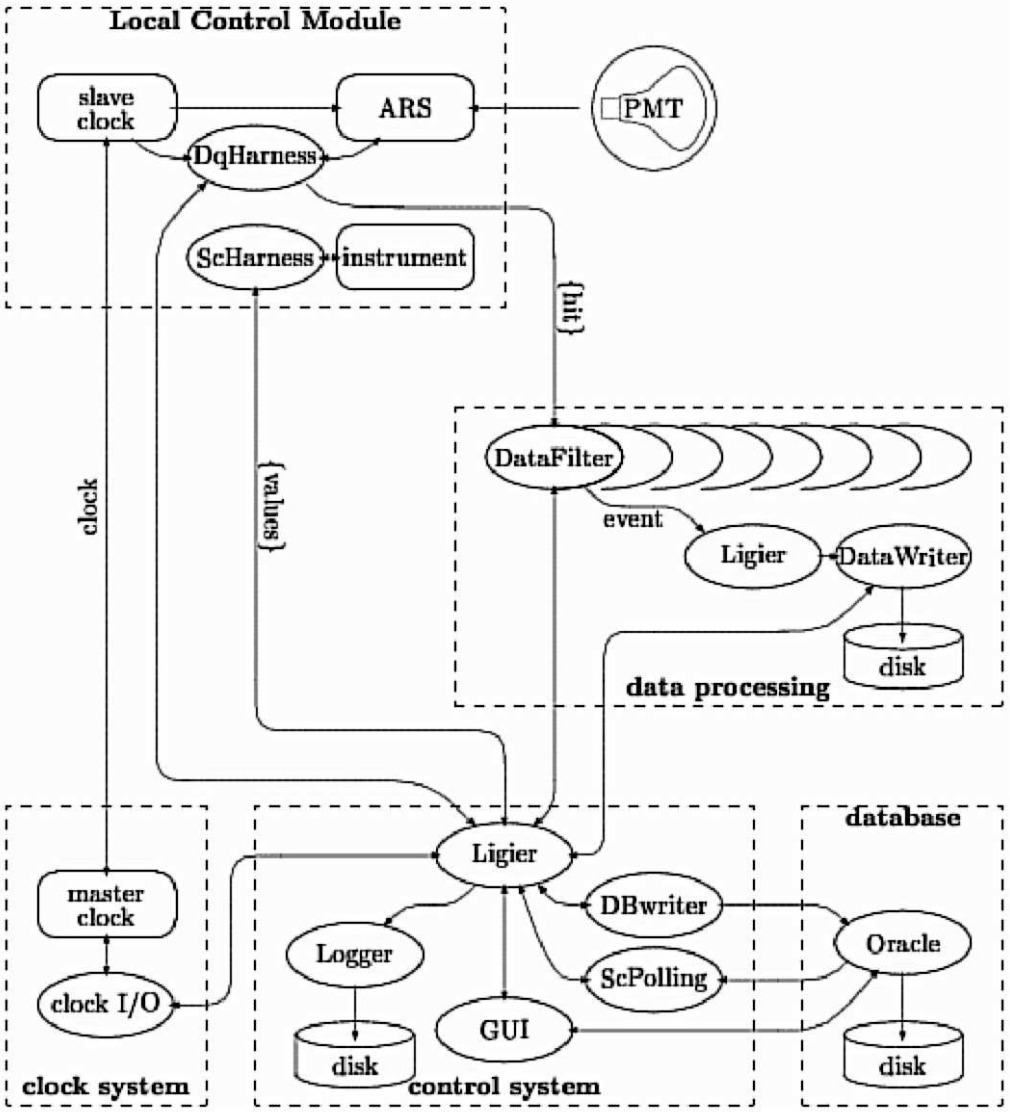

Figure 2.12: *Scheme of the data acquisition system in ANTARES.*

phenomena of few ms. The clock signal is distributed via optical fibres up to the SCMs at the base of each line, where it is converted to an electrical signal and distributed to each sector. Within a sector it is daisy-chained between the LCMs. The LCMs are also equipped with a transceiver able to send back the signal, thus allowing the stability of the round trip from/to shore to be monitored.

Muon track reconstruction requires a precision of ∼1 ns on the relative times of the hits in the whole detector. This is obtained through a time calibration procedure whose goal is to account for all the contributions to the transit time of signals from the OMs to shore. The round trip shore-LCMs of the clock signals, which is monitored once per hour, is twice the propagation time. A further time offset for each OM is due to the PMT transit time, the OM-LCM cabling, the front-end electronics response time and the ARS threshold. These are measured by means of LED beacons placed on the storeys 2, 9, 15 and 21[5] of each line, as well as LASER beacons placed at the bottom of two central lines. The LED beacons are able to flash the PMTs of the same line and are used to calibrate the time offsets between corresponding OMs (intra-line offsets). The start time of the flash is obtained from an 8 mm PMT placed within the LED beacon, while the expected arrival time of the signal at the OM is given knowing the distance. LASER beacons are able to illuminate the whole detector and are thus used to measure the offsets between different lines (inter-line offsets). This calibration procedure is also called *in situ* calibration. Before the deployment of a line, a time calibration is always performed in a dark room and allows the analysis of the the data taken immediately after the deployment.

2.3.3 Positioning system

Due to the sea currents, the whole line structure is subject to displacements from the vertical relative to the fixed base on the seabed. The OMs can move up to several meters from their nominal position depending on the sea conditions, as one can see in Figure 2.13. To allow for track reconstruction without degrading the angular resolution, a precision on the OMs' positions of 20 cm is required, corresponding to a 1 ns requirement in time precision. This is obtained from the positioning system, which comprises an acoustic system and series of tiltmeters and compasses placed on each storey. Acoustic emitters at the bottom of each line broadcast sinusoidal wave packets of short duration (typically 2 ms) and high frequency (40-60 kHz), detected by hydrophones distributed along each line on storeys 1, 8, 14, 19 and 25. The hydrophones are not uniformly distributed along the line, being more concentrated near the top, where the displacement is at its greatest and a better precision is required. Knowing the travel time of the emitted sound wave and the sound speed profile in water, which is obtained by means of sound velocimeters placed at different locations along the detector lines, the exact position of each hydrophone can be obtained by triangulation. These positions are used to reconstruct the line shape on the basis of a mechanical model that takes into account the influence of the drag forces due to the currents, the buoyancy and the weight of each element. The inclination angle $\Theta(z)$ of a point of the line with respect to the vertical can be

[5]Storeys in ANTARES are numbered from bottom to top.

computed from the vertical forces (buoyancy minus weight) F_z and the horizontal drag forces $F_\perp = \rho C_W A v^2$, where ρ is the water density, A is the cross section area of the element considered, v is the sea current velocity and C_W is the drag coefficient. Since $\tan\Theta = dr/dz$, by integrating the resulting expression along the line one obtains the so called "line shape formula", that relates the displacement r to the position along the line z:

$$r(z) = av^2 z - bv^2 \ln[1 - cz] \tag{2.14}$$

where a,b and c are known coefficients, while the sea current velocity v is left as a free parameter of a χ^2 fit. Once the line shape is calculated, the tiltmeters and compasses contained in the LCMs allow the inclination and the orientation of each storey to be obtained, from which the exact position of each OM is obtained.

The error on the position is computed by comparing the calculated distance between the acoustic emitters and receivers before and after triangulation. It is estimated to be ∼10 cm, well below the requirements.

The positioning of the detector is performed every 2 minutes, which is short enough in relation to the slow movements of the lines under the action of the sea currents.

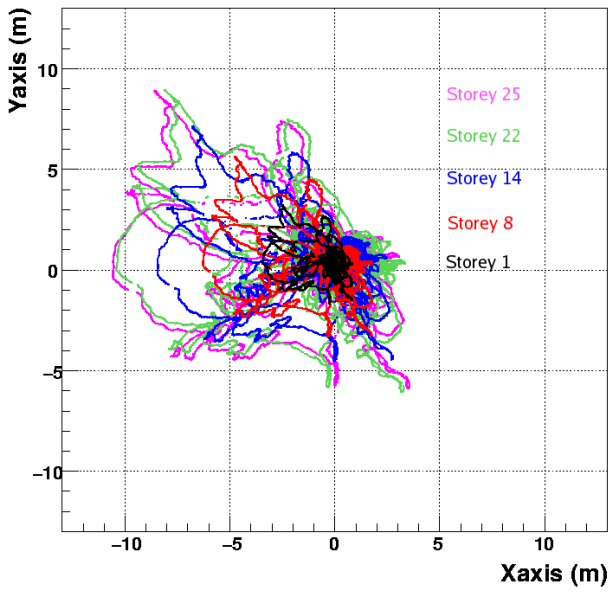

Figure 2.13: *The horizontal movements from anchor, of all hydrophones on Line 11 for a 6 month period. The dominant East-West heading of the line movements is due to the dominant Ligurian current which flows at the ANTARES site.*

2.3.4 Charge calibration

Special calibration runs are regularly performed to calibrate the amplitude of the detected light signals. During such runs the output of the PMT is digitized at random times, allowing the measurement the pedestal of the AVC channel. The

single photo-electron peak is obtained from minimum bias events, since the optical activity due to the ^{40}K decay and bioluminescent bacteria produces primarily single photons at the photocathode level. The knowledge of the position of the single photoelectron peak and of the pedestal is used to determine the charge conversion over the full dynamical range of the ADC.

2.3.5 Detector status and operation

The first phases of the detector construction started in the second half of the 1990s with the sea campaigns in which several sites were evaluated and their properties studied. In 2001 the main electro optical cable was laid down from the shore station to the detector site, and one year later the junction box was deployed. Hence the technology developed for the final detector was validated with the deployment and the connection of a prototype sector line, with only one sector, and a mini instrumentation line, in 2003. In 2005 a mechanical test line, i.e. a fully equipped detector line without electronics connection, was deployed to validate the final design, together with a fully equipped instrumentation line. After the successes of these tests, the first two ANTARES lines were deployed and connected in 2006. ANTARES physics data taking started at the end of January 2007 when lines 3,4 and 5 were connected. In December 2007 lines 6-10 were deployed and in May 2008 the detector was finally completed with the connection of lines 11 and 12. Soon after the detector was completed, on 24 June 2008, a fault in the offshore part of the main electro-optical cable caused the interruption of the data taking until the cable was repaired in September 2008. Since then, some other maintenance operations were performed to repair detector lines 6, 9, 10 and 12, which failed in 2009. Between 2009 and 2010 all the lines were repaired and reconnected. At present, the detector is taking data in its full configuration with 12 lines. This analysis uses the data taken from January 2007 to December 2010, comprising all the different detector configurations.

The recent data taking activity from the last three years is summarized in Figure 2.14, which shows bioluminescence activity, sea currents, muon rate and triggering. It can be seen how the currents correlate to the mean optical rates, and how this influences the data taking. Low sea currents are normally associated to low bioluminescence activity which allows looser trigger to be employed and thus increase the rate of detected downgoing muons. This also reflects on the number of effective days of data taking per month, shown in Figure 2.15. It is possible to see how during the periods with high bioluminescence rate, that normally happen during spring, the effective *livetime* per month decreases. An average of 3 upgoing neutrinos are detected and reconstructed using more than one line per active time of data taking. The latter being as high as 90% of the apparent time during favourable data taking conditions.

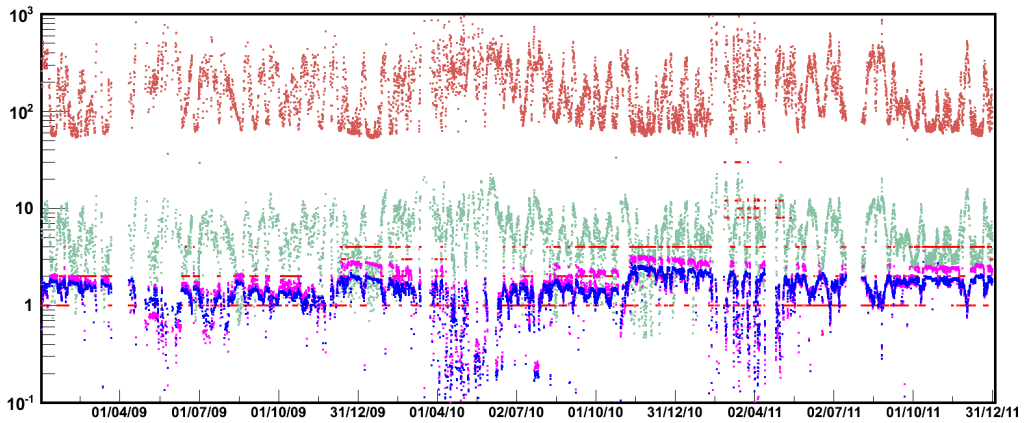

Figure 2.14: *Last three years' evolution of: mean optical rates in brown (kHz), sea current speed in green (cm/s), rate of muons reconstructed with only one line in magenta and with more lines in blue (Hz). In red is represented the trigger code: 1=simple causality trigger (3N+2T3), 2=1+Galactic Centre trigger, 4=2+low energy triggers. The step in November 2010 corresponds to the reconnection of lines 6 and 9.*

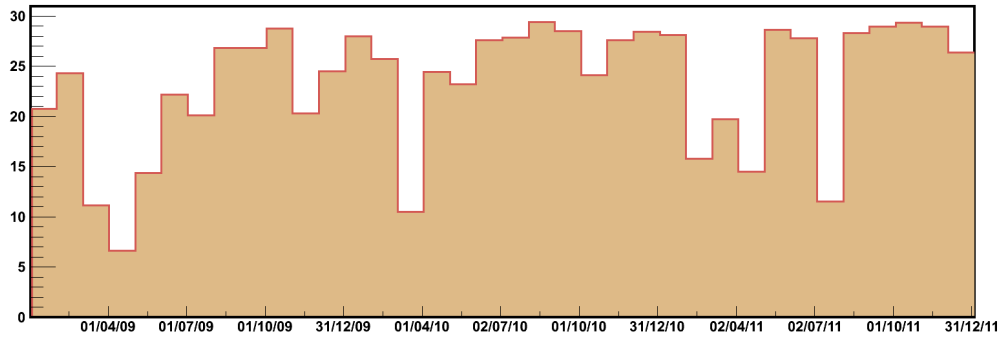

Figure 2.15: *Days of effective data taking per month between 2009 and 2011. The hole in July 2011 is due to a problem occurred to the database from which the detector configuration is read at the beginning of a new data run. The effect of this is also visible in Figure 2.14.*

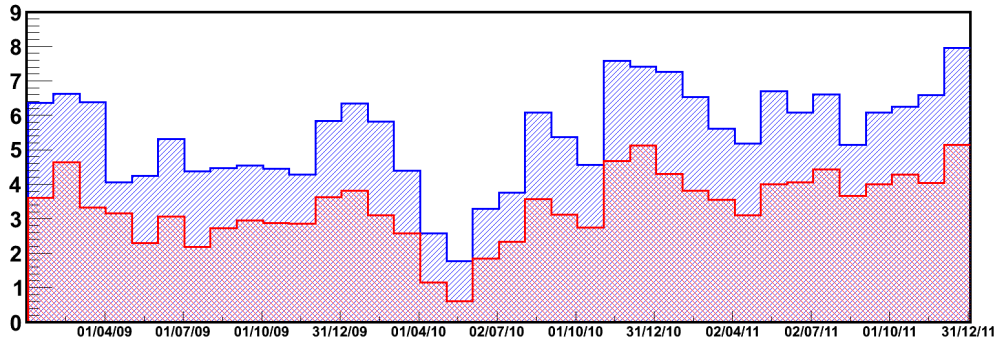

Figure 2.16: *Number of detected upgoing neutrinos per active day of data taking between 2009 and 2011, averaged in bins of one month. In red those reconstructed with multiple lines, in blue the single lines.*

2.3.6 Selected physics results of ANTARES

To test for the presence of astrophysical neutrino sources with ANTARES data, analyses have been conducted to search for both point sources and diffuse fluxes. This section briefly presents the results of published analyses.

A search for point sources of neutrinos has been performed by either looking at the fixed positions of a list of already known objects, or by scanning the whole sky to look for a cluster of neutrino events coming from the a certain, a priori unknown, direction. The first kind of search is referred to as "candidate search" and has the advantage to focus the observation to a relatively small portion of the sky, thus reducing the contamination of the background and requiring fewer signal neutrinos to set a discovery or an evidence. The second type of search is called a "full sky search" and is performed not to leave any part of the sky untested. Both kinds of analyses have been applied to the data collected between 2007 and 2008, corresponding to a data taking livetime of 304 days, during which 2190 neutrino candidates have been selected (Adrián-Martínez et al., 2011a). The sky map of the candidate neutrino events is shown in Figure 2.17a, together with the positions of the candidate sources represented as red circles. Since no significant excess has been found from these searches, limits on the neutrino flux have been set and are shown in Figure 2.17b. These are the most constraining limits on the part of the sky which is always visible by ANTARES, with a sensitivity of $7.5 \times 10^{-8}(E_\nu/\mathrm{GeV})^{-2}\mathrm{GeV}^{-1}\mathrm{s}^{-1}\mathrm{cm}^{-2}$.

In a separate analysis, a set of candidate AGN blazars, which exhibit relativistic jets pointing almost directly towards the Earth, has been selected among those detected by the Fermi/LAT gamma ray telescope and probed for neutrino emission during gamma ray flares (Adrián-Martínez et al., 2011c). Among the 10 sources under study, the most significant neutrino event was detected during a flare of the blazar 3C279 at 0.56° from the source, as shown in Figure 2.18.

A search for a diffuse flux of cosmic neutrinos has been performed on the basis of the different spectral shape of the expected cosmic diffuse flux, proportional to E_ν^{-2}, with respect to the atmospheric flux of neutrinos, which is proportional to $E_\nu^{-3.7}$ at high energies (Aguilar et al., 2011b). A robust energy estimator for the candidate neutrino events has been adopted, based on the average number of hit repetitions at the OMs used by the reconstruction algorithm. Repetitions are defined as the number of hits within 500 ns. The distribution of the energy estimator parameter obtained for the data is compared with the Monte Carlo prediction of an atmospheric neutrino flux that includes a Bartol model plus the maximum contribution from a prompt model (using the Recombination Quark Parton Model, RQPM). The 90% confidence level upper limit set for an E_ν^{-2} spectrum is $E^2\phi^{90\%CL} = 5.3 \times 10^{-8}\mathrm{GeV\ cm^{-2}\ s^{-1}\ sr^{-1}}$ in the energy range 20 TeV-2.5 PeV. In Figure 2.19, the ANTARES result is compared with those obtained by other experiments.

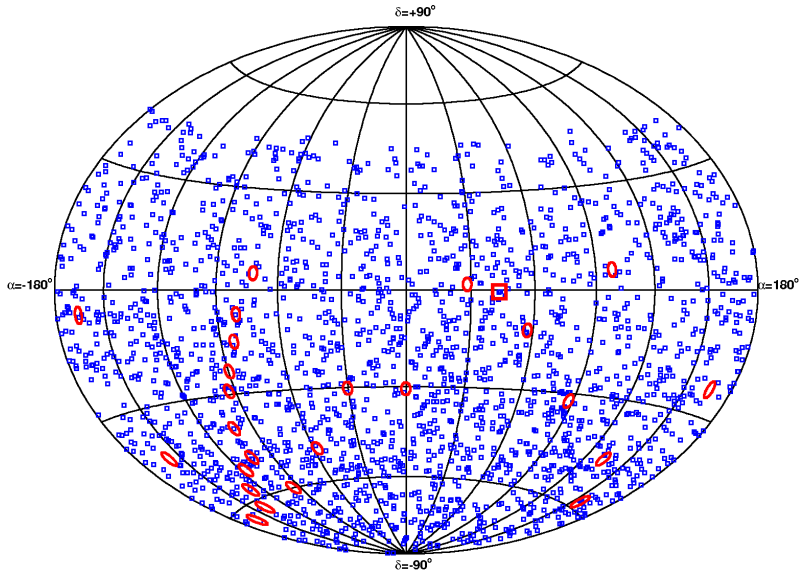

(a)

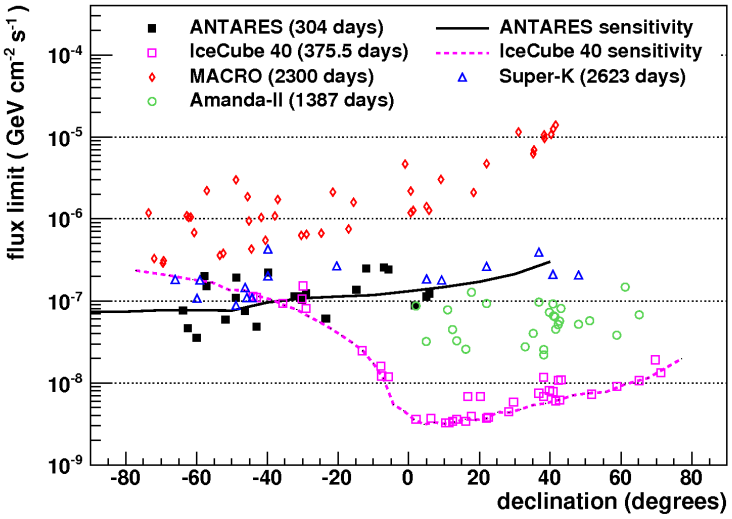

(b)

Figure 2.17: *Top: sky map of the candidate neutrino events selected in the 2007-2008 data (blue squares), used for the search of point-like neutrino sources. The red circles represent the candidate sources. The red square indicates the most significant cluster of events obtained from the full sky search. Bottom: limits set on the normalization ϕ of an E_ν^{-2} spectrum of high-energy neutrinos from selected candidates. The points show the 90% CL limit at the declination of the candidate source. From (Adrián-Martínez et al., 2011a).*

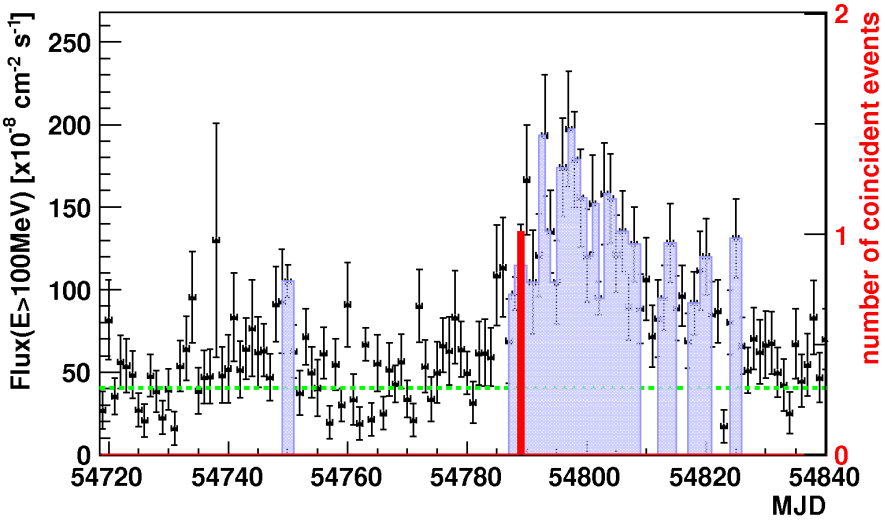

Figure 2.18: *Gamma-ray light curve (dots) of the blazar 3C279 measured by the LAT instrument onboard the Fermi satellite above 100 MeV. The light shaded histogram (blue) indicates the high state periods. The dashed line (green) corresponds to the fitted baseline. The red histogram displays the time of the associated ANTARES neutrino event. From (Adrián-Martínez et al., 2011c).*

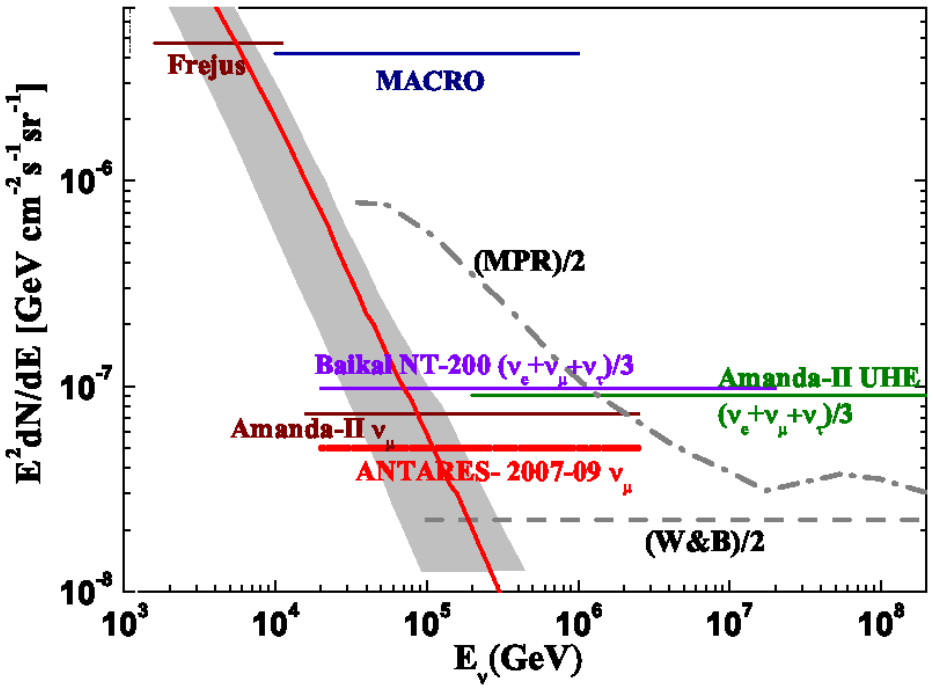

Figure 2.19: *ANTARES 90% C.L. upper limit for an E_ν^{-2} diffuse high energy $\nu_\mu+\bar{\nu}_\mu$ flux, compared with the limits from other experiments. The grey band represents the expected variation of the atmospheric ν_μ flux: the minimum is the Bartol flux from the vertical direction; the maximum the Bartol + RQPM flux from the horizontal direction. The central line is averaged over all directions. From (Aguilar et al., 2011b).*

2.3.7 The KM3NeT project

The institutes currently involved in ANTARES are also part of an extended consortium whose aim is to build, deploy and operate a neutrino telescope of a km^3 size in the Mediterranean Sea: the KM3NeT[6] detector. The KM3NeT consortium is composed of 40 institutes or university groups from 10 countries around Europe, which have been involved in the three pilot projects that have tested the technologies to implement in the final detector. Other than the french based ANTARES, the other two pilot projects are the Italian based NEMO[7] (Migneco et al., 2006) and the Greek based NESTOR[8] (Aggouras et al., 2006), each providing also a submarine site candidate to host the final detector.

Detailed studies have been conducted in order to define the detector configuration that maximizes the effective area and minimizes the sensitivity to cosmic neutrino sources. Several solutions have been proposed for the configuration of the OMs, their electronics, the data readout and transport and the detector geometry; these are reported in the Technical Design Report (The KM3NeT Consortium, 2010). Besides the classic OM scheme described in § 2.3, though with a slightly smaller PMT of 8", a layout has been proposed in which 31 small sized PMTs (3") are contained in a single OM. A 13" glass sphere is used in both cases. Both solutions have their pros and cons: whereas the single PMT scheme has been widely used and tested in several experiments, including ANTARES, the multi PMT optical module would allow a better separation of multiple photon hits at the OM, thus improving, in principle, the rejection of background hits. The adoption of one OM scheme rather than the other is strictly tied to the choice of the geometry of the detection units (DUs), the analogue of ANTARES lines, for which three options are taken into consideration. The *Bar* detection unit consists in a semi-rigid mechanical structure composed of horizontal bars, the storeys, interlinked by a system of cables that forces each bar to assume an orientation perpendicular to its vertical neighbours after the deployment. Each storey hosts three couples of OMs, two at the sides of the bar and one in the middle. In the Bar layout, OMs with a single PMT are adopted. A *String* detection unit has also been proposed, which involves the adoption of storeys with one multi PMT optical module, spaced along the string by 30 m. This layout offers the minimal hydrodynamical drag. Finally, the *Triangle* detection unit involves storeys formed by a circular structure hosting three couples of OMs (of single PMT type) placed at an angular distance of 120° from each other with respect to the centre of the storey. The full detector will contain about 320 bar, 280 triangle or 620 string units. Among the parameters considered in the optimization of the detector performances is the distance between the detection units. Simulations show that the best sensitivity is obtained for DU distances of 180 m for the bar design and 130 m for the string design. The three layouts just described are sketched in Figure 2.20.

Besides the detection units, the underwater infrastructure also includes a main electro optical cable, for the power and data transmission, a primary junction box,

[6]**KM3 Ne**utrino **T**elescope
[7]NEutrino Mediterranean Observatory
[8]Neutrino Extended Submarine Telescope with Oceanographic Research

Figure 2.20: *Sketch of the three detection unit layouts proposed for KM3NeT. From left to right: the bar, the string and the triangle layout (see text).*

for the conversion of high voltage to medium voltage, two secondary junction boxes, and the cabling between primary and secondary junction boxes and between the latter and the detection units. The design and construction of such a detector thus represents a technological challenge, since it would be the biggest underwater neutrino telescope ever built. The total electrical power needed by the underwater infrastructure is estimated to be around 96 kW for the detection units plus 10 kW for the associated science nodes. Due to the power losses at the different stages of the transmission, a total power of 155 kW will have to be provided from shore. The expected data flow is of the order of 0.2 Tb/s, which can be accommodated on a number of optical fibres using dense wavelength division multiplexing (DWDM) techniques. This data rate also exceeds any data storage capacity by several orders of magnitude, hence the filtering of the data onshore by dedicated trigger algorithms is mandatory.

The performances of the final detector have been evaluated by means of Monte Carlo simulations. Figure 2.21 shows the effective area of the final detector to upgoing neutrinos as a function of the neutrino energy. Depending on the applied quality cut, the effective area at 1 TeV is between 20 and 100 times that of ANTARES. In Figure 2.21 is also shown the cumulative point spread function of the final detector for a neutrino flux with a E_ν^{-2} spectrum. The median angular resolution is about 0.1°, which is an improvement of a factor of five with respect to ANTARES. KM3NeT is expected to reach a sensitivity to the search for point sources of $\phi_\nu = 2\times10^{-9}$GeV cm^{-2} s^{-1} on the flux normalization for an E_ν^{-2} neutrino flux after one year of data taking, which is an improvement of more than a factor 10 with respect to ANTARES (see Figure 2.22).

The construction of the KM3NeT detector is of uttermost importance for neutrino astrophysics, since it would cover with unprecedented sensitivity the southern sky, which includes the most part of the Milky Way, complementing the portion of the sky not covered by IceCube.

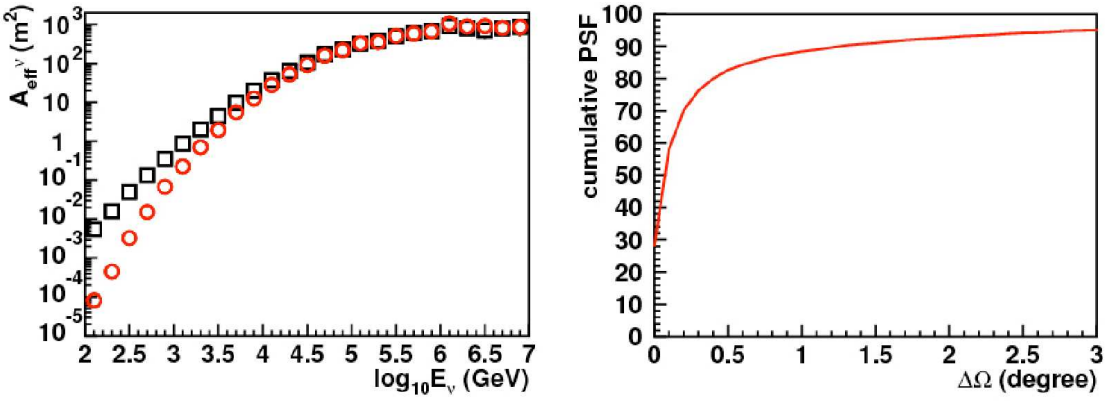

Figure 2.21: *Left: expected effective area to upgoing neutrinos of the final KM3NeT detector as a function of the neutrino energy for stricter (red) and a looser (black) quality cuts, still maintaining a reasonable angular resolution. Right: cumulative point spread function of the final KM3NeT detector for a simulated neutrino source with a E_ν^{-2} spectrum. From (The KM3NeT Consortium, 2010).*

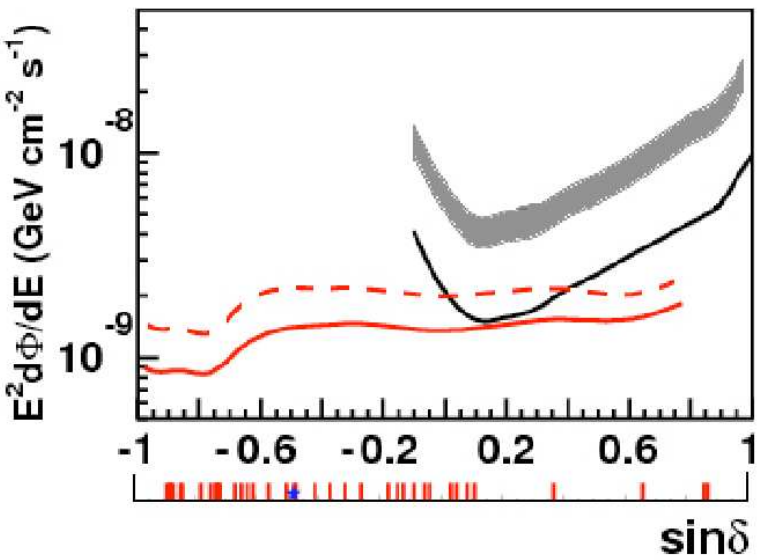

Figure 2.22: *Sensitivity of the full KM3NeT detector to neutrino point sources with an E_ν^{-2} spectrum for one year of observation, as a function of the source declination. The red lines indicate the 90% CL flux sensitivity (full line) and the 5σ discovery flux with 50% probability (dashed line).*

Chapter 3

Simulation tools and muon track reconstruction in ANTARES

This chapter describes the main software tools used to simulate the flux of particles at the detector and the detector response. In addition, the algorithms used to reconstruct the muon tracks in both simulation and data analysis are also presented.

3.1 Monte-Carlo simulation

The simulation chain used in this analysis comprises the generation of neutrinos and atmospheric muons, their propagation and interaction in the vicinity and within the detector and the detector response. A typical software chain is shown in Figure 3.1. The various computer codes used in this work are described below.

3.1.1 Muon neutrino generation

High energy neutrinos are generated using the code `GENHEN` (Bailey, 2004). This program generates a flux of neutrinos with uniformly distributed directions within a defined zenith angle interval θ_{min}-θ_{max}, with a power law energy spectrum E_ν^{-X}, called the "generation spectrum", and within a certain "generation volume" surrounding the detector. First the neutrino position, direction and energy are generated, then its interaction is simulated using the code `LEPTO` (Ingelman et al., 1997) and `RSQ` (Barr, 1987), for deep inelastic scattering and resonant/quasi-elastic interactions, respectively. The secondary particles issued from the interaction are stored for further processing only if they are deemed to produce some detectable light at the PMTs. For this reason, a sensitive volume, called "the can" (Figure 3.2), is defined in such way that the Cherenkov light produced outside of it has a small probability of being detected. The muons issued from neutrino interactions are kept only if they intersect the can surface.

Although the neutrinos are generated with a defined energy spectrum E_ν^{-X}, they can be used to simulate any user specified spectrum by using a weight assigned to each event at generation time and stored in the output files. The generation weight

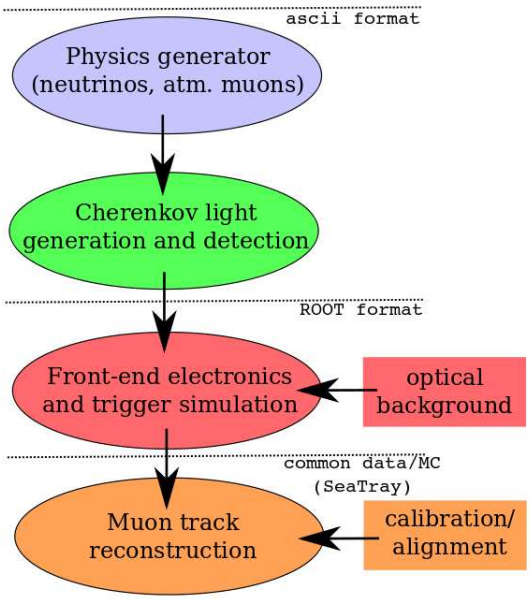

Figure 3.1: *Software chain for the Monte Carlo simulation and data analysis. Track reconstruction software runs on both Monte Carlo and calibrated data.*

W_{gen} is given by:

$$W_{gen}^{-1} = \frac{N_{total}\ E_\nu^{-X}}{I_E\, I_\theta\, V_{gen}\, \sigma_{CC}(E_\nu)\, \rho\, N_A\, P_{Earth}(E_\nu, \theta_\nu)} \tag{3.1}$$

where N_{total} is the total number of generated events. I_E is the energy phase space factor defined as the integral of the generation spectrum E^{-X} over the generated energy range. The term V_{gen} represents the generation volume, which multiplied by the charged current interaction cross section $\sigma_{CC}(E_\nu)$, the medium density ρ and the Avogadro's numbers N_A, gives the effective interaction area at that energy. The possibility for neutrinos to be absorbed by the Earth is accounted for in the term P_{Earth}. In order to reproduce a certain neutrino flux $\phi^{model}(E_\nu, \theta_\nu)$, each event has to be assigned a weight W_{event} which depends on the generation weight as

$$W_{event} = W_{gen} \cdot \phi^{model}(E_\nu, \theta_\nu) = W_{gen} \cdot \frac{\mathrm{d}N_\nu^{model}}{\mathrm{d}E_\nu\ \mathrm{d}S\ \mathrm{d}t}\,. \tag{3.2}$$

In the simulations used in this thesis, neutrinos have been generated over a 4π solid angle ($\theta_{min} = 0$ and $\theta_{max} = \pi$), with a generation spectral index $X = 1.4$ and with energies between 100 and 10^8 GeV. For the simulation of atmospheric neutrinos the Bartol model has been used (Agrawal et al., 1996), whose event weights are provided by the program itself.

3.1.2 Atmospheric muons generation

Two approaches are used in ANTARES for the simulation of the flux of atmospheric muons that reach the detector from above. One involves a full simulation of the interaction of the cosmic rays (protons and nuclei) in the atmosphere and

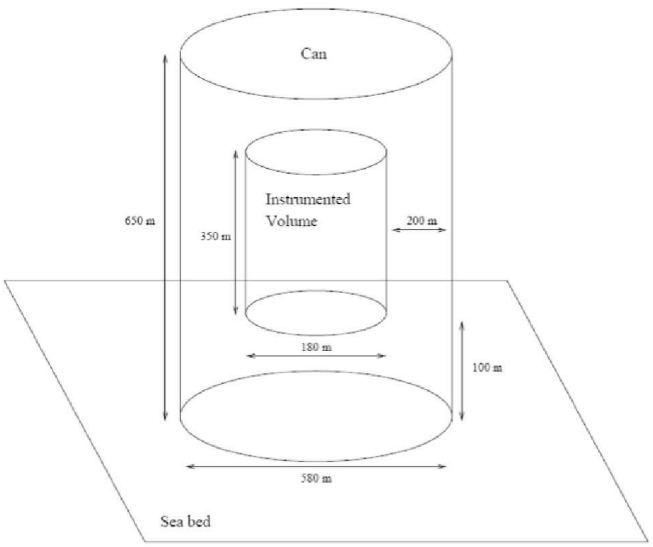

Figure 3.2: *Schematic view of the ANTARES can. The can extends about two and an half absorption lengths, both radially and vertically, away from the instrumented volume.*

the propagation of the secondary particles down to the sea level and then to the detector. This kind of simulation, which is very CPU-expensive, is done with the code `CORSIKA`[1] (Heck et al., 1998). It is used to simulate cosmic rays in a zenith angle interval within 0°-85° and energy per nucleon between 10^3-10^8 GeV. The development of the hadronic shower in the atmosphere is simulated with the `QGSJET` model (Bossard et al., 2001).

The other approach for generating atmospheric muons uses a fast algorithm that simulates the flux of atmospheric muons by means of parametric formulae that describe the angular distribution of muon bundles at the detector (Becherini et al., 2006). The formulae have been extracted from the full simulation code `HEMAS`[2] (Scapparone, 1999) and are implemented in the `MUPAGE`[3] code. The latter has been used in this thesis to simulate the atmospheric muon flux. `MUPAGE` generates the events for a user specified data acquisition time, so that no weighting is needed. As said already, the main advantage of this program is the computational speed, much faster than the full simulation, e.g. the generation of a data set with a live time equivalent to one month requires about 300 hours of CPU time on a 2xIntel Xeon Quad Core, 2.33 GHz with `MUPAGE`.

3.1.3 Photon generation, propagation and detection

The simulation of Cherenkov photons emitted along the muon and electron tracks and the generation of the photon hits at the OMs is done by the package `KM3` (Bailey, 2004; Navas et al., 1999). This code simulates the propagation of muons in water using the `MUSIC` library (Antonioli et al., 1997), taking into account the

[1] COsmic Ray SImulations for KAscade
[2] Hadronic, Electromagnetic and Muonic components in Air Showers
[3] MUon GEnerator from PArametric formulae.

energy losses due to ionization, bremsstrahlung, photonuclear interaction and pair production. The code divides energy losses into a *continuous* part (energy loss < 1 MeV), calculated at each propagation step, and a *stochastic* part (energy loss > 1 MeV), sampled according to the known muon cross section. The angular and lateral deflection of muons due to multiple Coulomb scattering is also simulated.

Once the energy loss profile of the muon track, including the shower locations, is simulated, the hits produced by Cherenkov photons at the OMs are generated. Since generating and following each single photon would be too CPU consuming, the strategy adopted by the `KM3` package consists in using precomputed hit probability tables. The package is thus subdivided into three tools, two of which take care of generating the probability tables, whereas the third one runs the actual simulation. The three programs composing the `KM3` package are:

`gen` : this program implements a complete `GEANT3` simulation of Cherenkov light prodution from relativistic electrons and muons travelling in water. Photons are produced for a short muon track segment (from 1 to 2 m) or an electromagnetic shower, and their positions and properties are recorded at concentric spheres of various radii centered on the origin. The program output consists of some tables containing all the photons recorded at each spherical shell. The photon propagation is done taking into account light absorption and scattering, according to the values shown in Figure 3.3, as well as the dependence on the wavelength of the group velocity.

`hit` : this program creates the hit distributions at the OMs for muon track segments and electron showers, using the photon tables created by `gen`. It creates the probability distributions for hits caused by direct and scattered light, sampling them for various distances and inclinations of the OM with respect to the source of the Cherenkov light. In calculating the hit probability, this program takes into account the features of the OMs, as the collection efficiency, the quantum efficiency and the transmission factor of the gel and glass sphere. The efficiency of detection of an OM depends also on the incident angle and is maximal for head-on photons. The quantum efficiency of the PMTs and angular acceptance of the OMs are shown in Figure 3.4.

`km3mc` : this program propagates each incoming muon using the `MUSIC` library, generating the secondary showers according to the energy loss profile. For each muon track segment and generated shower, it produces the hits at the OMs according to the probability tables produced by `hit`.

An additional code, `geasim`, provides the same functionality as `KM3` with a different implementation. It generates the hits at the OMs by means of a full `GEANT3` simulation of photon production, instead of using probability tables as for `km3mc`. The tracking of each photon, though, is performed in straight lines, i.e. neglecting the light scattering. This simplified assumption drastically reduces the computational time, since photons that do not hit any of the OMs can be easily discarded from the simulation by geometrical considerations. To add a further speed up, this code simulates particle showers as single electrons. This *one particle approximation* has been tested and proved to be reliable.

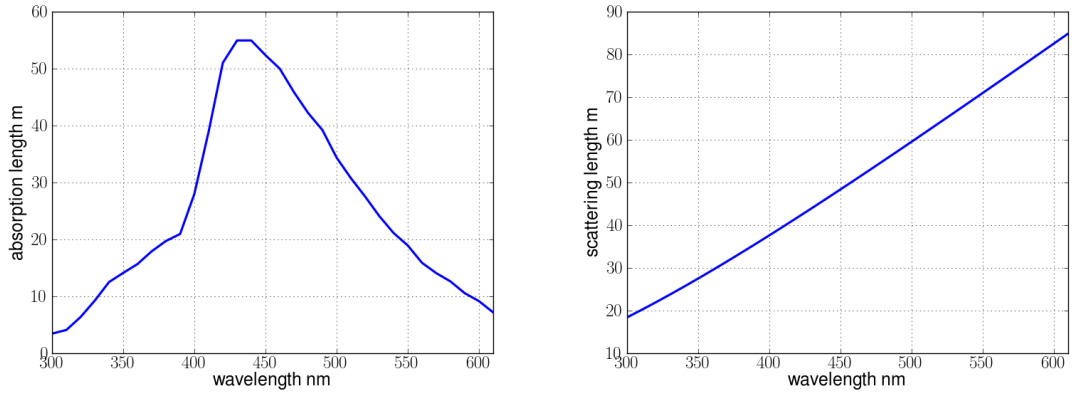

Figure 3.3: *Wavelength dependence of the absorption (left) and scattering (right) lengths used in Monte Carlo for the propagation of Cherenkov photons in water.*

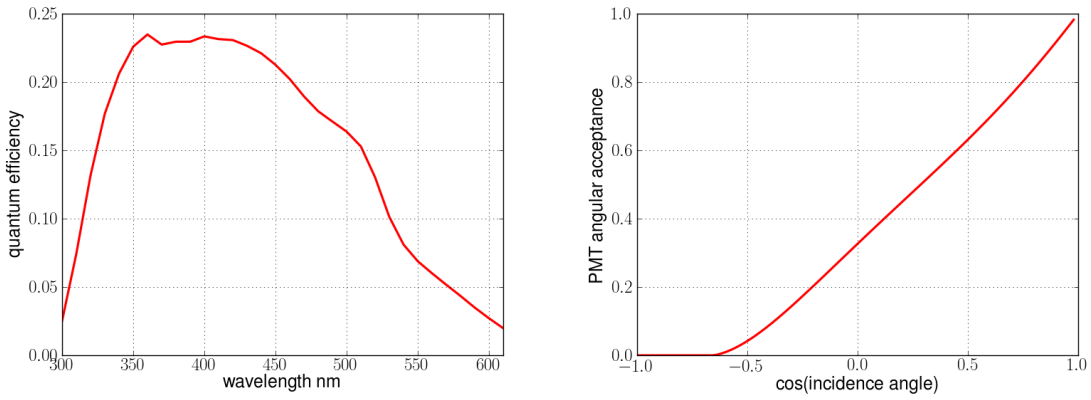

Figure 3.4: *Left: wavelength dependence of the quantum efficiency of a PMT. Right: angular acceptance of an optical module as a function of the incidence angle of the photon.*

3.1.4 Front-end electronics and trigger simulation

The simulation of the detector response is accomplished by the code `TriggerEfficiency` (de Jong, 2009). This code simulates the conversion of the single photon hits at the OMs into an analog charge signal at the PMT output by taking into account the conversion efficiency. The time of the hit is generated according to the *transit time spread* distribution measured during the characterization of the ANTARES PMTs. Further, an early after-pulse is generated with a preset probability of 0.5%.

The digitization of the hit by the ARSs is also simulated. The time stamping and the time interpolation (TVC) is computed using the TVC calibration of the ARS. The walk effect, i.e. time delay due to the finite rise time, is taken into account. The charge of consecutive pulses are added during a fixed time period corresponding to the integration period of the ARS. The value of the integrated charge (AVC) is computed using the charge calibration of the ARS.

3.1.5 Generation of the optical background

The `TriggerEfficiency` program also takes care of generating the background hits at the OMs according to the single rates found in real data. Raw data files come with a dedicated data structure that contains a summary of the recorded single rates at each OM encountered during the data taking. This data structure is used to simulate the single rates proper of each data run. Background hits are assumed to be randomly distributed, so that the time difference between two consecutive hits follows an exponential distribution whose characteristic time is the inverse of the simulated single rate.

3.2 Muon track reconstruction

The reconstruction of muon tracks is a fundamental task to perform astronomy with a neutrino telescope. At present, two different strategies are adopted in ANTARES for track reconstruction: a maximum likelihood algorithm and a fast algorithm used for online reconstruction. The latter also performs the reconstruction of "bright points", i.e. spherical-like flashes of light in the detector caused by showers. The reconstruction algorithm adopted can also have an impact on the resulting angular resolution and acceptance of the detector.

A muon track crossing the detector is fully determined by 5 parameters, which define its starting point $\vec{p_0} = (x_0, y_0, z_0)$ (at the time $t = t_0$) and its direction $\vec{d} = (d_x, d_y, d_z)$. In a polar coordinate frame the direction can be defined in terms of the zenith angle θ and the azimuth ϕ as $\vec{d} = (\sin\theta\cos\phi, \sin\theta\sin\phi, \cos\theta)$. The task of reconstructing a muon track consists in estimating the set of 5 parameters $(\theta, \phi, x_0, y_0, z_0)$.

Muon track reconstruction exploits the geometrical features of Cherenkov light in order to estimate the track parameters. The expected arrival time of photons at

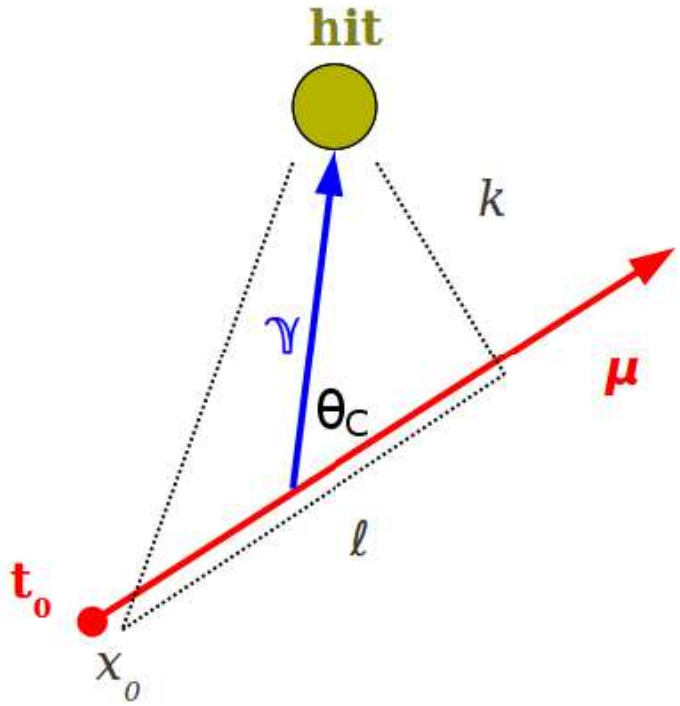

Figure 3.5: *Geometric representation of the detection of a Cherenkov photon (in blue) emitted by a muon (red) and generating a hit at an optical module (yellow).*

the OMs is illustrated in Figure 3.5 and is given by:

$$t_{exp} = t_0 + \frac{1}{c}\left(l - \frac{k}{\tan\theta_C}\right) + \frac{1}{v}\frac{k}{\sin\theta_C} \tag{3.3}$$

where k is the distance of closest approach of the track to the OM, l is the path length travelled by the muon between the starting point at $t = t_0$ and the point of closest approach, θ_C is the Cherenkov angle, c is the speed of light, at which the muon is assumed to travel, and v is the speed of light in water. For every set of track parameters it is possible to calculate the expected arrival time t_{exp} of Cherenkov photons at each OM position. The difference $r = t_{hit} - t_{exp}$ between the detected hit time and the expected time is called a *time residual*.

All track reconstruction algorithms used in ANTARES perform a preliminary selection of the hits in order to reject as many background hits as possible. Based on this reduced set of hits, the algorithms make use of appropriate estimators, which are function of the time residuals, in order to find the best set of track parameters. Different estimators can be used in sequence in order to provide at each step a more refined result. The first step which provides the starting point to all subsequent estimations is called a *prefit*, which is normally obtained by means of a linear fit.

The selection of neutrino events could be done in principle by selecting all the upward going tracks among the reconstructed ones. This criterion alone however proves not to be sufficient due to the high contamination of downward-going atmospheric muons which are mis-reconstructed as upgoing. Muon bundles, in particular, are thought to contribute to this background. Track reconstruction algorithms must

thus provide one or more suitable quality parameters that allow the discrimination of mis-reconstructed muons and the selection of a sample of neutrino events, whose purity can be tuned by varying the cut on the quality variable.

The reconstruction algorithms and the relative quality parameters are described in more detail in the following sections.

3.2.1 Maximum likelihood algorithm

This reconstruction strategy is based on a multi-step likelihood maximization of the distribution of the time residuals (Heijboer, 2004). It is implemented in a package called `aafit`. It performs a hit selection, a linear prefit, an M-estimator fit, a "simplified" likelihood maximization and a full likelihood maximization. These steps are described below.

Hit selection and track prefit - step 0

The hit selection implemented in this algorithm is based on a causality filter. Two hits are causally related if:

$$|t_i - t_j| < \frac{d_{ij}}{c} + 20 \text{ ns} , \tag{3.4}$$

where $t_{i,j}$ is the hit time, d_{ij} is the distance between the OMs and the 20 ns account for the uncertainty on the OMs positions. The goal of this hit selection is to let as many hits as possible into the reconstruction process, in order to maximize the information available to improve the precision of the final result.

In order to reduce the impact of PMT afterpulses[4] on the reconstruction, all the hits selected on the same OM using the causality filter are merged within a time window of 300 ns.

The first estimate of the track parameters is given using a linear least squares fit based on the simplified assumption that all the hits occur on points that are located in the muon track. This linear problem is resolvable analytically and the resulting track parameters that minimize the χ^2 are easily obtained, although with a poor precision.

M-estimator fit - step 1

M-estimators (where "M" stands for "maximum likelihood-type") are a broad class of functions that allow parameter estimation even when the probability distribution function that defines the problem is not exactly know. They are referred to as *robust estimators* when the result is insensitive to small deviations from the underlying distribution assumed.

This kind of estimator is used by the algorithm to improve the result obtained by the prefit. The function that is maximized to estimate the track parameters is:

$$M = \sum_i \kappa(-2\sqrt{1 + A_i r_i^2/2}) - (1-\kappa) f_{ang}(a_i) \tag{3.5}$$

[4]Afterpulses are delayed pulses that arrive up to several hundreds of nanoseconds after the main pulse due to internal feedback in the PMT.

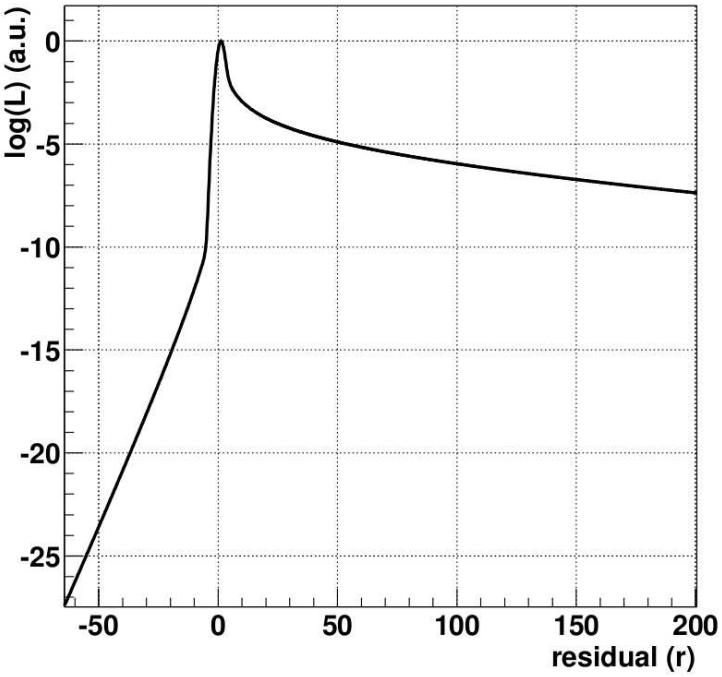

Figure 3.6: *The simple PDF of time residuals used in the maximum likelihood track fit. This PDF does not take into account the background hits.*

where A_i is the hit amplitude, r_i the time residual, f_{ang} is the angular acceptance of the PMT as a function of the incident angle of the photon a_i. The weight κ is a tunable parameter whose optimum value was found to be 0.05. The contribution of each hit to the estimator is quadratic for small values of r_i and linear for large values of r_i. This behaviour assures that background hits with large time residuals do not seriously affect the fit result, thus providing the required robustness. Further, this estimator is shown to be only slightly sensitive to the starting point provided by the prefit. For this reason it is a mandatory step to improve the track estimate before using the maximum likelihood estimators, which are instead very sensitive to the starting point due to the higher number of local minima.

Maximum likelihood fit

The procedure of maximum likelihood fitting is based on the definition of a suitable probability distribution function (PDF) which describes the distribution of the time residuals in an event containing a muon track, with respect to the true track. On this basis, one can calculate the likelihood of each set of track parameters as:

$$\mathcal{L} = P(\text{event}|\text{track}) = \prod_i P(r_i) \ , \tag{3.6}$$

where $P(r)$ is the distribution of the time residuals. In this algorithm two degrees of approximation are used for the $P(r)$, these are described below.

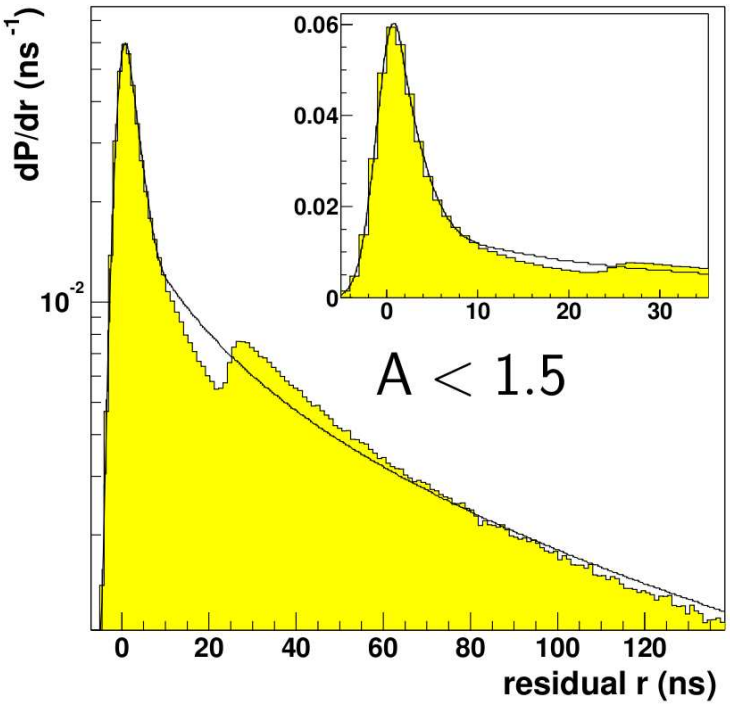

Figure 3.7: *The full PDF of the time residuals used in the last step of the maximum likelihood track fit. In yellow the histogram obtained by the Monte Carlo, the solid line is the parameterization used by the likelihood fit.*

Simple PDF - step 2 The first step of the maximum likelihood fit is done using a PDF which does not include the distribution of background hits. This PDF is shown in Figure 3.6 and takes into account the smearing on the hit times introduced by the transit time at the PMTs, which tunes the width of the peak at zero, and the scattering of light in water, which causes the long tail at positive values. An unphysical tail is present at values below -5 ns. This was introduced to render the PDF differentiable at negative values in order to help the fitting routine.

Due to the restrictions of the PDF, the hits used in this fit are refiltered in order to reduce the contribution of background hits. The selection is done on the basis of the result of the M-estimator fit, by including all the hits with time residuals between $-0.5 \times R$ and R, where R is the root mean square of the residuals used for the M-estimator fit.

This fitting step is also used to provide a track estimate as precise as possible to initialize the following last reconstruction step. This is done by repeating steps 1 and 2 using different starting points of the prefit track (step 0). Four starting points are obtained by rotating the prefit track by 25°. The rotation is done about the track point which is closest to the center of gravity of the selected hits. Four more trials are done by translating the starting point of the track by ± 50 m in the direction $\vec{d} \times \hat{z}$ and by ± 50 m in the $\hat{z}$ direction. Among the 9 trials, the track with the best likelihood is retained, together with the number of trial tracks N_{comp} that were compatible with it, i.e. those whose direction was at most 1° far from the chosen track. The number N_{comp} will contribute in the final cuts to define the quality of the final fit.

Full PDF - step 3 The final result of the track fit is given by maximizing a likelihood that uses a full PDF of the time residuals. This PDF, which is show in Figure 3.7, takes into account the background hits and the effects of the front-end electronics. The peak at around 25 ns is due to the integration time of the ARS chip (cf. §2.3.1).

The hits used in this step are a subset of the ones selected using the causality relation. The selection is performed on the basis of the track result obtained at the previous step, selecting all the hits with time residuals between −250 and 250 ns and within 100 m from the track, or those belonging to local coincidences.

Selection criteria and performances

The value of the likelihood $\mathcal{L}^{max}$ issued from the full PDF fit is used to define a quality parameter of the reconstructed track. The quality parameter adopted is defined as:

$$\Lambda = \frac{\log \mathcal{L}^{max}}{N_{dof}} + 0.1(N_{comp} - 1) \ , \tag{3.7}$$

where $N_{dof} = N_{hits} - 5$ is the number of degrees of freedom of the fit and is equal to the number of hits used by the reconstruction algorithm minus the number of fitted parameters. The last term, instead, acts as an ad hoc reward for fits with $N_{comp} > 1$.

The track reconstruction algorithm provides a second quality parameter to further reduce the contamination of mis-reconstructed downgoing muons to the sample of upgoing tracks. This is the angular error estimate of the reconstructed track which is calculated from the shape of the likelihood at the maximum and is referred to as :

$$\hat{\beta} = \sqrt{\sigma_\theta^2 + \sin^2\theta\sigma_\phi^2} \ , \tag{3.8}$$

where σ_θ and σ_ϕ are the error estimates of the track's zenith and azimuth respectively. As shown in Figure 3.8, neutrinos and mis-reconstructed muons have different distributions of $\hat{\beta}$, allowing it to be used as a quality parameter.

The distributions of the quality parameters just described are shown in Figure 3.8. By applying suitable cuts on the variables shown it is possible to select a pure sample of neutrino events.

3.2.2 Online reconstruction (`BBfit`)

This reconstruction algorithm is used for the online monitoring of the triggered events and the data analysis. It is implemented in the package called `BBfit` (Aguilar et al., 2011a). The speed needed for the online processing of data has imposed the use of a simplified detector geometry, which is considered by the algorithm with the following approximations:

- detector lines are considered to be perfectly vertical, thus ignoring line displacements due to sea currents.
- instead of three OMs, storeys are considered containing only one OM located directly on the detector line with an axis-symmetric field of view. The signals of the three PMTs within one storey are combined.

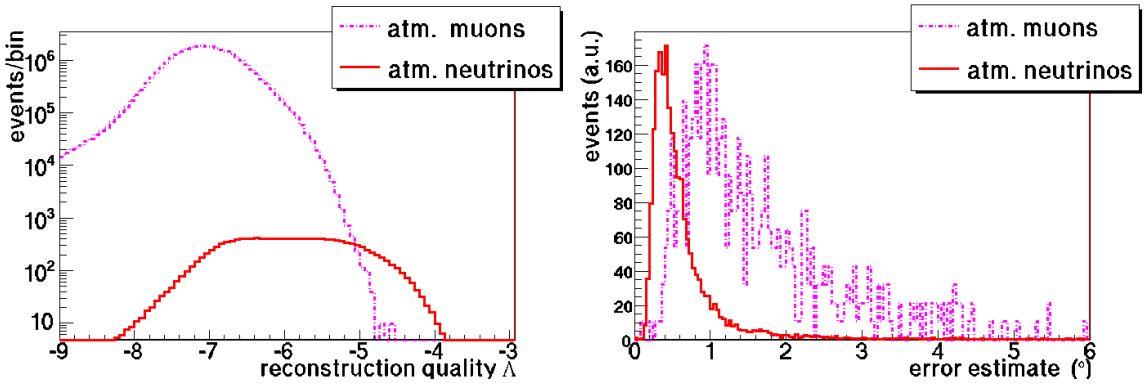

Figure 3.8: *Left: reconstruction quality Λ for upgoing reconstructed tracks from Monte Carlo. Right: angular error estimate of reconstructed upgoing tracks, with $\Lambda > -5.6$. Atmospheric neutrinos are in red, mis-reconstructed atmospheric muons are in magenta.*

This strategy adopts a hit selection, a linear prefit, a χ^2-fit and an M-estimator fit. These steps are described more in detail below.

Hit merging and selection

The use of a simplified storey geometry imposes that all the hits detected on the same floor which are in coincidence within 20ns are merged into one. The time of the resulting hit is that of the earliest among the merged hits, whereas its charge is given by the sum of the participating charges. A bonus charge of 1.5 photoelectrons assigned only once to a merged hit. This increases the weight of local coincidences in the track fit with respect to isolated hits. Among the resulting merged hits, those with a charge bigger than 2.5 photoelectrons are called L1s[5].

The hit selection is then based on the presence in the event of so called T3 coincidences, defined as a coincidence between two L1s in adjacent floors within 80ns or between next-to adjacent floors within 160ns. Only those lines with at least one T3 will be used for the further hit selection and thus for the reconstruction. In order for the reconstruction to proceed, at least one T3 must be found in the detector, and all T3 hits will participate in the track fit. The last step of the hit selection consists in adding those hits whose times are compatible with a linear extrapolation of the times of the T3 hits along the same line. The list of selected hits thus obtained is sent to the reconstruction described in the next paragraph.

The hit selection described here is strongly focused on coincidences between close by OMs, resulting in a stricter selection than the one based on the causality filter. This feature makes it stable with respect to the fluctuation of the optical background rates due to the bioluminescence and provides robustness to the whole algorithm.

[5]This definition of L1, though not identical, is similar to that given in §2.3.1. Due to the bonus charge of 1.5 photoelectrons, almost all floor coincidences within 20 ns will pass the threshold of 2.5 photoelectrons and be considered L1s.

Modified-χ^2 fit

This reconstruction step is based on the minimization of an estimator that depends on the quadratic sum of the time residuals (a χ^2 term), plus an additional term that depends on the charge of the hits. The quantity which is minimized to estimate the track parameters is:

$$\tilde{\chi}^2 = \frac{1}{N_{dof}} \sum_{i=1}^{N_{hit}} \left[\left(\frac{r_i}{\sigma_i} \right)^2 + \frac{a(a_i)d(d_\gamma)}{\langle a \rangle d_0} \right] , \tag{3.9}$$

where:

- $r_i = t_{hit,i} - t_{exp,i}$ is the time residual of the hit,
- $a(a_i)$ is the amplitude of the hit corrected for the angular acceptance of the floor, with a saturation at 10 photoelectrons,
- σ_i is the uncertainty on the time of the hit, estimated as 10 ns when $a_i > 2.5$ photoelectrons and 20 ns otherwise,
- $\langle a \rangle$ is the mean of the hit amplitudes corrected for the angular acceptance of the floor,
- d_γ is the travel path of the photon with a lower bound at 5 m,
- d_0 is a normalization weight set to 50 m. This value is motivated by the fact that at this travel distance a photon hitting an OM head on produces on average a single photoelectron signal,
- $N_{dof} = N_{hits} - 5$ is the number of degrees of freedom, N_{hits} is the number of hits used in the reconstruction.

The second term in Eq. 3.9 is introduced as a penalty to high charge hits that correspond to long travel path of the incident photon. The `BBfit` algorithm can use the estimator of Eq. 3.9 to reconstruct for each event both a track and a shower. The two cases differ in the way of calculating the expected arrival time of the photon at the PMT used to obtain the residuals, which is modeled as an isotropic emission from a single point in the case of a shower. According to the number of lines involved in the hit selection, one can have single-line or multi-line fits. In the case of a multi-line fit all the track parameters $(\theta, \phi, x_0, y_0, z_0)$ and bright point parameters (x_0, y_0, z_0, t_0) are calculated. Meanwhile for a single-line fit the azimuth information is lost in both cases, leading to these track parameters (θ, t_0, z_0, d_c) and bright point ones (z_0, t_0, d_c), where d_c is the distance of closest approach of the track from the line used in the reconstruction, or simply the distance of the shower from the line.

Resolution of the azimuth degeneracy

When a track is reconstructed using only two lines, an ambiguity is introduced on the reconstructed azimuth angle. The reason for this is that the distribution of the hit times of the "true" track and the track obtained by mirror symmetry with

respect to the plane connecting the two lines are the same. The "mirror" track has the same θ as the original track but rotated ϕ, according to the relation

$$\phi_{mirror} = \phi_{lines} - 2 \times \phi_{track} \,, \tag{3.10}$$

where ϕ_{lines} is the azimuth angle of the plane connecting the 2 detector lines used for the reconstruction.

Due to the rather strict hit selection described in the previous paragraph, the majority of multi-line tracks are reconstructed with only two lines. For this reason an intermediate reconstruction step has been added to this strategy in order to resolve the azimuth ambiguity. The choice between the two tracks cannot be based on the $\tilde{\chi}^2$ of Eq. 3.9, since it normally has similar values for both. In order to drive the choice, a temporary hit selection is performed for both tracks over the whole detector, selecting all the hits with time residuals less than 30 ns. The sum of the charges of the two sets of selected hits is calculated and the track corresponding to the highest value is considered to be the correct one. In this way, the best track is chosen 70% of the time and the two-line angular resolution is improved by 42% for upward-going atmospheric neutrinos and by 15% for downward-going atmospheric muons.

M-estimator fit

The last reconstruction step is based on the maximization of an M-estimator and is applied to all the tracks reconstructed with more that one line. A new hit selection is applied based on a time residual cut of 20 ns. The quantity which is maximized to estimate the track parameters is:

$$M = \sum_{i=0} \left(2 - 2 \cdot \sqrt{1 + \frac{r_i^2}{2}} \right) \,, \tag{3.11}$$

where r_i is the time residual. Note that in this estimator no information is contained about the charge of the hits.

Selection criteria and performances

The quality parameter adopted in this algorithm to distinguish the upgoing neutrinos from the mis-reconstructed muon background is the the minimized $\tilde{\chi}^2$ of Eq. 3.9. The distribution of this parameter is shown in Figure 3.9 for Monte Carlo simulations including both atmospheric neutrinos and atmospheric muons. A pure neutrino sample can be selected by applying a cut on the $\tilde{\chi}^2$. A cut $\tilde{\chi}^2 < 1.4$ ensures a 90% purity while keeping 48% of the total sample of upward reconstructed multi-line neutrino tracks.

3.3 The new software framework

The necessity to provide a common interface to perform simulations and data analysis in ANTARES, also in the perspective of the future construction and operation KM3NeT (§2.3.7), has motivated the recent adoption of a software framework.

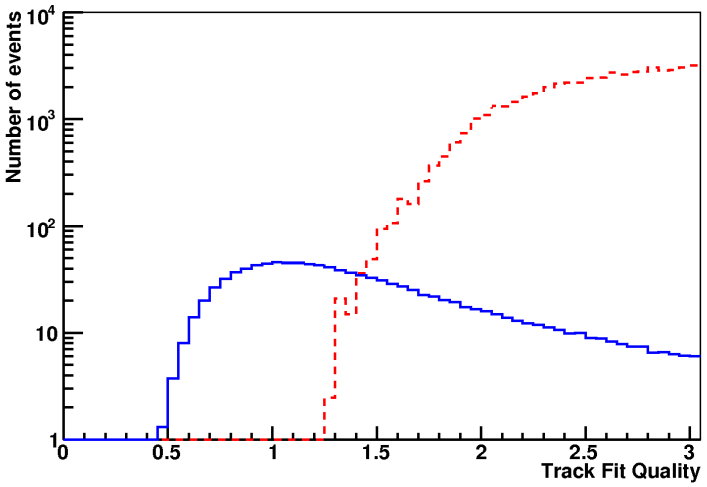

Figure 3.9: *Distribution of the quality parameter of the online reconstruction algorithm for Monte Carlo neutrinos obtained with* `CORSIKA` *(solid blue) and atmospheric muons obtained with* `MUPAGE` *(dashed red).*

A "framework" is a collection of software facilities aiming to uniformize the procedures for the creation and utilization of simulation and analysis scripts, as well as to provide a set of common implementation rules to code developers. Further, the framework must promote the modularization of the implemented algorithms and the collective contribution to their development.

`IceTray` is the software framework that was developed and is currently in use by the IceCube collaboration. The core of the system defines, among other things, the structure of the data flow, which is subdivided into *frames* (or events), and the *modules* that can interact with it. The frames can carry physics events, geometry or calibration information, whereas the modules are the algorithms that extract and process the information contained in them. The software is organized into `C++` package libraries, each providing different algorithms (modules). Libraries can also provide base *dataclasses* needed to store common use physics objects, as tracks and hits, or objects that describe the detector geometry and calibration. Base functionalities are also provided with dedicated classes for the definition of, e.g., simple directions and positions. Also, a namespace is provided for a common definition and transparent use of physics units and physics constants within the code. A `python`[6] interface is provided to each module and dataclass by means of the `boost` libraries[7]. Python scripts can be setup to configure and run simulation or analysis chains by plugging the modules needed for the task to be accomplished. No intermediate files are produced by the modules, as it would be the case if each task were performed by a different standalone program.

The `IceTray` framework has been adapted for use within the ANTARES collaboration (Kopper, 2010). For this to be possible, it has been necessary to provide a suitable reader for the data format issued from the ANTARES-DAQ and the utili-

[6] www.python.org
[7] www.boost.org

ties to implement the detector geometry and calibration. The framework currently implementes all the necessary tools to perform data analysis, including the track reconstruction algorithms described in this chapter. The framework is also used to calibrate and reconstruct the data and to apply track reconstruction to Monte Carlo simulations. The Monte Carlo generators described in this chapter are not included in the framework, neither is the simulator of the front-end electronics and trigger. Though the framework has kept its original name, the distribution that includes all the modifications and packages used in ANTARES is released under the name of `SeaTray`.

3.3.1 Implementation of `BBfit` in the framework

As part of the general effort from the collaboration to supply `SeaTray` with all the necessary software needed to perform data analyses in ANTARES, part of the work during this thesis has been dedicated to the porting of the `BBfit` reconstruction algorithm (§3.2.2) into `SeaTray` and its maintenance.

The guideline followed during the porting has been to enhance modularity, in order to take advantage of the framework architecture and encourage the use of the different parts of the software according to the need of the end users, which may differ from the original strategy. The algorithm has been split into three different modules, each performing one major task:

BBFitHitSelection : for hit merging and selection,

BBFit : for the χ^2-fit ,

BFitMEstimator : for the M-estimator fit.

The modules are intended to be joined into a single track reconstruction chain, though in principle they can also be used separately or plugged into other reconstruction strategies.

Some slight modifications with respect to the original algorithm have been made during the porting. The main ones concern the geometry used by the fitting algorithm. While it has been possible to reproduce the *one OM per floor* feature in the hit selection and the χ^2-fit, the shapes of detector lines of real data are subject to the alignment provided by the acoustic positioning and can thus move away from the vertical, whereas only vertical lines are used by the original algorithm in both data and Monte Carlo. This difference, though, is not expected to have a significant impact on the performances.

The simplified geometry of one OM per floor is abandoned at the stage of the M-estimator fit. By using the detailed detector geometry with 3 OMs per floor the angular resolution improves by $\sim 0.2°$ for tracks reconstructed with only 2 lines (Aguilar et al., 2011a).

The correction of the azimuth degeneracy, which in the original algorithm is applied only to those tracks reconstructed with 2 lines, has been extended to the tracks reconstructed with 3 and 4 lines when these are quasi-aligned. The choice between the two mirror solutions is done by selecting all the hits with time residuals

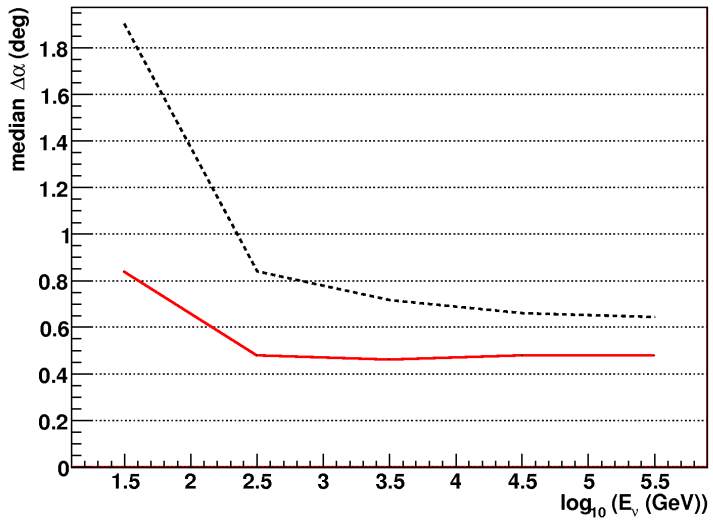

Figure 3.10: *Median angular resolution of the final M-estimator fit as a function of the neutrino energy for all multi-line tracks (dashed) and tracks reconstructed with more than 2 lines (solid), for a quality cut* $\tilde{\chi}^2 < 1.4$.

less than 20 ns for both tracks and calculating the sum of the charges weighted by the angular acceptance of the optical module

$$\text{weighted charge} = \sum_{i}^{N_{hit}} a_i \times f_{ang}(\Theta_i) \tag{3.12}$$

where a_i is the hit charge, f_{ang} the angular acceptance of the OM (shown in Figure 3.4) and Θ_i the incident angle of the photon on the OM. Selecting the track with the highest weighted charge is correct 75% of the times and improves the angular resolution by 50% for the tracks reconstructed with 2 lines.

The angular resolution of the final algorithm is shown in Figure 3.10 for tracks reconstructed with $\tilde{\chi}^2 < 1.4$. In order to validate this `SeaTray` version of `BBfit`, a comparison has been made with the standalone version. As shown in Figure 3.11 the distributions of the track quality and the cosine of the zenith angle agree with each other.

In the following of this section is given a detailed description of how to configure each module in order to run the strategy in `SeaTray`.

The module BBFitHitSelection

This module performs the hit selection and merging and can be included in a `Seatray` script as:

```
tray.AddModule("BBFitHitSelection","bbfitHitSelection")(
   ("InputPulsesName","CalibratedPulses"),
   ("OutputPulsesName","BBFitSelectedPulses"),
   ("InputTriggeredPulsesName","TriggeredPulses")#optional
   )
```

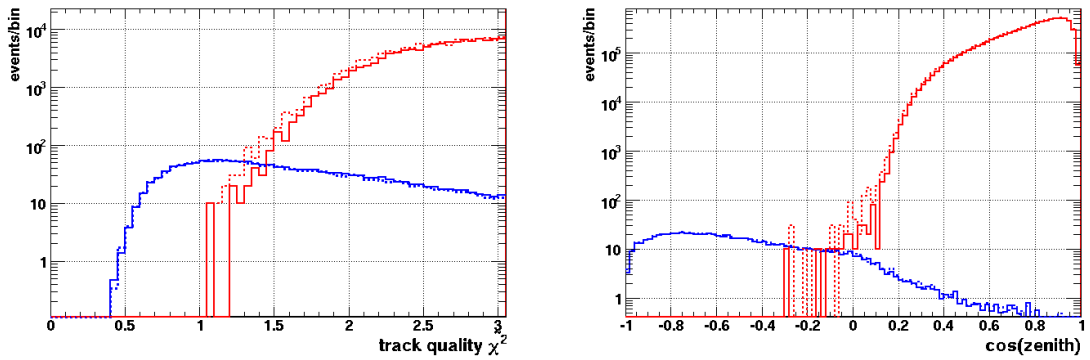

Figure 3.11: *Comparison between the distributions obtained with the standalone version (dashed) and the* `SeaTray` *version (solid) of BBfit for the track quality* $\tilde{\chi}^2$ *of upgoing tracks (left) and the cos(zenith) of all tracks with* $\tilde{\chi}^2 < 1.4$ *(right). Neutrinos are in blue, muons are in red.*

The user needs to specify the name of the frame object containing the event hits on which to perform the selection, using the field `InputPulsesName` (see also table 3.1). The name of the resulting selected pulses is set with the field `OutputPulsesName`. Both input and output pulses must be shared pointers of the type `I3RecoPulseSeriesMap`. The optional field `InputTriggeredPulsesName` allows to explicitly specify the list of triggered hits to be used by the selection.

Table 3.1: *Configurable parameters for the module* `BBFitHitSelection`

Parameter Name	type	default	description
`InputPulsesName`	string	-	name of the input event pulses in the frame
`OutputPulsesName`	string	-	name of the output selected pulses in the frame
`InputTriggeredPulsesName`	string	-	normally not necessary, name of the explicit triggered pulses

As said before, one of the peculiarities of `BBfit` is that it uses a simplified detector geometry consisting of a single OM situated at the centre of each floor, instead of the standard three OMs per floor. Moreover, the hit selection returns a maximum of one selected hit per floor. Nevertheless no custom classes have been created to store the selected hits, since this would have made it more difficult to use the hit selection in other contests than `BBfit`. The selected hits are thus stored in a `I3RecoPulseSeriesMap` class, which is the standard class used in `SeaTray` for storing hits. The selected hit at each floor, when present, is put in correspondence of the OM with id=0. The fitter will then internally place the hit at the centre of the floor (note that this comes naturally from the parametric formulae used to calculate the track quality in equation 3.9).

The module BBFit

This module performs the $\tilde{\chi}^2$-fits, giving as output the reconstructed track and bright point. Below it is shown how to include it in a `SeaTray` script:

```
tray.AddModule("BBFit","bbfit")(
   ("SelectedPulsesName", "BBFitSelectedPulses"),
   ("OutputTrackName","BBFitTrack"),
   ("OutputBrightName","BBFitBright"),
   ("PerformMirrorCorrection",True),
   ("EventPulsesName","RawHitsAfterL0")#needed if "PerformMirrorCorrection"=True
   ("WriteAllEvents",True)#defaulted to True
   )
```

This module has six configurable parameters, described in table 3.2. The name of the hit map to be used for the reconstruction must be specified at the `SelectedPulsesName` parameter. The module performs the track and bright point reconstruction and stores the results in two different `AntaresRecoParticle` objects. These are put in the frame with the names set for the `OutputTrackName` and `OutputBrightName` parameters respectively. If one of the two names is not set, the corresponding fit is not performed and the track object is not stored. The execution of the azimuth degeneracy correction is included in this module and is set with the Boolean flag `PerformMirrorCorrection`. Every time this is set to `True`, the user must provide also the name of the event hits with the parameter `EventPulsesName`. If the Boolean flag `WriteAllEvents` is set to `True`, the module will write also those events for which no reconstruction has been performed (for example if not enough hits were selected).

Table 3.2: *Configurable parameters for the module `BBFit`*

Parameter Name	type	default	description
`SelectedPulsesName`	string	-	name of the selected pulses for reconstruction
`OutputTrackName`	string	-	name of the reconstructed track in the frame
`OutputBrightName`	string	-	name of the reconstructed bright point in the frame
`PerformMirrorCorrection`	bool	True	apply or not mirror correction to multiline tracks
`EventPulsesName`	string	-	name of the event pulses needed for the mirror correction
`WriteAllEvents`	bool	True	pass or not those frames where no reconstruction has occurred

The module `BBFitMEstimator`

This module performs the MEstimator track fit, and can be included in a `Seatray` script using the following example:

```
tray.AddModule("BBFitMEstimator","bbfit-mest")(
   ("InputPulsesName","CalibratedPulses"),
   ("InputTrackName","BBFitMirrorTrack"),
   ("OutputTrackName","BBFitMEstTrack"),
   ("PulsesUsedForFitName","BBFitMEstRecoPulses"),
   ("WriteAllEvents",False)
   )
```

The parameter `InputPulsesName` requires the name of the event pulses in the frame, which are needed to perform the hit selection for the fit. This hit selection is done internally, but it is possible to access the results by setting a value to the parameter `PulsesUsedForFitName`, that will make the module push the relative pulses to the frame. The `PrefitTrackName` indicates the prefit track that initializes the M-Estimator minimization. Normally it is taken from the `BBFit` module, though it could be provided by any other external module. When reading the prefit tracks, the module checks the number of lines used for the reconstruction with the function `AntaresRecoParticle::GetNumberOfUsedLines()`, if this is less than 2 the reconstruction is not performed. The reconstructed track will be stored in the frame with the name set for the `OutputTrackName` parameter as an `AntaresRecoPArticle` shared-pointer object. A list of the configurable parameters for this module is shown in Table 3.3.

Table 3.3: *Configurable parameters for the module* `BBFitMEstimator`

Parameter Name	type	default	description
`InputPulsesName`	string	-	name of the event pulses
`PrefitTrackName`	string	-	name of the prefit track in the frame
`OutputTrackName`	string	-	name of the reconstructed track
`PulsesUsedForFitName`	string		name of the pulses that have been selected for reconstruction
`WriteAllEvents`	bool	True	pass or not those frames where no reconstruction has occurred

3.3.2 Conclusions

The `BBfit SeaTray` package presented here is currently included in all ANTARES Monte Carlo and data productions. It is used in the analyses for dark matter searches

due to its better performances at lower energies with respect to the maximum likelihood algorithm. The standalone algorithm is used for the online reconstruction of neutrino events and to send alerts to a network of optical telescopes for the optical followup around the reconstructed direction of particularly energetic neutrino events (Ageron et al., 2012). This `SeaTray` version can not be used for online processing of the data, due to the overhead introduced by the use of a framework which is not optimized for speed, though it is used as a cross check for the offline analyses. The hit selection module has been implemented in the analysis devoted to the search of electron showers induced by GRBs (Presani, 2011).

Even though this reconstruction strategy performs better at lower energies (few hundreds of GeV), the maximum likelihood algorithm has a higher efficiency to neutrino fluxes from point sources with an E_ν^{-2} spectrum up to 100 TeV and beyond. For this reason, the maximum likelihood algorithm will be used in the search for neutrino emission from microquasars presented in the following chapters.

Chapter 4

Microquasars

Microquasars are galactic binary systems formed by a compact object, i.e. a black hole or a neutron star, accreting mass from a companion star. The accretion flow of matter from the companion to the compact object causes X-ray emission through the dissipation of gravitational energy. Microquasars hence belong to the class of X-ray binaries (XRB), that have been extensively studied since the launch of the first X-ray space detectors. What characterizes them among other XRBs is the observation of relativistic ejections of matter, detected as non-thermal synchrotron radiation by ground based radio telescopes. These ejections, or jets, were first discovered on 1E1740.7-2942 (Mirabel et al., 1992) and successively observed with apparent superluminal motions on GRS 1915+105 (Mirabel et al., 1994), indicating that the acceleration of matter takes place up to relativistic velocities.

The name was chosen in analogy with AGNs, in which accretion and ejection were known to take place. The physics of mass accretion onto black holes and the subsequent acceleration of matter in the form of relativistic jets is assumed to be governed by the same laws in microquasars, AGNs and GRBs (Figure 4.1). The main differences derive from the fact that the scales of length and time of the phenomena are proportional to the mass of the black hole (Mirabel, 2004).

This chapter describes the main features of microquasars and presents an overview of the radiative processes that contribute to their broad band emission. Particular stress is given to the correlations between different wavelengths, as in disc-jet coupling. Most of what is presented here applies generally to XRBs.

4.1 Classification and main properties

Some physical and observational properties of XRBs depend on the nature of the companion star and of the compact object.

Depending on the mass M_c of the companion, such systems are classified as "high-mass X-ray binaries" (HMXBs), if $M_c \gtrsim 10M_\odot$, and "low-mass X-ray binaries" (LMXBs), if $M_c \lesssim 1M_\odot$, where $M_\odot$ denotes the solar mass. In HMXBs the orbiting companion is a massive OB class star and accretion is driven by its strong supersonic stellar wind. In LMXBs instead the companion can fill its Roche lobe and the mass is transferred through the Lagrangian point (see § 4.2). The companion star is usually directly observable in HMXBs systems, whereas in LMXBs

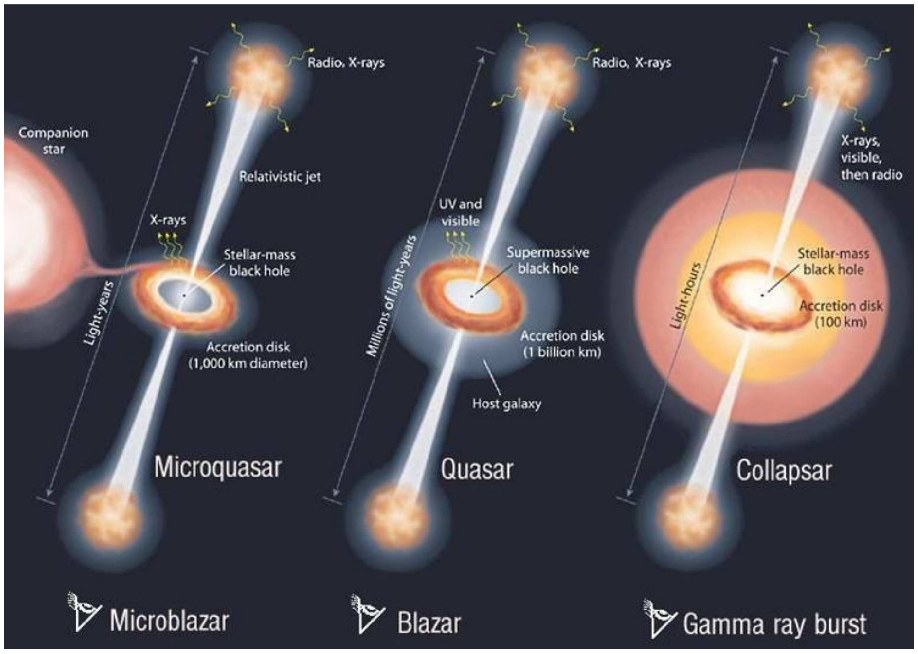

Figure 4.1: *The mechanisms driving the acceleration of relativistic jets are supposed to be governed by the same laws for microquasars (left), quasars (centre) and collapsars (right). Each of these objects contains a black hole, an accretion disk and relativistic jets. Whilst microquasars and quasars can eject matter recursively, collapsar jets form but once. When the jet is oriented towards the observer's line of sight these objects appear as microblazars, blazars and gamma ray bursts.*

the optical emission is dominated by reprocessed X-ray radiation from the disc and the irradiated face of the companion. Given the large difference in mass between high- and low-mass companion, they also evolve in different ways. The lifetime in HMXBs is determined by the lifetime of the massive star ($\sim 10^5 - 10^7$ yr), whereas in LMXBs it is determined by the mass transfer process and is longer ($\sim 10^7 - 10^9$ yr). As a consequence, HMXBs are distributed along the galactic plane as young stellar populations, while LMXBs are mostly found in the galactic centre and in globular clusters (Grimm et al., 2002).

Another classification can be done with respect to the nature of the compact object, either a black hole or a neutron star. The presence of a solid surface in neutron stars and an event horizon in black holes can lead to different observational properties. Matter accreted on the surface of a weakly magnetic neutron star may compress to densities for which the thermonuclear burning of helium is unstable. This causes the ignition of helium and an observed X-ray burst with a typical rise time of ~ 1 s and decay time of ~ 10 s, called Type I thermonuclear burst (for a review see Strohmayer et al., 2006). This is, together with the observation of a pulsed X-ray emission, an unambiguous signature of accretion on a neutron star. The measurement of a high mass for the compact object is considered one of the strongest pieces of evidence for the presence of a black hole, since an upper bound to the mass of any NS is $\sim 3.2 M_\odot$.

Lists of known low-mass and high-mass microquasars are shown in Table 4.1 and 4.2.

Table 4.1: *List of known low mass microquasars(Liu et al., 2007) and relative visibility for ANTARES. The visibility is defined as the fraction of time the source is below the horizon as seen by ANTARES.*

Name	RA (°)	Dec (°)	Visibility(%)
Circinus X-1	230.17	-57.17	100.0
XTE J1550-564	237.74	-56.48	100.0
GX 339-4	255.71	-48.79	100.0
GRO J1655-40	253.50	-39.85	78.1
H1743-322	266.56	-32.23	69.9
1E 1740.7-2947	265.98	-29.75	67.8
XTE J1748-288	267.02	-28.47	66.8
GRS 1758-258	270.30	-25.74	64.8
Scorpius X-1	244.98	-15.64	58.4
Swift J1753.5-0127	268.37	-1.45	50.9
GRS 1915+105	288.80	10.95	44.5
XTE J1859+226	284.67	22.66	37.3
XTE J1118+480	169.55	48.04	0.0

Table 4.2: *List of known high mass microquasars (Liu et al., 2006) and relative visibility for ANTARES. The visibility is defined as the fraction of time the source is below the horizon as seen by ANTARES.*

Name	RA (°)	Dec (°)	Visibility(%)
IGR J17091-3624	257.26	-36.39	73.9
V4641 Sgr	274.84	-25.43	64.6
LS 5039	276.56	-14.85	58.0
SS 433	287.96	4.98	47.6
Cygnus X-1	299.59	35.20	27.4
Cygnus X-3	308.11	40.95	20.4
CI Cam	64.93	56.00	0.0
LS I +61°303	40.13	61.23	0.0

4.2 Accretion process and X-ray emission

4.2.1 Mechanisms of mass transfer

Roche lobe overflow

When the gravitational attraction of the compact object is able to remove the outer layers of the companion star, mass transfer takes place through the Roche lobe overflow (after the French mathematician Edouard Roche, who first studied this problem in connection with planetary satellites). The potential to which a test particle of negligible mass is subject in the presence of two co-rotating bodies of masses M_1 and M_2, also called the Roche potential, includes the gravitational terms of the two masses plus a centrifugal term:

$$\Phi_R(\vec{r}) = -\frac{GM_1}{|\vec{r}-\vec{r}_1|} - \frac{GM_2}{|\vec{r}-\vec{r}_2|} - \frac{1}{2}(\vec{\omega}\times\vec{r})^2 \ , \tag{4.1}$$

where $\vec{r}_1$ and $\vec{r}_2$ are the positions of the two masses and $\vec{\omega}$ is the angular velocity of the rotation, which is given by Kepler's law $|\vec{\omega}| = [G(M_1+M_2)/a^3]$, a being the separation between the two objects. The shape of the potential Φ_R depends only on the ratio $q = M_2/M_1$ and is sketched in Figure 4.2. The first Lagrangian point L_1 connects the two Roche lobes and acts as the point of lowest potential, a saddle, between the two potential wells around the two masses. Material within one of the lobes in the vicinity of L_1 finds it favourable to pass through L_1 into the other lobe, thus allowing mass transfer.

Stellar winds

Stellar winds in early type OB massive stars can provide a mass loss rate sufficient to drive accretion in close binary systems with a compact object. Such intense winds are driven by the momentum transfer from photons to the ions in the plasma due to resonant scattering at absorption/emission lines, for which reason they are referred to as "line driven winds". Reviews can be found in Cassinelli; Puls et al. (1979;

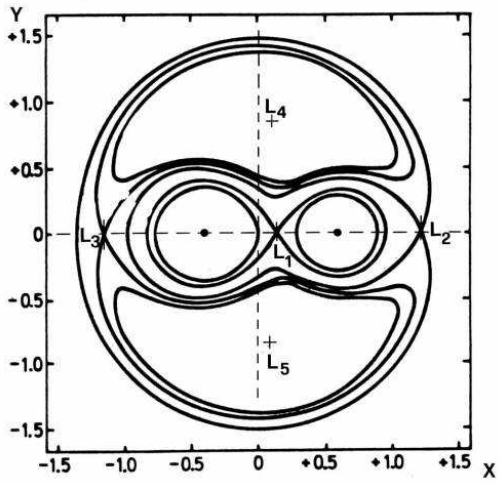

Figure 4.2: *Roche potential in the orbital plane of a binary system with $q = 0.3$. Black lines represent the intersection of equipotential surfaces with the x-y plane. The critical points $L_1, \ldots, L_5$ correspond to the condition $\nabla\Phi_R(\vec{r}) = 0$. The equipotential surface passing by the L_1 Lagrangian point defines the Roche lobes.*

2008). The momentum transfer after a resonant scattering is :

$$\Delta P = h/c(\nu_{in}\cos\theta_{in} - \nu_{out}\cos\theta_{out}) \ , \tag{4.2}$$

which, integrating all contributions, results in an overall radially directed acceleration thanks to the fore-aft symmetry of the re-emission process. This acceleration acts mainly to metal ions rather than H and He, the latter being accelerated less due to fewer lines close to the stellar flux maximum. In denser winds metal ions can transfer momentum to the passive hydrogen and helium ions through Coulomb collision. This is necessary for the line driven acceleration to act on the total wind plasma, given the higher abundance of H and He.

In the simple case of a stationary, homogeneus and spherical wind structure, the equation of motion, derived from the Navier-Stokes equation, reduces to:

$$v\frac{\mathrm{d}v}{\mathrm{d}r} = -\frac{1}{\rho}\frac{\mathrm{d}p}{\mathrm{d}r} - \frac{GM}{r^2} + g_{rad} \ , \tag{4.3}$$

where v is the radial velocity, ρ the mass density and p the pressure. The last two terms include the effects of external forces such as gravitation and radiation pressure respectively. The latter can be further decomposed in its two components, g_{rad}^{cont} due to the continuum opacity issued from photon scattering off electrons, and g_{rad}^{line} due to the opacity from line scattering.

Resonant scattering with a line of frequency ν_0 can also take place with a photon frequency $\nu > \nu_0$ by Doppler shift, provided that the velocity:

$$v = \frac{\nu - \nu_0}{\nu_0} \cdot c \ , \tag{4.4}$$

is reached by the accelerated plasma. If absorption lines are appropriately distributed, the flow of plasma can be optically thick to the whole spectrum and the entire momentum of the stellar radiation L/c be transferred to the wind with terminal velocity v_∞ and mass loss rate $\dot{M} \lesssim (L/c)/v_\infty$. For a star with $L = 10^6 L_\odot$ and $v_\infty = 3000 km/s$, this gives a maximum mass loss rate of $\dot{M}_{max} = 7 \times 10^{-6} M_\odot$ yr^{-1}, which is about what is observed for the most luminous Wolf-Rayet stars and OB supergiants.

Such intense winds can drive accretion on a compact object orbiting around the massive star with radial velocity v_c. The relative velocity between the wind and the compact object is $v_{rel} \approx (v_c^2 + v_\infty^2)^{\frac{1}{2}}$ and accretion can only take place within a cylindrical region along the relative wind direction and radius $r_{acc} \simeq 2GM_c/v_{rel}^2$. This accretion mechanism is nevertheless less efficient than the Roche lobe overflow in terms of the ratio between the star's mass loss rate and the accretion rate by the compact object, which is of the order of 10^{-4}-10^{-3}. Only the huge wind intensity in massive stars can make wind driven accretion have observable effects in X-ray binaries.

Clumpy winds Stellar wind modelizations are more complex and need to include the effects of rotation and of magnetic fields. Also the homogeneity hypothesis has revealed to be too simplistic and observational evidence shows that the winds of

massive stars may be in the form of clumps, i.e. blobs of expanding plasma. These clumps have typical sizes of $\sim 1R_\odot$, which would need a microarcsec resolution to be resolved at a distance of close O star ($\approx$ 1000 pc). Such small scale clumping was recognized with a time resolved and high resolution spectroscopic monitoring of WR emission lines (Moffat et al., 1988). The time evolution of the fine structure He II λ5411 line in HD 191745 (a Wolf-Rayet star) showed that those peaks that started red(blue)-shifted with respect to the central value of the line were becoming even more red(blue)-shifted with time, indicating the presence of blobs of wind material being accelerated outward.

4.2.2 Disc formation and radiation

Once the mass is transferred to the compact object, it cannot be accreted until it looses part of its angular momentum. An accretion disc is formed and the matter contained in each annulus follows a Keplerian orbit with angular velocity:

$$\omega_K(r) = \left(\frac{GM}{r^3}\right) , \tag{4.5}$$

where M is the mass of the attractor and r the radius of the orbit. This "differential rotation" can be exploited to introduce a mechanism for angular momentum transfer by means of a viscous torque acting between close rings rotating at different velocities. In the α-disc model by Sakura and Sunyaev (Shakura et al., 1973), the nature of the torque was identified with some turbulence of "unspecified" physical nature[1], whose effect is to make some particles fall inwards whilst others move outwards, thus conserving the total angular momentum and allowing accretion. Simple shear viscosity between the layers of the accreting plasma fails to provide the observed accretion rates. Balbus & Hawley (Balbus et al., 1991; Balbus et al., 1998) discovered a magnetohydrodynamical linear instability of discs accreting in presence of a weak magnetic field, which predicts the onset of turbulences in the accreting gas. The resulting viscosity coefficient seems to be of the right magnitude and sign in order to explain the observed accretion rates.

In an accretion disc that transports angular momentum through viscosity, the radiated energy can be inferred by imposing a steady accretion rate $\dot{m}$, without depending on the viscosity coefficient, leading to:

$$D(r) = \frac{3GM\dot{m}}{8\pi r^3}\left(1 - \sqrt{\frac{r}{r_0}}\right) , \tag{4.6}$$

where $D(r)$ is the irradiated energy per unit area per unit time, r is the radius of the emitting ring and r_0 the inner disc radius. If the disc is optically thick its radiation density is also described by the Stefan-Boltzmann law for blackbody radiation:

$$D(r) = \sigma_{SB}T^4(r) , \tag{4.7}$$

[1]Although the authors state that the mechanism could have a magnetohydrodynamical origin.

where σ_{SB} is the Stefan-Boltzmann constant and T the temperature. From Eq. 4.6 and 4.7 one can obtain the profile of the temperature along the disc:

$$T(r) = 2.7 \times 10^7 \mathrm{K} \left[\left(\frac{\dot{m}}{10^{-10} M_\odot \mathrm{yr}^{-1}} \right) \left(\frac{M}{M_\odot} \right)^{-2} \left(\frac{r}{R_g} \right)^{-3} \right]^{\frac{1}{4}} \cdot \left(1 - \sqrt{\frac{r}{r_0}} \right)^{\frac{1}{4}} , \quad (4.8)$$

where $R_g = GM/c^2$ is the gravitational radius. For values typical of X-ray binaries the disc temperature is $\sim 10^7$ K, corresponding to an X-ray thermal radiation. The disc composite spectrum from the contributions of all radii $r_{in} \leq r \leq r_{out}$ can be obtained by:

$$S(E) = \int_{r_{in}}^{r_{out}} B(E, T(r))\, 2\pi r \, \mathrm{d}r \ , \quad (4.9)$$

where $B(E, T(r)) \propto E^3 \cdot \exp[E/kT(r) - 1]^{-1}$ is the Planck function.

4.3 Other contributions to the X-ray spectrum

4.3.1 Comptonization

The spectrum of X-ray binaries cannot be explained only by blackbody emission from the accretion disc (cf. §4.5), since it often presents a non-thermal hard tail. This hard component is thought to be produced by multiple inverse Compton scattering of soft photons off high energy electrons. This process is referred to as Comptonization. The environment in which the high electrons are produced is still uncertain, the main hypotheses include an optically thin atmosphere of hot electrons surrounding the compact object, the so called *corona*, or a population of hot electrons at the base of an accelerated jet. In the first case the up-scattered photons would be the thermal ones produced in the disc, in the second case the synchrotron photons produced by the accelerated electrons in the jet.

The scattering of photons on electrons in the non-relativistic case is described by Compton scattering and the energy of the scattered photon is obtained by imposing the 4-momentum conservation:

$$E' = \frac{E}{1 + \frac{E}{m_e c^2}(1 - \cos\theta)} \ , \quad (4.10)$$

where $E' \leq E$, thus the photon can only loose energy when scattering off a stationary electron. In the approximation $E \ll m_e c^2$ the average relative energy loss is given by:

$$\left\langle \frac{\Delta E}{E} \right\rangle \approx -\frac{E}{m_e c^2} \, . \quad (4.11)$$

This is valid for the scattering off an electron at rest, but is not the situation that represents the environment in binary systems. In the presence of a population of electrons whose velocities are distributed as a Maxwellian (possibly relativistic) characterized by a temperature T_e, the scattering of photons with $E \ll kT_e$ is

referred to as *thermal Comptonization*. It can be shown (Rybicki et al., 1979) that in this case the average relative energy loss is:

$$\left\langle \frac{\Delta E}{E} \right\rangle \approx \frac{4kT_e - E}{m_e c^2} \ , \tag{4.12}$$

which is positive, i.e. the photon increases its energy, if $E < 4kT_e$. The photon spectrum resulting from the multiple scatterings within the electron plasma cloud, though not trivial to obtain (see e.g. Sunyaev et al., 1980), is roughly an exponential spectrum whose spectral index depends on the optical thickness of the plasma, with an exponential cutoff at $E \gtrsim kT_e$, at which energy photon up-scattering becomes less probable.

4.3.2 Reflection

The hard photons produced by Comptonization can successively interact with the "cold" matter in the accretion disc and be reprocessed, giving rise to the so called *reflected* component. If the photon energy is low enough, $\lesssim$ 15keV, it can excite the outer accessible shells of the ions in the plasma that will further reemit a fluorescence radiation. This produces the observed Fe Kα line at 6.4 keV, which is usually the most prominent among the fluorescence lines. Higher energy photons instead are Compton *down-scattered* and loose energy, thus producing a hump in the X-ray spectrum above $\sim$ 15 keV, so called "Compton reflection hump". Compton down-scattered photon can also be absorbed and contribute to the fluorescent emission.

4.4 Relativistic jets

Jets from microquasars have been imaged with radio observations from ground based very large baseline interferometry, via their non thermal synchrotron emission. From the measurement of their proper motions it has been inferred that they travel at relativistic velocities. In this section their main features are described.

4.4.1 Synchrotron emission

The observed radio emission from the jets is due to the synchrotron radiation produced by the relativistic electrons gyrating in the ambient magnetic field, as inferred from the observed spectral shape and degree of polarization.

A relativistic electron in a magnetic field has a gyrofrequency:

$$\omega_g = eB/\gamma m_e \ , \tag{4.13}$$

where B is the field strength and γ is the Lorentz factor of the electron. The trajectory being a helix, it forms a constant angle α with the magnetic field lines, called the pitch angle. The emitted radiation is strongly collimated in the direction of motion of the electron within a cone of half angle $1/\gamma$. An observer at rest sees a very short pulse every time the emission cone encounters its line of sight.

Such a narrow pulse produces a broad band spectrum, thus synchrotron radiation is naturally broad band. This emission is peaked at the so called *critical frequency*:

$$\omega_c = \frac{3}{2}\left(\frac{c}{v}\right)\gamma^3\omega_g \sin\alpha \ , \tag{4.14}$$

where v is the speed of the electron and α is the pitch angle. The total synchrotron emissivity for a single electron is given by (Longair, 1992):

$$j(\omega) = \frac{\sqrt{3}e^3 B \sin\alpha}{8\pi^2\varepsilon_0 c m_e} F(\frac{\omega}{\omega_c}) \ , \tag{4.15}$$

where ω is the emitted frequency and $F(\omega/\omega_c)$ is given by:

$$F(x) = x\int_x^\infty K_{5/3}(z)\,\mathrm{d}z \ , \tag{4.16}$$

where $K_{5/3}$ is the modified Bessel function of order 5/3. It can be shown that in the limit $\omega \gg \omega_c$ the emissivity in Eq. 4.15 has the form $j(\omega) \propto \omega^{1/2}\exp(-\omega/\omega_c)$, thus very little power is emitted at frequencies $\omega > \omega_c$.

The emission from relativistic jets is due to a population of relativistic electrons accelerated with a power law spectrum:

$$\frac{\mathrm{d}N}{\mathrm{d}E} \propto E^{-p} \ , \tag{4.17}$$

with each electron contributing to the total emissivity through the Eq. 4.15, where the energy E modifies the critical frequency ω_c in Eq. 4.14 (through the Lorentz factor). By integrating all the contributions to the emissivity at each energy and pitch angle, one obtains (Longair, 1992) that the key dependencies for the overall synchrotron emissivity are:

$$J(\omega) \propto B^{(p+1)/2}\omega^{-(p-1)/2} \ , \tag{4.18}$$

thus the spectral index of the accelerated electrons p is related to the spectral index of the observed radiation α as:

$$p = 1 - 2\alpha \, . \tag{4.19}$$

Observed optically thin spectral indices in the range $-0.4 \leq \alpha \leq -0.8$ indicate $1.8 \leq p \leq 2.6$, which is consistent with the value obtained from the shock acceleration mechanism (§1.1.4).

4.4.2 Jet speeds and apparent superluminal motions

Jet speeds from AGNs and microquasars are estimated by measuring the proper motion of the ejected blobs using very long baseline interferometry. For a twin jet emitted at an angle θ from the line of sight, the proper motions $\mu_{a,r}$ of the approaching and receding components are:

$$\mu_a = \frac{\beta\sin\theta}{(1-\beta\cos\theta)}\frac{c}{d} \quad , \quad \mu_r = \frac{\beta\sin\theta}{(1+\beta\cos\theta)}\frac{c}{d} \ , \tag{4.20}$$

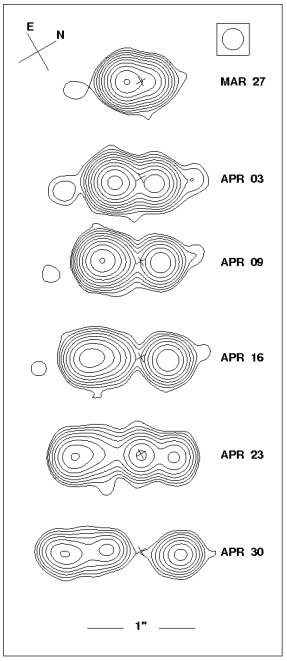

Figure 4.3: *Radio maps of GRS 1915+105 taken at different epochs of 1994 (shown on the right side) with VLA at 3.5 cm (from Mirabel et al., 1994). Supposing a distance of 12.5 kpc, the extrapolated apparent motion of the approaching blob is superluminal.*

where d is the distance from the source and β the intrinsic speed of the jets. The two equations 4.20 can be transformed to the equivalent pair of equations:

$$\beta \cos\theta = \frac{\mu_a - \mu_r}{\mu_a + \mu_r} \ , \tag{4.21}$$

$$d = \frac{c \tan\theta}{2} \left(\frac{\mu_a - \mu_r}{\mu_a \mu_r} \right) \ , \tag{4.22}$$

where the product $\beta \cos\theta$ is known without knowing the distance. By setting $\beta = 1$ in Eq. 4.21 and substituting the θ obtained in Eq. 4.22, one can obtain an upper limit to the distance:

$$d_{max} = \frac{c}{\sqrt{\mu_a \mu_r}} \ , \tag{4.23}$$

whereas an independent measure of the distance allows the calculation of both jet parameters β and θ.

Apparent superluminal motions, i.e. when the observed jet speed $\beta_{obs} = \mu d > 1$, were first predicted by (Rees, 1966) and successively observed on AGNs (Porcas, 1987). The first galactic superluminal source to be discovered was GRS 1915+105 (Mirabel et al., 1994), for which a proper motion of the approaching jet $\mu_a = 17.6 \pm 0.4$ milli arcoseconds d^{-1} was measured, corresponding to $\beta_{obs} = 1.25 \pm 0.15$, for a distance of 12.5 ± 1.5 kpc independently measured. The resulting intrinsic jet speed for this source is $\beta = 0.92$, thus the jet is relativistic (Figure 4.3).

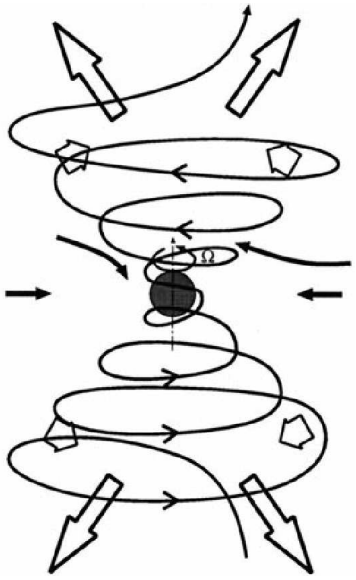

Figure 4.4: *Scheme of the MHD acceleration and collimation mechanism. The magnetized plasma inflow towards the compact object (solid arrows) winds the magnetic field lines into a rotating helical coil. Magnetocentrifugal forces expel some of the material along the field lines and magnetic pressure and pinching forces (short open arrows) further lift and collimate it into a jet outflow (long open arrows)*

4.4.3 Jet acceleration and collimation

The most credited mechanism for explaining the observed relativistic and collimated jets from accreting objects involves magnetohydrodynamics (MHD). In (Meier et al., 2001) a model is presented in which the differential rotation of the accreting plasma creates a magnetic coil that expels some of the in-falling material. In this model only two simplifying assumptions are made: that plasma particles act like a fluid and that the conductivity is so high that electric fields generated by free charges are shorted out. Under these conditions, of ideal magnetohydrodynamics, the field lines are tied to the plasma (frozen in). As a result, the field lines generated in this way have three important properties:

- the plasma flows along the field lines and cannot cross them. If the hydrodynamic pressure is higher than the magnetic pressure, magnetic field lines are bent in spiral by the rotating plasma.

- parallel field lines repel each other, producing a pressure perpendicular to them and thus to the flow of plasma. This magnetic pressure can be enhanced by the addition of more field lines, due for example to a toroidal coiling.

- magnetic field lines tend to straighten like spring wires if left alone, whereas they keep a curved shape only if forced by an external pressure from the plasma or from other magnetic field lines.

The magnetized plasma accreting to the central compact object through an accretion disk with differential rotation is threaded by the poloidal magnetic field lines that assume a helix shape about the rotation axis (long solid line in Figure 4.4). Depending on the relative importance of the magnetic field, plasma density and rotation the system can evolve in different ways, such as a broad uncollimated wind, a slowly collimated bipolar outflow and a highly collimated jet.

4.4.4 Jet composition

The composition of microquasar jets, and in particular their baryonic content, is a key point for neutrino flux expectations. At present, only the synchrotron emission from the leptonic component of the jets, both from microquasars and AGNs, has been observed. The only exception is the microquasar SS 433, for which a series of ionization iron lines have been recognized in the X-ray spectrum of the jets (Marshall et al., 2002).

The reason why emission lines are only observed in SS 433 is yet unclear. One possible interpretation is that all other jets have little or no baryonic content and are purely composed by e^-e^+ pairs. This would mean that the majority of the accreted mass does not escape from the system. Indeed, the jets from SS 433 are only mildly relativistic with $\beta = 0.27$, which may facilitate the observation of the emission lines. Mirabel et al. (1997) observed that the absence of emission lines from GRS 1915+105 jets may be due to a strong Doppler broadening caused by the intrinsic relativistic expansion of the blobs at $\geq 0.1c$ ($\Delta\lambda/\lambda \geq 0.1$). Moreover, R. P. Fender (2003) showed that Doppler factors of microquasar jets are poorly constrained, thus it is not know where to look for such lines.

4.5 X-ray spectral states and disc-jet coupling

The main contributions to the X-ray spectrum of XRBs have been unidentified in § 4.2 and § 4.3, these are:

1. the thermal blackbody component from the accretion disc, at soft X-ray energies,

2. the radiation produced by the Compton up-scattering of soft photons in a gas of hot electrons, in form of a power-law component up to hard X-ray energies (with possible cutoff),

3. the reflected radiation from the disc, at energies $\gtrsim 10$ keV, and the iron emission lines, at 6.4 keV.

This emission is also variable in time in terms of flux, spectral shape and timing properties. Studies made in the last decades with X-ray telescopes on X-ray binaries have shown that the variability of the X-ray flux for these objects follows some specific patterns that have been classified in so called *X-ray states*, each presumably representing a different mode in the accretion of matter onto the compact object (Esin et al., 1998). X-ray states can also be correlated to the acceleration of a jet or its suppression. In the next sections, the state classifications for black hole and neutron star binaries are presented.

4.5.1 In black hole binaries

X-ray states in black hole binaries (BHBs) have been classified according to the component that dominates the spectrum:

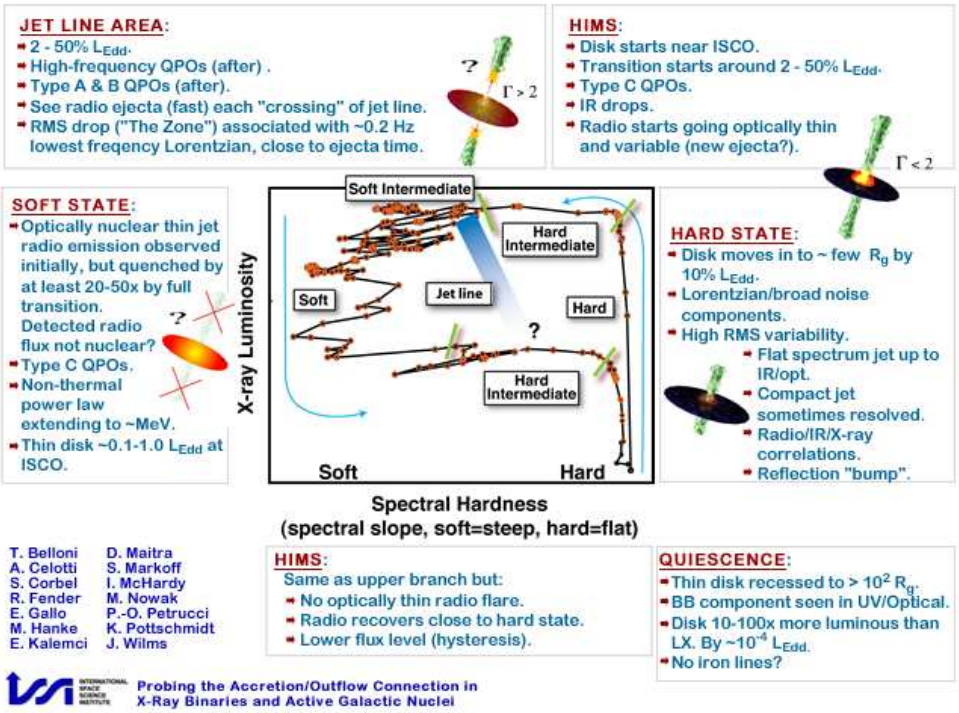

Figure 4.5: *Sketch of the "canonical q-track pattern" through all the different spectral states of a black hole binary outburst. Figure from: http://www.sternwarte.uni-erlangen.de/proaccretion/.*

- *hard state* (also called Low/Hard State, LHS): the source is fainter and the spectrum is non-thermal and well fitted by a power law function with spectral index ∼1.7, while the thermal component is weaker and at lower energies than in the soft state.

- *hard intermediate state* (HIMS): softer spectrum than the hard state, with evidence of the thermal disk component

- *soft intermediate state* (SIMS): the spectrum is systematically softer that the HIMS and the disk component dominates the spectrum

- *soft state* (also called High-Soft State or Thermal Dominant): the source is bright in X-rays and the spectrum is well fitted by a multi-temperature accretion disc model with a temperature of ∼1 keV.

The HIMS and the SIMS[2] are metastable, transitional states that present features common to both the hard and the soft states, with a steep power law component (photon index >2.4) as well as a thermal contribution.

Since the X-ray and radio emission of a binary system are linked to the accretion and the ejection of matter respectively, correlations between these two wave bands have been looked for in XRBs. A long term monitoring study conducted on GX 339-4 (Corbel, R. P. Fender, et al., 2000) has shown that during the hard state the

[2]For an alternative classification scheme see (McClintock and Remillard, 2006).

source accelerates a steady jet and that the X-ray and radio fluxes are correlated. Further studies have proved that this scheme is applicable to several black hole candidates (BHC) and that during the hard state the intensities of the radio and X-ray flux seem to fit the relation $L_{radio} \propto L_X^{+0.7}$ (Gallo, R. P. Fender, et al., 2003). An empirical study on a large sample of outbursts from binaries (R. P. Fender et al., 2009) has attempted to give a unified model to the disk jet coupling in black hole binaries. Outbursts from black hole binaries start and end in the hard state at a low luminosity, developing in a characteristic Q-shaped track in the Hardness Intensity Diagram (HID), as shown in Figure 4.5. During the first phase the source increases its luminosity keeping a hard spectrum until it undergoes a transition to the intermediate states. The HIMS and the SIMS can be distinguished by their timing properties as well as by the ejection of relativistic jets associated to the transition from the HIMS to the SIMS. After the SIMS, the source enters a state where the X-ray spectrum is dominated by the emission of the soft thermal component, the soft state. Then the flux starts to decrease, most likely following a parallel decrease in accretion rate. At some point, a reverse transition is started and the path is followed backwards, though at a lower luminosity, all the way to the hard state and then to quiescence. The resulting correlation between the X-ray state and the radio emission during the evolution of an outburst can be summarized as follows:

- a powerful steady jet with $\Gamma \sim 2$ is present during the hard state
- a major radio flare with $\Gamma > 2$ is produced during transitions from the HIMS to the SIMS
- the core jet is suppressed during the soft state, but a relic emission is observed probably due to the expanding blobs.

4.5.2 In neutron star binaries

Low magnetic field neutron star X-ray binaries are divided into two broad subclasses according to their timing and spectral properties: "Z" sources and "atoll" type neutron stars. The names are related to the shape assumed by their X-ray colour-colour diagrams (CD), an example of which is shown in Figure 4.6.

Z sources, first classified by (Hasinger et al., 1989), are supposed to accrete at near the Eddington rate and are the most luminous NSs in our Galaxy. The three branches forming the typical Z-shaped track of their CD are called Horizontal (HB), Normal (NB) and Flaring (FB), and define three distinct spectral states of the systems. Z sources are rapidly variable in X-rays and can transit through the three states in hours to days. The radio emission depends on the position in the CD and is observed to decrease at increasing mass accretion rates (solid line in Figure 4.6). The only two known neutron microquasars are Sco X-1 and Cir X-1. The former is classified as a Z source, whereas the latter is considered as a peculiar source that avoids classification. The radio emission of Cir X-1 is dominated by its orbital period of 16.6 days, with an enhanced radio jet at superior conjunction.

Atoll sources show two distinct X-ray states, hard and soft, which are recognized according to the position in the CD: the hardest X-ray state is called "island", the

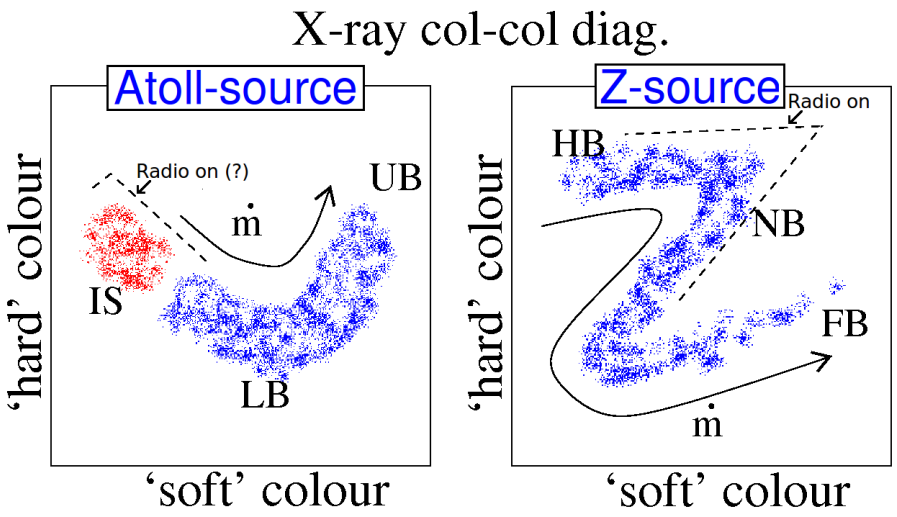

Figure 4.6: *Example of colour-colour diagram of an atoll-type and Z-type neutron star binary, from (R. Fender, 2002). For the atoll sources the abbreviations are: IS=Island State; LB=Lower Banana; UB=Upper Banana. For the Z sources the abbreviations are: HB=Horizontal Branch; NB=Normal Branch; FB=Flaring Branch.*

softest "banana". Atoll sources are fainter in radio than Z sources, probably due to their lower accretion rate.

4.6 HE and VHE γ-ray emission from microquasars

A few microquasars, all classified as HMXBs, have also been detected in γ-rays at high (HE, 0.1-100 GeV) and/or very high (VHE, >100 GeV) energies.

The peculiar microquasars LS 5039 and LS I +61°303 were first detected in VHE γ-rays by H.E.S.S. (Aharonian et al., 2005) and MAGIC (Albert et al., 2006) respectively, and successively by Fermi-LAT (Abdo et al., 2009b; Abdo et al., 2009c). Both sources are considered enigmatic as their γ-ray spectra resemble those of pulsar wind nebulas, although no pulsation at GeV energies has ever been observed.

Cyg X-1 was detected by MAGIC in 2006 (Albert et al., 2007b) and by AGILE in 2009 (Sabatini et al., 2010). In both cases the detection was only significant when restricting the analysis to a 1-day period.

Cyg X-3 has recently been detected flaring in the gamma rays by AGILE (Tavani et al., 2009) and then by Fermi-LAT (Abdo et al., 2009d), who also detected its orbital period. The observed HE γ-ray outbursts were in both cases coincident with an ultra soft X-ray state, known to be associated to major radio outbursts for this source. Emission above 250 GeV has been excluded by MAGIC up to a flux 2.2×10^{-12} ph cm^{-2} s^{-1} (Aleksić et al., 2010).

A search for γ-ray emission from other microquasars has been performed with negative results. Sco X-1 has been observed for several hours by MAGIC while it was in the Normal and Flaring Branch (i.e. when the relativistic jet emission is expected, cf. § 4.5.2), giving an upper limit of 3.4×10^{-12} cm^{-2}s^{-1}. The microquasars GRS 1915+105 and SS 433 were also undetected by MAGIC (Saito et al., 2009).

A leptonic model to explain the broad band γ-ray emission from microquasars is presented in (Bosch-Ramon, Romero, et al., 2006). The high and very high energy emission is explained by means of inverse Compton scattering with the relativistic electrons in the jet, seeded by the synchrotron photons from the jet itself (Synchrotron Self Compton, SSC) as well as by the external photon fields from the companion star, from the disc and the corona. This model has been applied to the case of LS 5039 (Bosch-Ramon, Paredes, et al., 2006) and allows the explanation of the broad band spectral energy distribution, although underestimating by one order of magnitude the contribution in the VHE regime with respect to the H.E.S.S. measurement. A hadronic model for the production of high energy gamma rays in HMXBs and its implications in the neutrino flux are presented in § 4.7.2

4.7 Models for neutrino production

4.7.1 Neutrinos from the jets

A model that allows the estimation of the flux of neutrinos to be expected from microquasar jets is presented in (Levinson et al., 2001). It assumes that the energy employed in the jet acceleration is significantly dissipated through collisionless internal shocks at sufficiently small scales, estimated to be $\lesssim 10^{11}$ cm. This mechanism accelerates a population of protons to a non-thermal energy distribution $\mathrm{d}N/\,\mathrm{d}E \propto E^{-2}$ up to high energies ($\sim 10^{16}$ eV). The fraction of jet energy that is tapped to accelerate the protons, denoted by η_p, is given by the fraction of the total burst energy that is dissipated behind the shock, times the acceleration efficiency at which protons are accelerated by a single shock. These protons can then interact with the X-rays produced in the accretion disk or with the synchrotron photons produced inside the jet by thermal electrons. If the proton energy is higher than the threshold for the production of the Δ-resonance, estimated around $10^{13} - 10^{14}$ eV, neutrinos can be produced by the subsequent pion production and decay. Since the neutrino produced is expected to carry $\sim$5% of the initial proton energy, TeV neutrinos are expected from this model. The total energy flux in neutrinos (ν_μ and $\bar{\nu}_\mu$) at Earth is given by (Levinson et al., 2001, Eq. 18):

$$f_{\nu_\mu} \simeq \frac{1}{2}\eta_p \Gamma^{-1} \delta^3 \frac{L_j/8}{4\pi D^2} \ , \tag{4.24}$$

where Γ is the bulk Lorentz factor of the jet, $\delta = [\Gamma(1 - \beta\cos\theta)]$ its Doppler factor (θ the angle between the jet and the line of sight), L_j the jet luminosity and D the distance of the source. The procedure for the calculation of L_j depends on whether the radio emitting knots are resolved or not and is detailed in Distefano et al. (2002).

4.7.2 Neutrinos from wind-jet interactions in HMXBs

Romero et al. (2003) presents a hadronic model for the production of γ-rays and neutrinos from microquasars with a high mass star ($\sim 10 M_\odot$) anchored to the compact object. Early type OB stars are able to loose a significant fraction of their mass through an intense stellar wind which can drive accretion (see § 4.2).

Typical mass loss rates are of the order of $10^{-5} M_{\odot}$ yr^{-1} with winds at speeds of ~ 2500 km s^{-1}. Neutrinos can be produced by the interaction of the relativistic hadrons accelerated in the jets with the clumps of stellar wind from the companion star.

Chapter 5

Multi-wavelength study

In searches for point sources of neutrinos, the atmospheric neutrino background can be significantly reduced if proper time cuts are applied in addition to the simple directional information. This is the case e.g. for transient sources such as GRBs and can be generally applied to all variable sources, as AGNs and microquasars for instance. The advantage is that a single neutrino detected in time coincidence with a sufficiently short transient event and coming from the same direction (within the angular resolution of the detector) can easily reach a high statistical significance.

Microquasars are variable sources in which long periods of quiescence, lasting up to years or decades, can be followed by luminous outbursts, lasting up to several months. Persistent X-ray microquasars, such as Cyg X-1, can pass through different X-ray states, each in turn related to a certain radio behaviour. The presence of relativistic jets, witnessed by the radio emission, is naturally interesting in a contest of cosmic ray acceleration and neutrino production. Radio telescopes, however, usually do not continuously monitor sources and radio observations are only confined to particular periods. This limitation can be overcome by the last generation of X-ray satellites, equipped with monitoring detectors. As they provide continuous information on the flux of known sources, they are used to trigger observations from other telescopes, including radio, infrared and X-ray pointed observations. Moreover, for certain black hole binaries, they can be employed to estimate the radio behaviour by means of established relations between accretion and jet acceleration, as described in § 4.5.1.

This chapter focuses on the methodology used to select a list of candidate microquasars and, for each microquasar, the choice of the interesting periods in which to look for neutrinos. The main input comes from the light curves of the two X-ray monitors RXTE/ASM and Swift/BAT, coupled with more detailed X-ray analyses found in the literature or in the *Astronomers Telegram*[1] (ATel). In one case, the γ-ray data from Fermi/LAT are used to select the outbursts. These data are used to look for outbursts that indicate the presence of the radio jet. The period in consideration for this analysis spans from the beginning of 2007 till the end of 2010, as for the ANTARES data set that will be further analyzed in § 6. Firstly, the detectors used in this study will be briefly described, and then the criteria used to select a list of candidate sources and the time selection are presented.

[1] http://www.astronomerstelegram.org

5.1 Detectors used

5.1.1 Rossi X-ray Tming Explorer - All Sky Monitor

The Rossi X-ray Timing Explorer (RXTE) satellite has been in orbit since 1995 December 30, and since then it has increased our knowledge about accreting systems in the galaxy. It is equipped with three instruments: the All Sky Monitor (ASM) (1.5-12 keV), the Proportional Counter Array (PCA) (2-60 keV) and the High Energy X-ray Timing Experiment (HEXTE) (15-250 keV).

The ASM (Levine et al., 1996) is equipped with three scanning shadow cameras each containing a position sensitive proportional counter able to infer the position and intensity of the sources within the wide field-of-view (FOV) of 6° by 90° FWHM. The cameras monitor 80% of the sky every 90 minutes (a dwell) and are sensitive to X-rays in the range of approximately 1.5-12 keV for three energy bands: a: (1.5-3 keV), b: (3-5 keV) and c: (5-12 keV). The light curves have been retrieved in form of ASCII tables as quick-look results provided by the RXTE/ASM team[2], which provide also the estimated uncertainty for each band. The subdivision in three bands enables calculation of the so called *Hardness Ratios* (HR), defined as the ratio between the fluxes of a harder over a softer band. In the literature, two HRs are defined and widely used:

$$HR_1 = \frac{c}{a} \ , \tag{5.1}$$

$$HR_2 = \frac{c}{b} \ . \tag{5.2}$$

5.1.2 Swift - Burst Alert Telescope

The Swift satellite (Gehrels et al., 2004) is operational since 2004 and it is dedicated to the study of GRBs in a multi wavelength contest. It is equipped with three instruments: the Burst Alert Telescope (BAT) (15-150 keV), the X-Ray Telescope (XRT) (0.2-10 keV) and the UV/Optical Telescope (UVOT) (170-600 nm). It is able to perform dedicated X-ray and UV/Optical observations, as well as to survey the entire sky.

The BAT instrument is a coded mask detector operating with good sensitivity in the energy range 15-150 keV over a field of view of 1.4 sr and with a point source location accuracy of $1'$-$4'$. It also performs a survey of the X-ray sky, providing orbital and daily averaged light curves of many microquasars, among other sources. The analysis in this thesis uses the processed light curves available from the BAT transient web page[3], for the energy range 15-50 keV.

5.1.3 Fermi - Large Area Telescope

The Fermi telescope was launched in 2008 to a low-Earth orbit at 565 km altitude. It studies the high energy phenomena in the Cosmos with its two instruments: the

[2]http://xte.mit.edu/asmlc/
[3]http://heasarc.nasa.gov/docs/swift/results/transients/

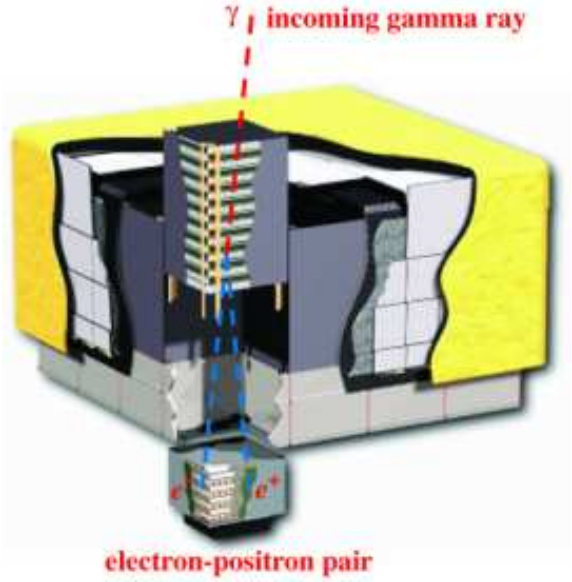

Figure 5.1: *Cutaway view of the LAT detector onboard the Fermi γ-ray telescope. In evidence one of the 16 modular detection towers with the tracking detector (top) and the calorimeter (bottom). The anti-coincidence detector surrounds the modules and lays below a multilayer "blanket" which provides thermal insulation and protects against micrometeoroids and debris (yellow).*

Large Area Telescope (LAT) (30 MeV - 300 GeV) and the Gamma-ray Burst Monitor (GBM) (8 keV - 30 MeV).

The LAT is sensitive to γ-rays with energies from 30 MeV to 300 GeV. The detector is composed of a tracking system, a calorimeter and an anti-coincidence detector. Both the tracking and calorimetry systems are made of 16 modules. The detection is based on the pair conversion of the incident γ-ray by means of high-Z material (tungsten) contained within the tracker. Here, solid-state silicon detectors follow the trajectory of the resulting e^+e^- pair to obtain the direction of the incident γ. The cesium-iodide calorimeter then measures the energy deposition produced by the pair. Another purpose of the calorimeter is to image the shower profile, thus helping to discriminate the background and to estimate the energy leakage fluctuations. The towers of the tracking and calorimetry system are surrounded by an anti-coincidence detector sensitive to charged particles, used to discriminate the the high flux of cosmic rays which is 10^5 times larger than the γ-ray flux. The LAT operates in continuous sky survey mode, covering the entire sky every 3 hours and has a large field of view of 2.4 sr. The point spread function has a width of 5° at 100 MeV, 0.8° at 1 GeV.

Data from Fermi/LAT have been employed to study the microquasar Cyg X-3.

5.2 Outburst selection using X-rays

The selection of the candidate microquasars is based on both the presence of X-ray outbursts and the possibility to relate them to the radio counterpart. Although some similarities can be found between different sources, the correlation patterns between X-ray and radio depend on the particular source under study, which makes it hard to find a single and generally applicable strategy to select active states for all microquasars. A first step can be done in the reverse direction, since it is easy to discard all those sources for which the X-ray light curves do not present any feature. This has been done by considering all the X-ray light curves for the period between 2007 and 2010 of all the microquasar visible by ANTARES and monitored by ASM and/or BAT (cf. the lists in Table 4.1 and 4.2). All the light curves are shown in Figure 5.3.

In order to establish the presence (or absence) of X-ray outbursts, the following procedure has been used:

- a Gaussian fit is performed to the distribution of the X-ray rates of both detectors to calculate the mean rate, or *baseline*, and its standard deviation $\sigma_{baseline}$
- the fit is performed within the interval $baseline^{+\sigma}_{-2\sigma}$, to reduce the contribution from the bursting region, and is repeated twice, iteratively updating the fit interval with the results of the previous fit
- the light curve is then scanned, looking for a rate measurement, a seed, that satisfies the condition $rate - 3\sigma_{rate} > baseline + 3\sigma_{baseline}$
- once a seed is found, all the following and preceding measurements for which $rate - \sigma_{rate} > baseline + 3\sigma_{baseline}$ are selected
- it is required that at least two consecutive measurements are selected, i.e. the *seed* plus an adjacent one, for the source to be considered in the analysis. Since daily averaged light curves are used, the minimum interval is two days.

In this way, all the sources that do not show any bursting activity are discarded. This was the case of, among others, SS 433, whose light curves are shown in Figure 5.2. In the case of Scorpius X-1 and GRS 1915+105 the ASM and BAT light curves are not sufficient to relate the X-ray activity to the jet acceleration, so these sources are also discarded, while Cygnus X-3 outbursts will be selected using γ-rays (section 5.3). The candidate sources selected with X-rays are: Circinus X-1, GX 339-4, H1743-322, IGR J17091-3624 and Cygnus X-1. With the exception of Cir X-1, which is a neutron star binary, they all are BHBs.

The selection of hard X-ray states in the BHB sources is done by looking for outbursts in the BAT light curve. Even though a rigorous estimate of the X-ray state should be obtained on the basis of the energy spectrum of the X-ray emission, from which one can calculate the contributions of the disk and the power-law components, the selection obtained with this criterion is in agreement with other observations in literature or in ATel, and it is thus considered suitable for selecting hard states. For

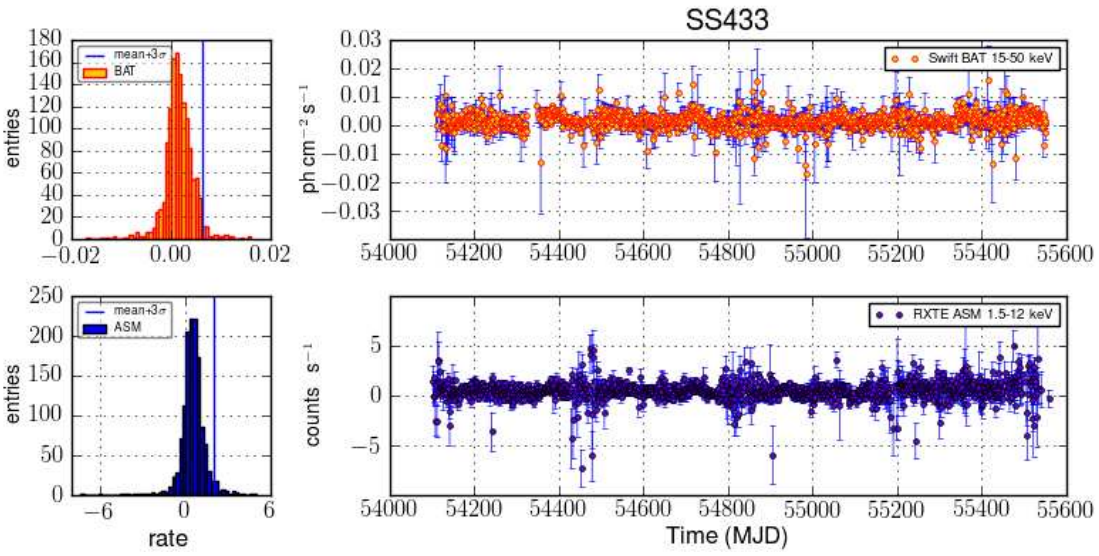

Figure 5.2: *The right plots represent the daily averaged X-ray light curves of the microquasar SS433 taken from Swift BAT (first row) and RXTE ASM (second row). The left plots represent the histogram of the X-ray rate compared with the value for the* $\text{mean} + 3\sigma$ *(vertical blue line) obtained from a Gaussian fit (see text). This source does not show any outbursting activity, so it is not selected for the analysis.*

the BHB Cygnus X-1, instead, a specific selection based on the ASM data will be adopted.

As discussed in section 4.5.1 the compact jet during the hard state is not the only interesting scenario for the neutrino search, another being the discrete emission at a higher Lorentz factor observed during the hard to soft transitions. When possible, the two scenarios will be treated separately, leading, for the BHBs, to two separate searches: one during the hard state and one during a state transition. It is worth pointing out for clarity that this scheme is not applied to Circinus X-1, which is a neutron star binary, or to Cygnus X-3, for which outbursts will be selected using γ-rays. Moreover, no transitions have been found for IGR J17091-3624.

In the following sections the detailed study for each of the selected sources is presented, the final results for the selected time windows are shown in Table 5.3.

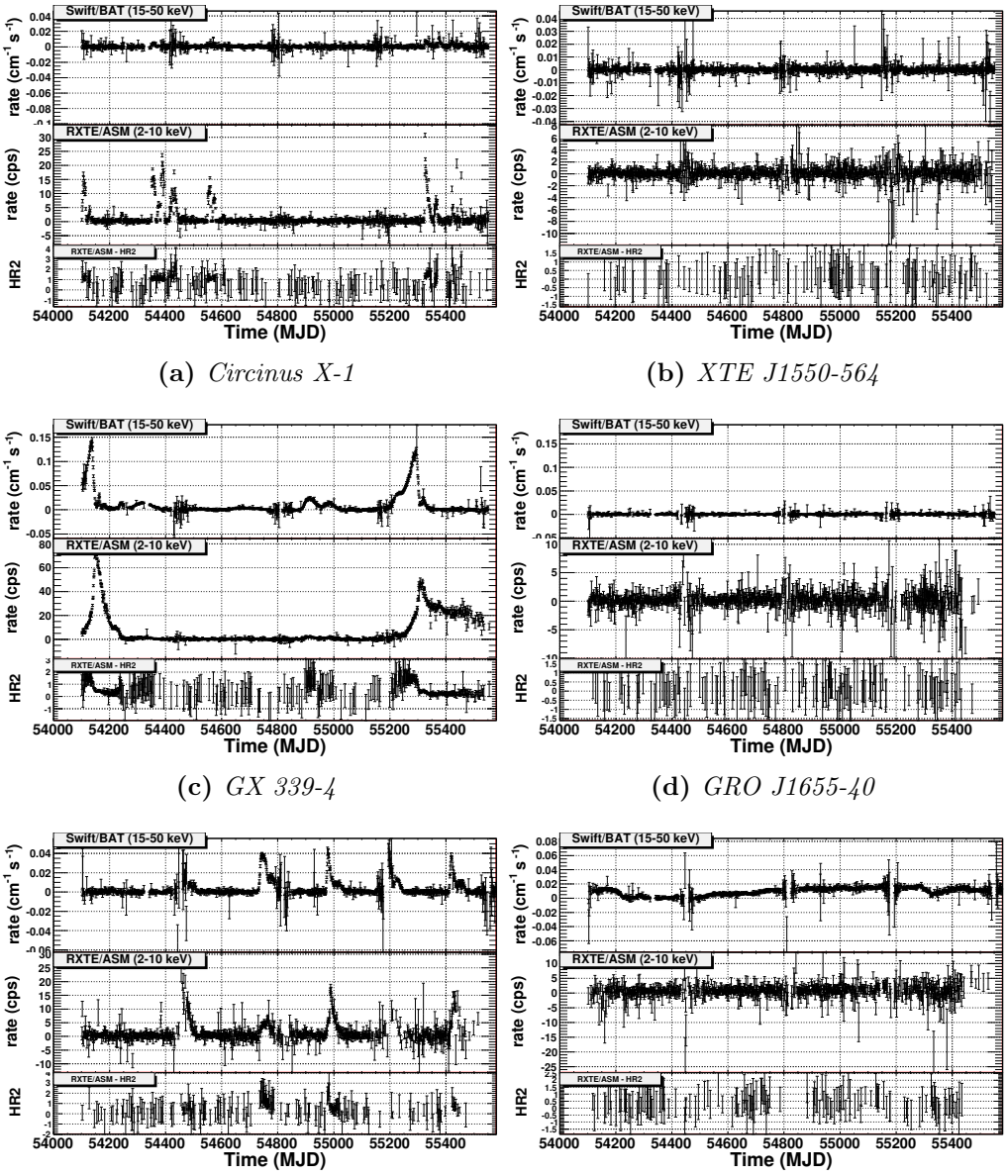

(a) *Circinus X-1*

(b) *XTE J1550-564*

(c) *GX 339-4*

(d) *GRO J1655-40*

(e) *H1743-322*

(f) *1E 1740.7-2947*

Figure 5.3: *Daily averaged X-ray light curves of the sources under study in 2007-2010.*

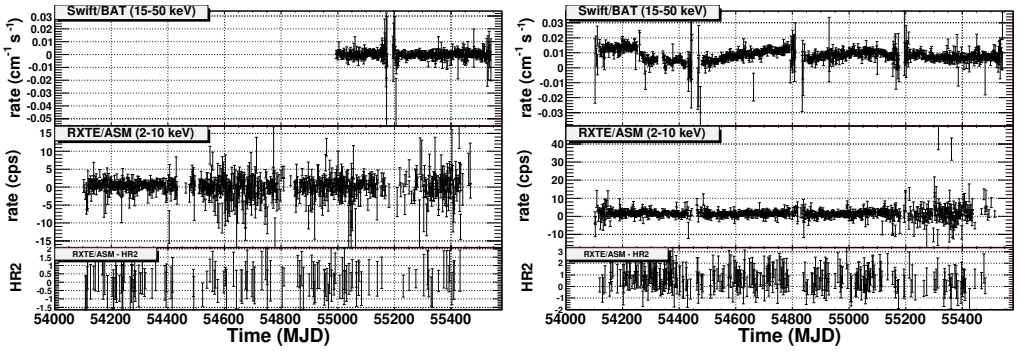

(g) *XTE J1748-288*

(h) *GRS 1758-258*

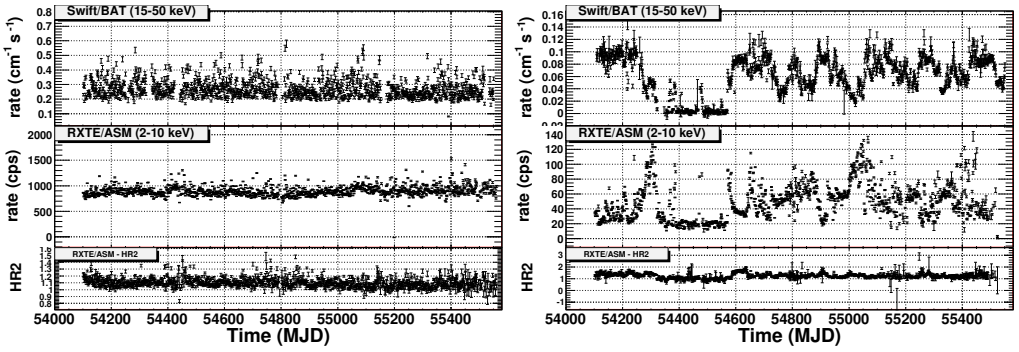

(i) *Scorpius X-1*

(j) *GRS 1915+105*

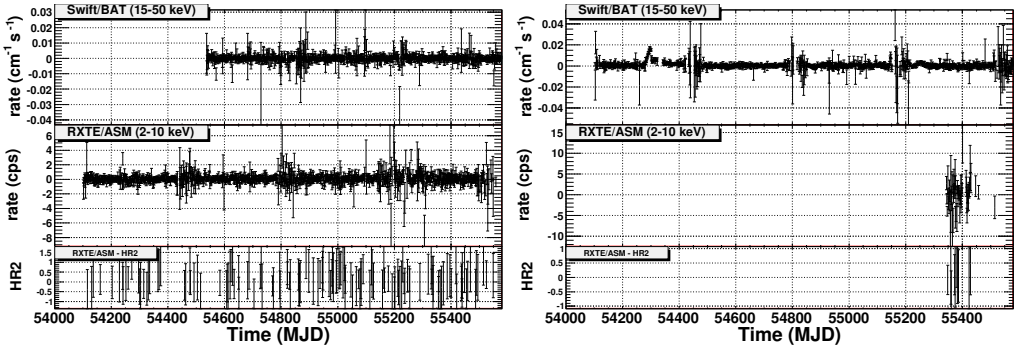

(k) *XTE J1859+226*

(l) *IGR J17091-3624*

Figure 5.3: *Daily averaged X-ray light curves of the sources under study in 2007-2010.(cont.)*

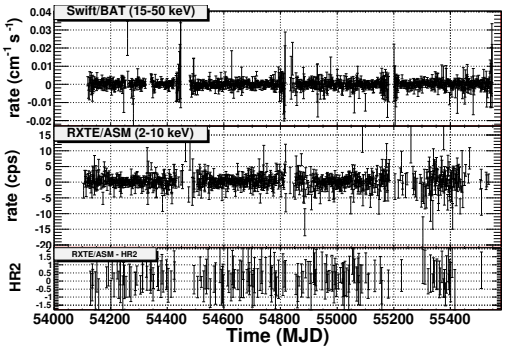

(m) *V4641 Sgr*

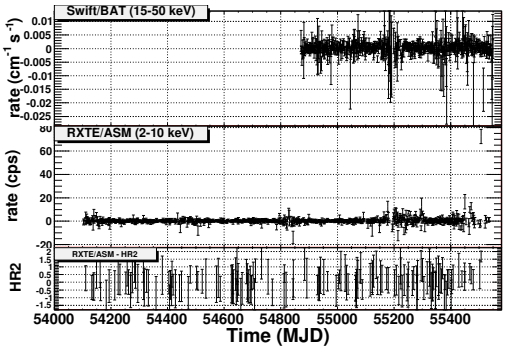

(n) *LS 5039*

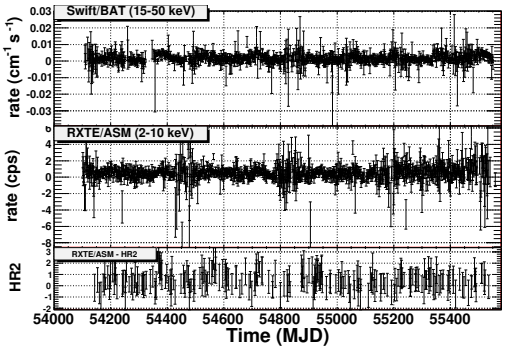

(o) *SS 433*

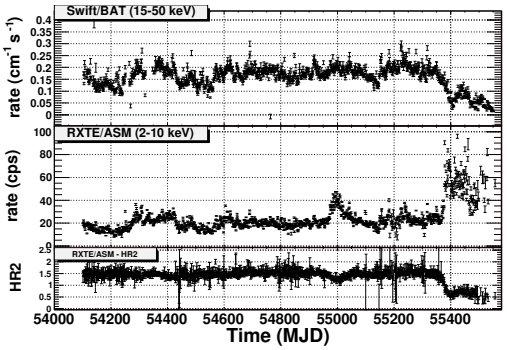

(p) *Cygnus X-1*

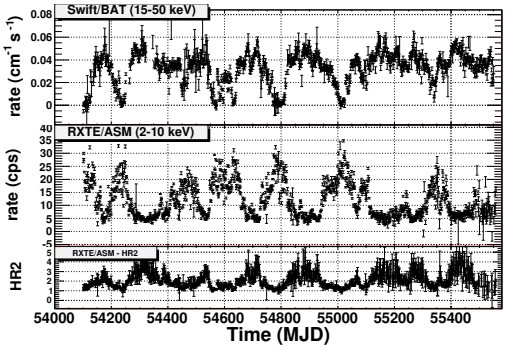

(q) *Cygnus X-3*

Figure 5.3: *Daily averaged X-ray light curves of the sources under study in 2007-2010.(cont.)*

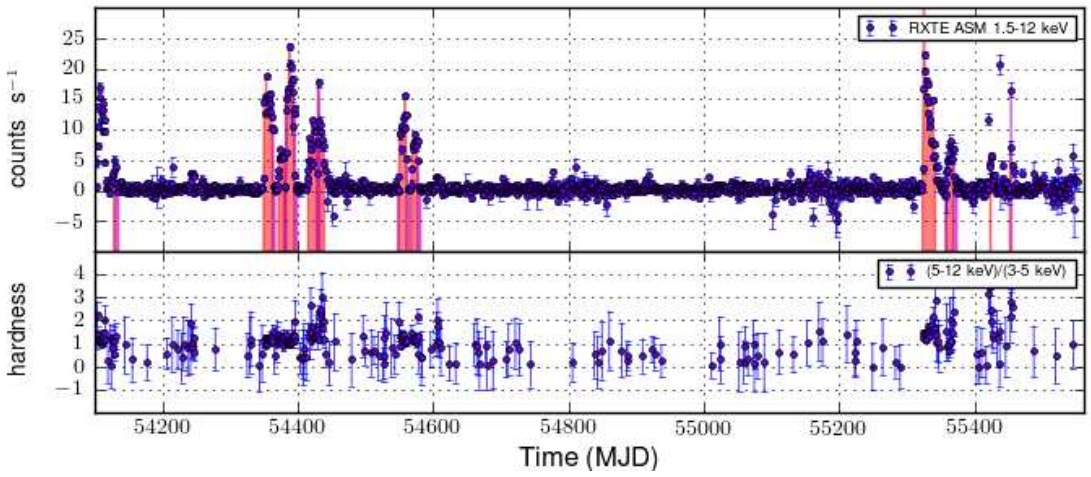

Figure 5.4: *X-ray light curves of Cir X-1 between 2007 and 2010 from RXTE ASM (top) and the hardness ratio HR2 from ASM (bottom). The filled areas refer to the periods selected for the neutrino search: in red are marked the periods of enhanced X-ray activity, in purple the near-by periods when the radio outburst at superior conjunction is expected. Both are selected for a single neutrino search for this source.*

5.2.1 Cir X-1

Circinus X-1(Cir X-1) has recently been confirmed as a neutron star binary after the observation of type-I thermonuclear bursts (Linares et al., 2010) and it is the only neutron star microquasar considered in this analysis. It is often referred to as a "peculiar" neutron star binary, since it does not fully match any of the classifications for these objects, roughly divided into Z-sources and atoll sources according to their spectral and timing characteristics (cf. § 4.5.2). It has an orbital period of 16.6 days, which has been measured from the modulation of the X-ray light curve (Kaluzienski, Holt, et al., 1976). This source also undergoes regular radio flares with the same period, interpreted as enhanced accretion near periastron passage in a highly eccentric orbit (Murdin et al., 1980). A recent high angular resolution monitoring campaign in the radio, conducted with e-VLBI in 2009, has confirmed this behaviour, observing an enhanced radio emission between orbital phase 0.09 and 0.21 (Moin et al., 2011), although these measures were taken during a period of very low activity in both radio and X-rays. It is one of the few confirmed neutron star binaries with resolved radio jets, which have been studied up to sub-arcsecond scales (Calvelo et al., 2012). Simultaneous radio and X-ray observations conducted by R. Fender et al. (2004) have shown that an increased accretion rate, in the form of an X-ray outbursts, is followed by a brightening of the radio core of the source, the jets, that successively feed two radio knots of an extended structure at arcsec scale.

Outburst selection

The overall light curve in Figure 5.4 shows that the source has undergone several outbursting events, better visible in the soft X-rays with ASM, some of which are zoomed in Figure 5.5. The periods of these outbursts have been selected for the

Table 5.1: *Periods and relative orbital phases in which Circinus X-1 has shown an outburst in the ASM light curve between 2007 and 2010. In most cases the X-ray activity ends around orbital phase 0.8-0.9 (see text).*

ASM outbursts (MJD)	Orbital phases
54128-54130	0.61 0.85
54349-54363	0.10 0.95
54371-54380	0.43 0.98
54381-54395	0.04 0.89
54415-54428	0.10 0.88
54430-54440	0.01 0.61
54549-54561	0.21 0.93
54567-54577	0.30 0.90
55323-55343	0.06 0.27
55359-55369	0.24 0.84
55423-55425	0.11 0.23
55452-55454	0.87 0.99

analysis, their start and stop time have been computed using the same criteria described at the beginning of this section for the outburst selection. As one can see in Table 5.1, nine of the twelve periods end around orbital phase[4] 0.8-0.9, while two of them start around phase 0.2-0.3. These have been extended (forward or backward) to include the phase interval 0.09-0.21 ($\sim$ 4 days more), when the enhanced radio flare is expected. The final selected periods are highlighted in Figure 5.4 and listed in Table 5.3 at the end of this chapter.

[4]The orbital phases of Cir X-1 have been calculated using the ephemeris in (Nicolson, 2007).

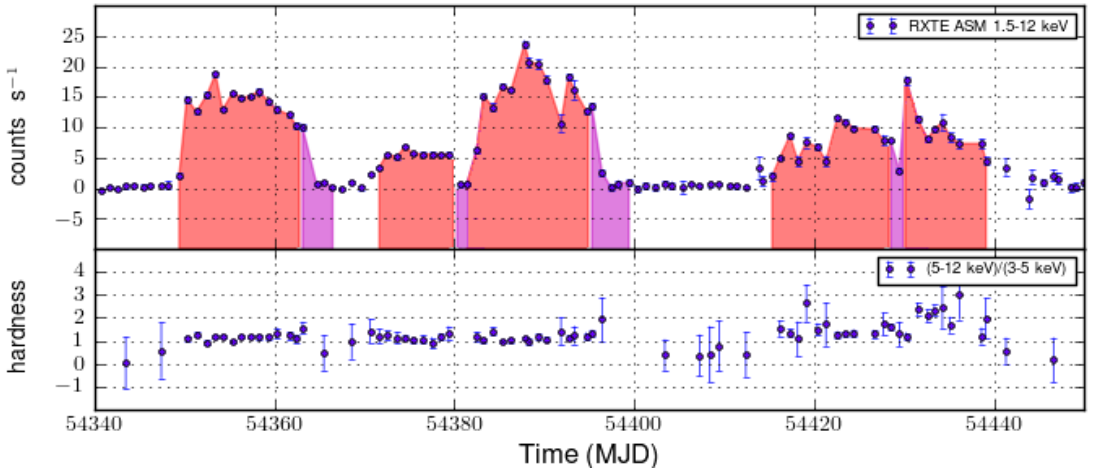

(a)

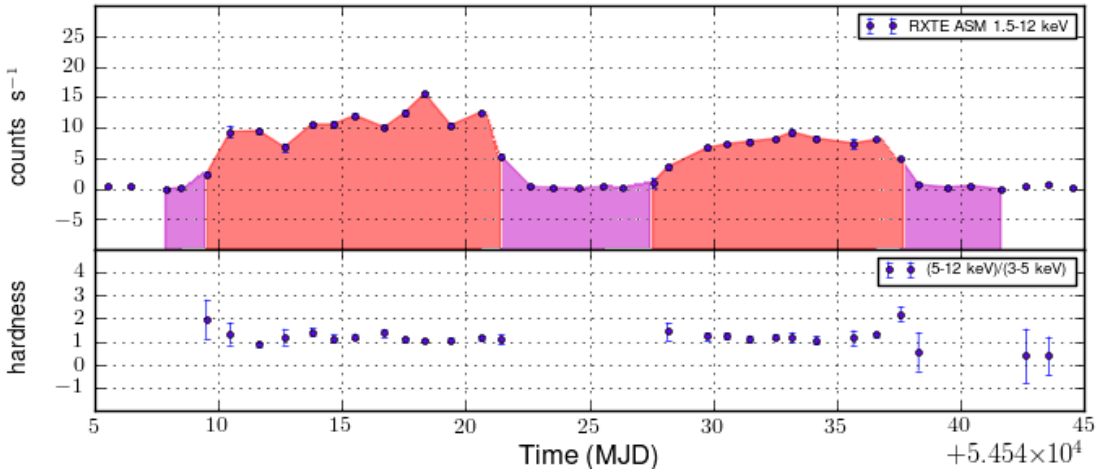

(b)

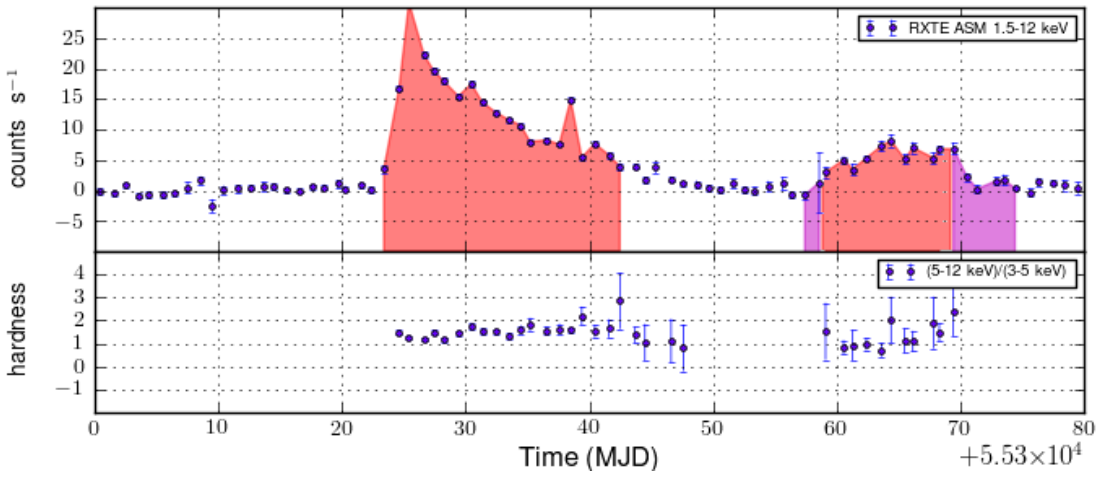

(c)

Figure 5.5: *Some of the Cir X-1 outbursts. The period selected for the analysis is highlighted in red. Here the BAT light curve is not shown since the source is not bright enough in its energy range.*

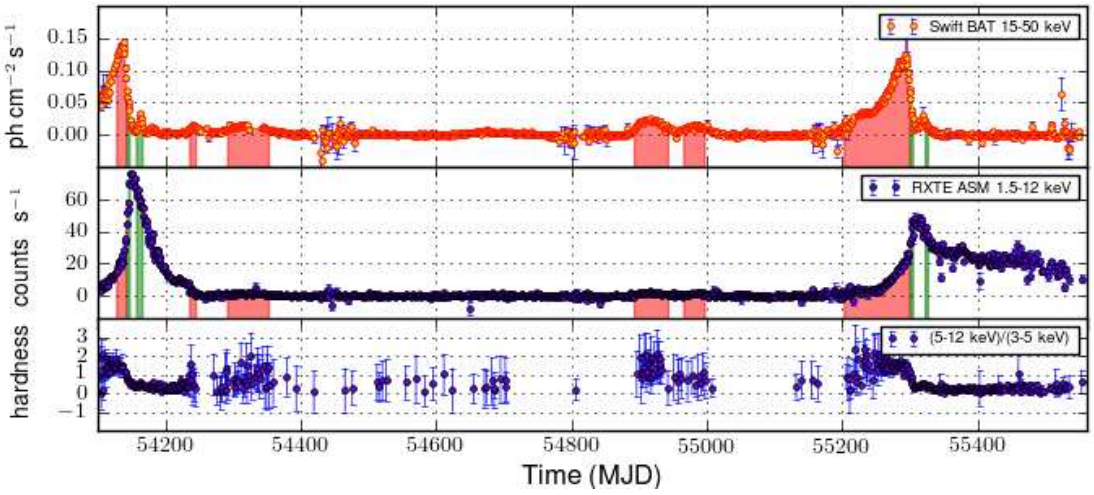

Figure 5.6: *X-ray light curves of GX 339−4 between 2007 and 2010, from Swift BAT (top) and RXTE ASM (middle). The lower panel shows the hardness ratio HR2 from ASM. The filled areas refer to the periods selected for the neutrino search: in red during the hard state and in green during the hard to soft transition. A separate neutrino search is performed on red and green areas.*

5.2.2 GX 339−4

Since its discovery in 1973 with the OSO-7 satellite (Markert et al., 1973), GX 339−4 showed a high X-ray variability and was observed transiting through different states, that were identified as *high*, *low* and *off*, according to their intensity. Hynes et al. (2003) measured a mass function of $5.8M_{\odot}$, thus giving the first dynamical proof that the system harbours a black hole, and obtained the first reliable estimate of the orbital period of 1.7 days. A lower limit to the distance of $\sim$ 6 kpc was obtained by means of a high resolution spectroscopic analysis of the Na D lines (Hynes et al., 2004), whereas by combining different results an accepted value for the distance is $\sim$ 8 kpc (Zdziarski et al., 2004). Since the system is not eclipsing, the inclination angle of the jet with respect to the line of sight has to be $\lesssim 80°$, Shidatsu et al. (2011) computed a best-fit value of $\approx 50°$.

Outburst selection

GX 339−4 is a recurrent black hole transient that has undergone two major outbursts, one in 2007 and one in 2010 both featuring a hard to soft transition, and some fainter ones visible only in the BAT light curve (Figure 5.6). For this source two different time selections are made, which will be analyzed separately: during hard states and during state transitions. The hard states are looked for as outbursts in the BAT light curve, while the times of the transitions as well as of the onset of the soft state are estimated using spectral X-ray observations found in the literature.

During the May 2002 outburst, this source has been observed producing a very bright optically thin radio flare at the completion of the hard-soft transition, when the ASM flux attained its maximum (Gallo, Corbel, et al., 2004). Unfortunately no analogous observations have been found in the literature for the outbursts in

2007 and 2010 that could establish the exact time of the radio flare. This has been approximated using detailed X-ray observations reporting the time of the HIMS to SIMS transition, which is related but not coincident with the major ejection. For these transitions a separate search will be performed w.r.t. the one during the hard state, with a time window centered at the estimated transition time ±2.5 days.

The outburst in Figure 5.7a was first detected in Dec 2006 by Swift/BAT(Krimm, 2006) and lasted until the first months of 2007. At the beginning of ANTARES data taking (5-lines configuration) the source was already in the hard state, so the first day selected is MJD 54128. Radio observations conducted with the ATCA telescope between 4 and 18 Feb 2007 (MJD 54135-54149) have measured a variable flux in the range of 1-25 mJy and a spectral shape ranging from flat to very steep spectrum, likely suggesting that the source was undergoing a series of plasma ejections (Corbel, Tzioumis, et al., 2007). Motta, Belloni, and Homan (2009) present a detailed study of the spectral time evolution of GX 339-4 during this outburst, the transition from the HIMS to the SIMS is observed around MJD 54145.5 and then again around MJD 54160 and MJD 54164.

Another similar outburst was observed in the first half of 2010, the corresponding X-ray light curves are shown in Figure 5.7c. ATCA detected on 28 March 2010 (MJD 55283) a radio flux density of the order of 20 mJy, typical of the compact jet of the hard state. The decay phase of the outburst and the subsequent transition to softer states has been followed by RXTE/PCA pointed observations in (Belloni et al., 2010), which locate the transition from the HIMS to the SIMS at around MJD 55304, after which the source was observed undergoing a transition to the soft state and then to the SIMS until MJD 55316. On MJD 55320 the X-ray spectrum was compatible with the source being in the HIMS again (Motta, Belloni, Muñoz-Darias, et al., 2010), but the subsequent transition was not observed, though from the light curves the time at which it occurred can be estimated around MJD 55324.

Some other outbursts, in which the transition to the soft state was not completed, were observed in between the two just described. These were characterized by an increase of the BAT flux while they were extremely faint in the ASM energy range, indicating that the source was in the low luminosity hard state. X-ray and radio observations during the 2009 outburst (Figure 5.7b) measured a power law X-ray spectrum with a 1.5 spectral index (Swift/XRT), typical of the hard state, and a radio flux density of 3.5 mJy (MOST) (Still et al., 2009; Hunstead et al., 2009).The selected periods are listed in Table 5.3.

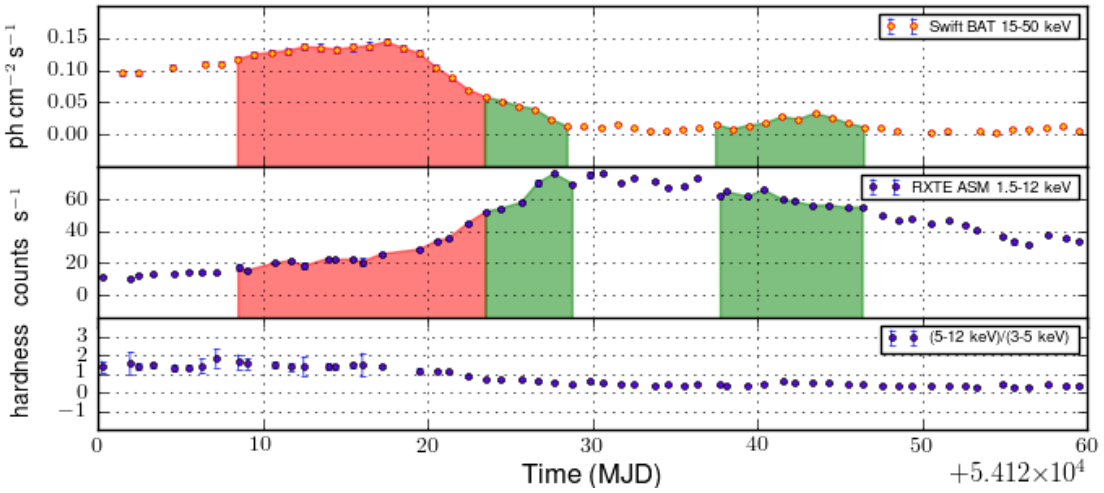

(a)

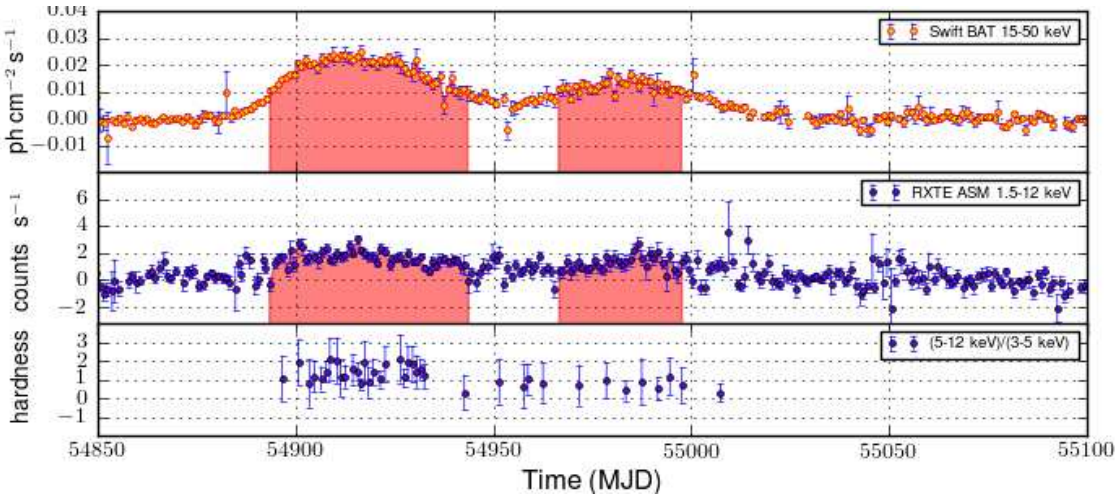

(b)

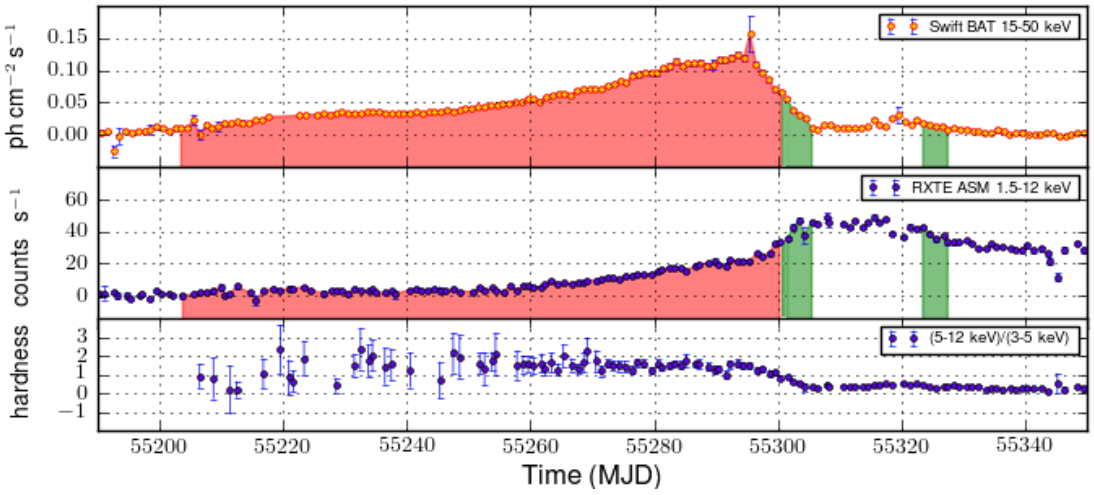

(c)

Figure 5.7: *GX 339-4 outbursts during 2007 (a), 2009 (b) and 2010 (c). The periods selected for the analysis (see text) are highlighted in red for the hard state and green for the hard →soft transition.*

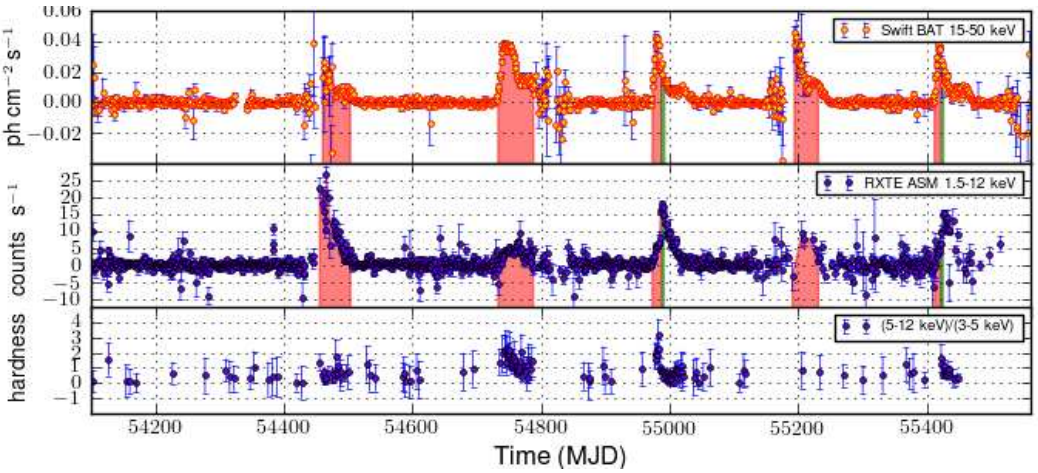

Figure 5.8: *X-ray light curves of H1743−322 between 2007 and 2010, from Swift BAT (top) and RXTE ASM (middle). The lower panel shows the hardness ratio HR2 from ASM. The filled areas refer to the periods selected for the neutrino search: in red during the hard state and in green during the hard to soft transition.*

5.2.3 H1743−322

H1743−322 was discovered in 1977 during an X-ray outburst with the Ariel 5 all-sky monitor (Kaluzienski and Holt, 1977) and was detected again in 2003 by INTEGRAL and RXTE. Analyzing the 2003 outburst, McClintock, Remillard, et al. (2009) classified it as a black hole candidate, due to the similarity of the observed X-ray behaviour with that of the well known system XTE J1550−564, although a mass function for H1743−322 has not yet been measured. Large scale X-ray jets, a very rare feature in microquasars present only in XTE J1550−564, were observed one year after the 2003 outburst using Chandra (Corbel, Kaaret, et al., 2005). Constraints on the distance and the inclination angle have been obtained by applying a model in which the jets propagate freely within a parsec-scale cavity around the source, until they encounter the surrounding interstellar medium. Using this purely kinematic model, Steiner et al. (2012) estimated a distance of ≈ 8.5 kpc and an inclination angle $i \approx 75°$. For this system, the orbital period is not yet known.

Outburst selection

H1743−322 has undergone five outbursts between 2007 and 2010 (Figure 5.8). Three of them have received a satisfactory coverage in X-rays, while the remaining two could not be observed well, since they happened while the source was close to the sun direction. The same selection scheme as for GX 339−4 is applied here for H1743−322, with two separate selections for the hard and transitional state.

The outburst at the end of 2008, shown in Figure 5.9a, has been classified as a failed outburst (Capitanio et al., 2010), since the source remained between the hard state and the HIMS without reaching the soft state or the SIMS. During MJD 54744, ATCA detected a radio flux of ∼2 mJy with an optically thin spectrum (Corbel, Tzioumis, et al., 2008).

The successive outburst during 2009, Figure 5.9b, has received a quite satisfactory X-ray coverage. A detailed analysis of the X-ray spectra (Chen et al., 2010) indicates a HIMS→SIMS transition at MJD 54990, which has been included in a time window of ±2.5 days for the transitional phase search (green area in the plot).

The evolution of the outburst detected in 2010 (Figure 5.8) is described in (Nakahira et al., 2010, and references therein). A HIMS→SIMS is observed around MJD 55424.5, after which the source stays in the soft state until quiescence. The selected periods are listed in Table 5.3.

The remaining two outbursts observed around MJD 54500 and MJD 55200 (the 1st and 4th highlighted in Figure 5.8) did not receive a good coverage in X-rays due to sun constraints. The first outburst was detected around MJD 54453 and lasted until MJD 54504 (Kalemci et al., 2007; Jonker et al., 2010). The second outburst was detected around MJD 55191 until MJD 55237 (Yamaoka et al., 2009). These have also been included in the analysis as hard states, since it is not known whether eventual state transitions have taken place.

5.2.4 IGR J17091−3624

IGR J17091−3624 was discovered relatively recently in 2003 with INTEGRAL (Kuulkers et al., 2003) during an outburst in which the source reached a flux of 20 mCrab in the 40-100 keV energy band. A subsequent observation with the Very Large Array revealed a radio counterpart with a steeply falling spectrum typical of synchrotron emitters (Rupen et al., 2003). Pandey et al. (2006) successively confirmed the radio source and hypothesized it could be a microquasar.

Outburst selection

This source was added to the RXTE ASM monitoring catalog only in 2010, whereas the full light curve between 2007 and 2010 is available with Swift BAT. A small outburst is observed in the BAT light curve between MJD 54286-54301, this has been selected for the analysis. XRT observations during that period confirmed a hardening of the X-ray spectrum (Kennea et al., 2007) (Table 5.3.).

5.2.5 Cyg X-1

Cyg X-1 is one of the brightest X-ray sources in the sky and as such was discovered in the early years of X-ray astronomy, in a rocket flight experiment in 1964 (Bowyer et al., 1965). The radio counterpart was detected some years later in 1971 (Tananbaum et al., 1972), when the onset of the radio emission followed a hardening of the X-ray emission detected by the satellite Uhuru. Its orbital period was found to be 5.6 days and the orbital elements implied a constrained mass for the unseen object to be higher than the maximum value for a neutron star, thus the system contains a black hole (Webster et al., 1972).

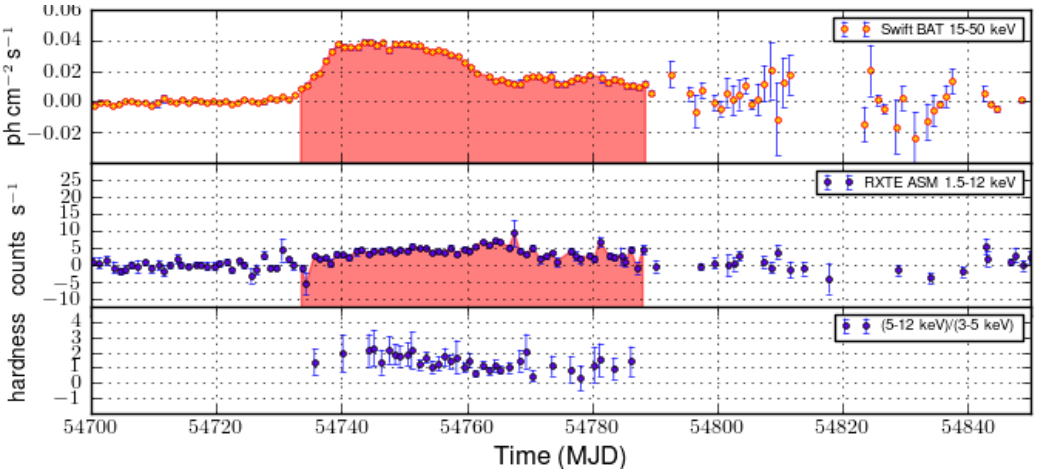

(a)

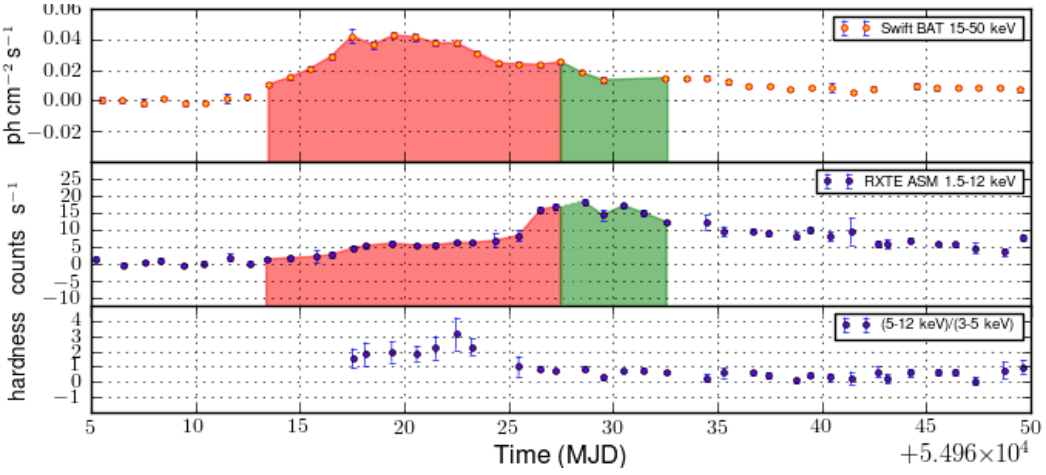

(b)

Figure 5.9: *H 1743-322 outbursts, zoomed from Figure 5.8. The periods selected for the analysis (see text) are highlighted in red for the hard state and green for the hard →soft transition.*

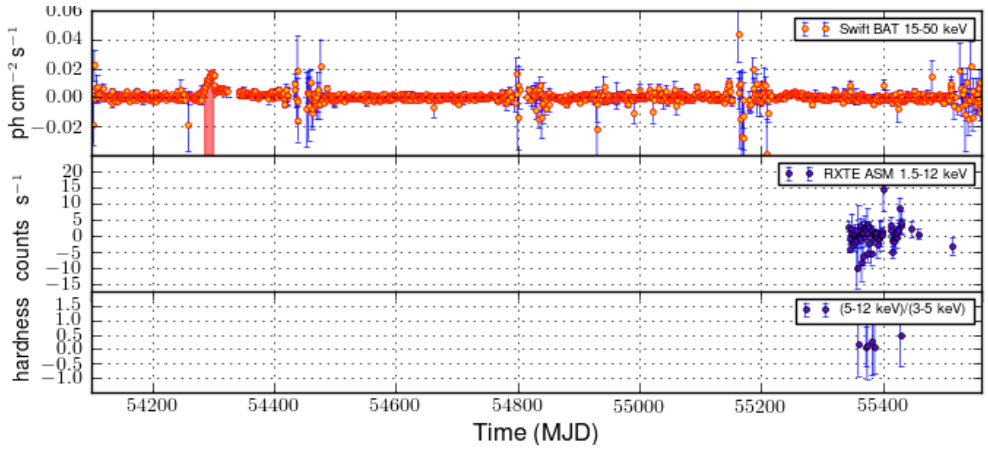

Figure 5.10: *X-ray light curves of IGR J17091−3624 between 2007 and 2010, from Swift BAT (top) and RXTE ASM (middle,bottom). The selected outburst is highlighted in red.*

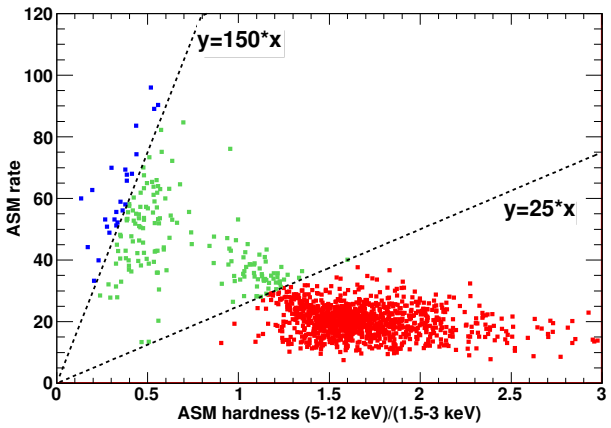

Figure 5.11: *HID of the ASM rate vs. the HR1 obtained with all the daily ASM measures during 2007-2010, used to classify X-ray states of Cyg X-1 according to (Rodriguez et al., 2011). The two straight lines divide the plane in three areas associated to the hard, transitional and soft state, in red, green and blue respectively.*

Outburst selection

As shown in the light curve in Figure 5.3p, Cyg X-1 is always very bright in X-rays and spends most of the time in the hard state. As other BHBs this source undergoes full transitions from hard to soft state and back. Besides, it is known to undergo so called "failed transitions", in which it enters an intermediate X-ray state without completing the transition into the soft state. These transitional phases can be associated with major radio flares and relativistic ejections of matter, as for other BHBs. Rodriguez et al. (2011) use exact state classification from spectral fits of the bi-weekly RXTE PCA and HEXTE taken since 1998 to calibrate a classification of X-ray states of Cyg X-1 based on ASM rate and HR1 hardness ratio alone. The results of this classification are summarized in the hardness intensity diagram (HID) in Figure 5.11, where the green dots individuate the transitional phases, dots below the lower straight line are associated to hard states and all the others are soft states. Figure 5.12 is shows the ASM X-ray light curve during the whole 2007-2010 period with daily averaged data points, and the HR2 hardness ratio. Different states are represented by different shaded area colours, red for the hard and green for the transitional. The selected periods are listed in Table 5.3.

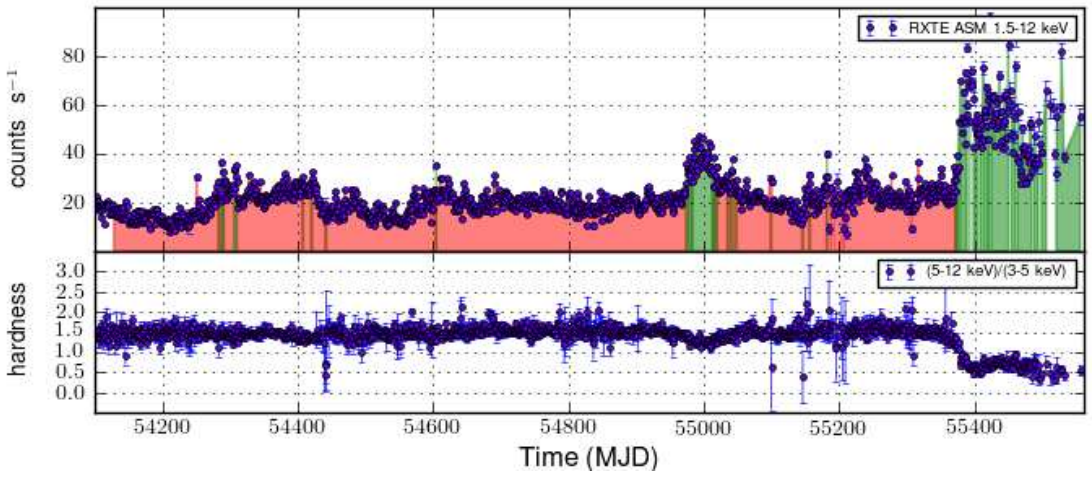

Figure 5.12: *X-ray light curves for Cygnus X-1 between 2007 and 2010. Different colours in the ASM panels represent different X-ray states: red for the hard, green for the transitional and blue for the soft state.*

5.3 Outburst selection for Cyg X-3 using γ-rays

Cyg X-3 was discovered during a survey of the Cygnus region with rocket flights by Giacconi et al. (1967). It is a high-mass binary with a Wolf-Rayet companion star (van Kerkwijk et al., 1992) rotating in a 4.8h orbit (Parsignault et al., 1972) around a compact object of yet unspecified nature. This source is known particularly for undergoing massive radio outburst, which attained up to 20 Jy flux densities (Gregory et al., 1972). The presence of the jets was put in evidence by the observation of a two sided radio structure at arcsec scale (Strom et al., 1989). Martí et al. (2001) observed the time evolution of the knots and inferred a mildly relativistic jet velocity of $\sim 0.5c[D/10$ kpc], where D is the distance of the source. First estimates of the distance based on the 21-cm line absorption were obtained after the 1972 and 1983 radio outbursts and seemed to be compatible with Cyg X-3 being extragalactic (Lauqué et al., 1973; Dickey, 1983), since a lower limit to the distance of ~ 11 kpc was found. Ling et al. (2009) used a geometric method based on the observation of the halo X-ray emission of Cyg X-3 scattered from a dust cloud, supposedly the Cyg OB2 association, determining a distance of 7.2 kpc. Using this distance value, the intrinsic motion of the jets becomes $\sim 0.35c$.

In the following part of this section, the procedure employed to obtain the Fermi/LAT light curve and the time selection chosen from it will be described.

5.3.1 Analysis of Fermi/LAT data

This analysis has been performed using HEASOFT v6.11 and ScienceTools-v9r23p1. The LAT data have been retrieved from the Fermi Science Support Center (FSSC) web interface[5], the summary of the query is shown in Table 5.2. The data consist of several photon files and a spacecraft file, all in FITS format.

[5]http://fermi.gsfc.nasa.gov/cgi-bin/ssc/LAT/LATDataQuery.cgi

Table 5.2: *Query to obtain Fermi/LAT data for Cygnus X-3*

Search Center (RA,Dec)	(308.107,40.9577)
Radius	15 degrees
Start Time	2008-08-04T15:43:37
Stop Time	2011-01-01T00:00:00
Minimum Energy	100 MeV
Maximum Energy	100000 MeV

The basic data reduction has been done using the standard tools `gtselect` and `gtmktime`. Good quality events with $evclass = 2$ or 3 were selected within a radius of 15° around the source position. To reduce the background photons coming from the Earth Limb, cuts on the maximum zenith angle value of 100° and on the maximum rocking angle of 52° have been applied.

Thirty arcminutes away from Cygnus X-3 lays the gamma ray pulsar PSR 2032+4127. The ephemeris from (Abdo et al., 2009a) was used to calculate the pulsar phase correspondent to each photon event, together with the tools `gtephem` and `gtpphase`. This allowed the selection of only those events falling within the off-pulse phase intervals: 0-0.12, 0.2-0.6 and 0.72-1; which removed 20% of the livetime.

The `gtltcube` program has been used to calculate the 'livetime cubes', that relate each position in the sky to the time spent by the detector observing it at each inclination angle. These are needed for the 'exposure map' calculation, done with `gtexpmap`, that gives the total exposure (area multiplied by time) for a given position in the sky producing counts in your region of interest. The exposure maps take into account the detector response function, thus they also depend on the energy of the photons. The response function used in this analysis is the "Pass 6 v11" (`P6_V11_DIFFUSE`).

To obtain the light curve, the data have been processed with `gtlike`, which implements an unbinned likelihood method to calculate photon fluxes. The contributions from all the sources located within the region of interest (15°) plus 5° are taken into account by the method[6].The model file, that collects all the nearby sources with their spectral parameters, was built using the first Fermi LAT catalog (1FGL)(Abdo et al., 2010). The data have been analyzed in time bins of four days, the resulting light curve is shown in Figure 5.13.

5.3.2 Outburst selection

The selection of γ-ray flares with the light curve just obtained has been performed in the same fashion as the one described for the X-rays in § 5.2, with some modifications due to the different nature of the data. The procedure adopted is the following:

- perform a Gaussian fit on the $\log_{10}(flux_\gamma)$ distribution to calculate mean value, or *baseline* and its standard deviation σ,

[6]The extra five degrees is to account for sources outside the region of interest which may contribute at lower energies due to the larger PSF there.

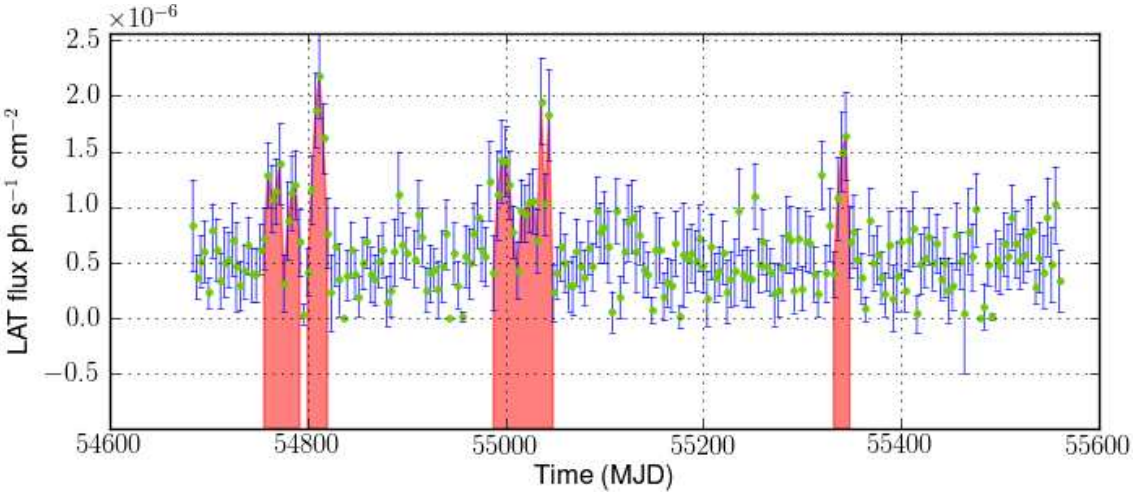

Figure 5.13: *Fermi LAT light curve of Cygnus X-3 from Aug 2008 to Dec 2010.*

- the fit is repeated twice within the interval $\langle \log_{10}(flux_\gamma) \rangle^{+\sigma}_{-2\sigma}$
- select all the flux measures for which $flux_\gamma - \sigma_{flux} > 10^{\langle \log_{10}(flux_\gamma) \rangle}$
- the time of each selected measurement is included in the analysis with a time window of 4 days around it, which is the binning used to produce the light curve.

During the γ-ray flares, a correlation of the LAT flux with the radio emission from the relativistic jets has been observed with a time lag of the radio to the γ-ray flare of about 5 ± 7 days (Tavani et al., 2009). If the γ-ray flare is due the IC up-scattering by jet electrons, then a radio flare is expected few days later as the gas of electrons expands and becomes transparent to the synchrotron emission. Multi-wavelength observations taken during the May 2010 outburst (Williams et al., 2011), observed a 1 Jy radio flare preceding, instead of following, the major γ-ray flare by 1-2 days, which would not be explained by the IC up-scattering model. Possible explanations for this involve the re-energization of the jet electrons due to a collision with a clump of the companion star wind. While, if the γ-rays would be emitted during the ejection event, a hadronic composition of the jet would explain the higher ratio of γ-ray to radio luminosity. To take into account the two possibilities of a positive and of a negative time lag, the selected time windows have been extended by 5 days before and after. The light curve is shown in Figure 5.13, the selected periods are listed in Table 5.3.

Table 5.3: *Candidate microquasars and selected periods.*

Source Name	Selected periods (MJD)
Circinus X-1	54128-54136, 54349-54367, 54371-54400, 54415-54442 54547-54582, 55323-55343, 55357-55375, 55421-55426 55452-55458
GX 339-4 (hard state)	54128-54143, 54236-54246, 54292-54354, 54893-54944 54966-54998, 55203-55301
(transition)	54143-54148, 54157.5-54166.5, 55301-55306, 55323-55328
H1743-322 (hard state)	54453-54504, 54733-54789, 54973-54987.5, 55191-55237, 55412-55422
(transition)	54987.5-54992.5, 55422-55427
IGR J17091-3624 (hard state)	54286-54301
Cygnus X-1 (hard state)	54128-54283, 54284-54287, 54288-54289, 54291-54306, 54310-54407, 54408-54420, 54421-54441, 54442-54604, 54605-54974, 54976-54977, 54982-54983, 55013-55014, 55016-55018, 55020-55035, 55036-55040, 55043-55048, 55049-55099, 55100-55146, 55147-55156, 55157-55182, 55183-55184, 55186-55190, 55192-55206, 55207-55372 55373-55374
Cygnus X-1 (transition)	54283-54284, 54287-54288, 54289-54291, 54306-54310, 54407-54408, 54420-54421, 54441-54442, 54604-54605, 54974-54976, 54977-54982, 54983-55013, 55014-55016, 55018-55020, 55035-55036, 55040-55043, 55048-55049, 55099-55100, 55146-55147, 55156-55157, 55182-55183, 55372-55373, 55374-55378, 55379-55388, 55389-55390, 55393-55394, 55398-55399, 55400-55405, 55408-55415, 55417-55418, 55419-55423, 55425-55451, 55454-55461, 55463-55485, 55488-55492, 55494-55495, 55499-55500, 55506-55507, 55521-55523, 55528-55530, 55532-55533, 55556-55557
Cygnus X-3	54753-54795, 54797-54823, 54985-55051, 55329-55351

Chapter 6

Analysis of the ANTARES data

This chapter describes the analysis of the ANTARES data optimised to the search for neutrino emission from the candidate microquasars selected in § 5. The search is restricted to those periods when a source is thought to accelerate a relativistic jet, these periods were defined in § 5 and are listed in Table 5.3.

The analysis is performed on all the data taken between January 2007 and the end of 2010. During this period of time, ANTARES operated with only 5 lines up to December 2007, when it was upgraded to 10 lines, and then to its full configuration with 12 lines in May 2008. Due to the maintenance of faulty lines, detector configurations with only 9 lines are also present in the data sample. For simplicity, no distinction will be made between the latter and the "12 lines configurations" in this chapter, since these slightly different configurations do not affect the detector performances to an extent where a separate analysis is necessary.

The statistical method used to infer the presence of a neutrino source, or to calculate the flux limits in case no discovery is made, is an unbinned likelihood method based on a likelihood ratio test. To avoid biased results, given the low number of expected signals, a blind strategy has been used to optimize the cuts for the event selection. The true neutrino directions in celestial coordinates have been unveiled only at the end of this process, once the periods and cuts were defined independently for each candidate source. The optimization of the cuts has been done in order to minimize the flux needed for a discovery thus maximizing the discovery potential.

The detailed analysis is presented in the following.

6.1 ANTARES Data processing

6.1.1 Selection of the data set

The data runs to be included in the analysis have been selected according to the quality criteria officially used by the collaboration, whose relevant information is found in the ANTARES data base in the table called `Data_Quality`. A `QualityBasic` parameter has been defined in the range of integers between 0 and 4, so that a `QualityBasic` ≥ 1 is associated to all the runs for which no problems were encountered during the data taking. The minimum requirements for such a

Table 6.1: *Number of data runs and corresponding livetime of the whole data set used in the analysis, also separated between 12 lines and 5 lines period (top) and corresponding to the burst periods selected for the analysis of each source (bottom) The livetime already accounts for the visibility factor.*

	Number of runs	Livetime (days)
all	7411	813.3
12 Lines	6017	630.5
5 Lines	1394	182.8
Cir X-1	776	100.5
GX 339−4 (HS)	1169	147.0
GX 339−4 (TS)	55	4.9
H1743−322 (HS)	883	84.6
H1743−322(TS)	49	5.1
IGR J17091−3624	55	8.5
Cyg X-1 (HS)	1568	174.4
Cyg X-1 (TS)	282	30.9
Cyg X-3	185	16.6

basic quality run, corresponding to `QualityBasic` = 1, are:

- no double frames
- no synchronization problems
- sampling< 3 (2007 only)
- reasonable muon rate, within 0.01-100 Hz
- apparent and effective duration so that $0 \leq T_{app} - T_{eff} \leq 450s$.

Al the runs selected in this analysis respect these quality requirements.

Each data run in ANTARES is associated to a specific *run setup*, which defines the trigger logics as well as the calibration set used during the data taking. A run setup which was still under test is labelled with the keywords "SCAN" or "PRELIM" and no calibration information is stored for it in the ANTARES data base. Runs taken with such run setups have been discarded from the analysis.

Some runs show an anomalous hit multiplicity for some events, which are reconstructed as point sources of light in the detector, centered around the position of an optical module. These events are thought to be produced by sparking optical modules and the runs containing them are referred to as *sparking runs*. In Figure 6.1 is shown the distribution of the hits selected by the track reconstruction for one of these runs, where one can clearly see the bump around 500 hits. The 25 runs that present this feature, thus being discarded from the analysis, are: 33608, 33610, 34663, 36600, 36666, 36670, 36689, 38347, 38348, 38349, 38351, 38352, 38353, 38355, 38357, 38482, 41668, 42507, 42511, 43196, 43215, 43684, 44030, 44035, 44070.

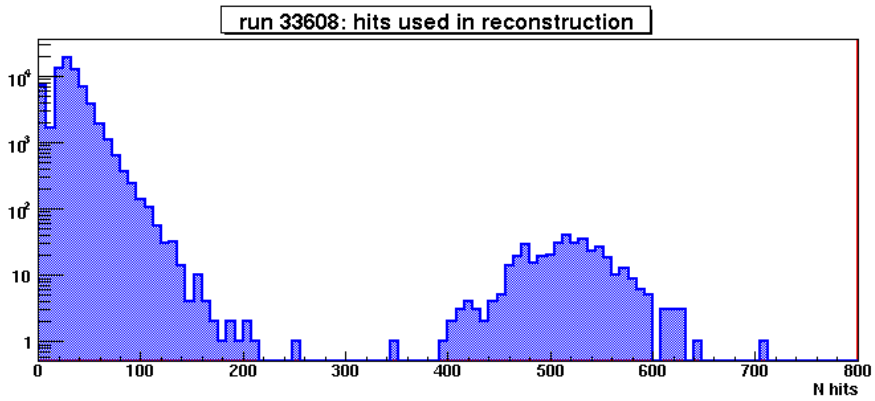

Figure 6.1: *Number of hits selected by the track reconstruction algorithm in a sparking run. The bulk of events with a high hit multiplicity is due to a sparking optical module. These events are reconstructed as point like sources of light centered on an optical module.*

A total of number of 7411 runs was selected, with a livetime of 813 days. This livetime is distributed differently among the candidate sources according to their selected periods. More details are given in Table 6.1.

6.1.2 Track reconstruction and event selection

ANTARES data have been calibrated, aligned and reconstructed using the SeaTray framework. The official data production used in this analysis is labeled `2011_05`, which uses the alignment version 0.994 for all runs.

Muon tracks have been reconstructed using the `aafit` package, which is a reconstruction strategy based on a maximum likelihood algorithm (Heijboer, 2004). The maximized likelihood of each reconstructed track, referred to as Λ, is used as a discriminating parameter to discern between upgoing neutrinos and mis-reconstructed downgoing muons. An example distribution of this parameter taken from the Monte Carlo is shown in Figure 3.8, which shows how a pure sample of upgoing neutrinos can be selected by putting a sufficiently high cut on Λ.

In this analysis the two parameters just presented have been used to apply quality cuts for the event selection. The choice of a specific set of quality cuts can influence to different extents the ability of the analysis to set a discovery or rather to set stringent flux limits. As a rule of thumb, a stricter quality cut can minimize the flux needed for a discovery by reducing the background, while a looser one can provide a better sensitivity by increasing the signal. In this analysis, quality cuts have been optimized to minimize the discovery potential. For this reason, four cuts on Λ have been tested: $\Lambda > -5.0$, -5.2, -5.4 and -5.6. The cut on the angular error estimate has been fixed to $\hat{\beta} < 1°$ and used as such in all cases.

The number of selected events in each of the four selected samples is shown in Table 6.2, for each neutrino search. The numbers in Table 6.2 are used to estimate the rate of background events in the pseudo-experiment generation, this is shown in § 6.3.1. The results of the cut optimization are presented in § 6.3.3.

Table 6.2: *Number of selected events in data (upgoing tracks) and in the whole sky, detected during the outbursting time of each source under study. These numbers refer to the events selected while the source was under the horizon, i.e. visible by ANTARES. They represent the total background at the detector for each neutrino search, and will be used to estimate the background in the pseudo-experiment generation (§ 6.3.1). Four different cuts on Λ are compared. The corresponding livetime is shown.*

Source		Selected Events				Livetime
		$\Lambda > -5.0$	$\Lambda > -5.2$	$\Lambda > -5.4$	$\Lambda > -5.6$	(days)
Cir X-1		139	256	583	1607	100.5
GX 339−4	(HS)	316	484	956	2609	147.0
	(TS)	3	5	14	45	4.9
H1743−322	(HS)	283	447	746	1817	84.6
	(TS)	10	20	27	90	5.1
IGR J17091−3624		10	16	40	120	8.5
Cyg X-1	(HS)	417	638	1254	3210	174.4
	(TS)	58	109	182	507	30.9
Cyg X-3		64	93	149	333	16.6

6.2 Data - Monte Carlo comparison

The Monte Carlo used is the official run-by-run production version 0.1.1 [1]. Atmospheric ν_μ's and $\bar{\nu}_\mu$'s have been generated with `GENHEN` using Bartol flux, in the energy range $100 - 10^8$ GeV and in a 4π solid angle, simulating also downgoing neutrinos. A total of 5×10^8 interactions per neutrino type and per simulated run have been generated. Atmospheric muons have been simulated with `MUPAGE`, for each run a number of events reproducing 10% of its livetime was produced.

By comparing the distribution of the reconstruction quality Λ obtained from the data with that obtained from the simulations, it has been found that the two curves agree best when a 2ns smearing on the arrival time of the hits is applied at the OM level in simulations. The reason why the data are better represented by a degraded Monte Carlo has been clarified by further investigations and ascribed to a too optimistic simulation of the transit time spread at the optical modules. This effect is currently being implemented in official simulations. The Monte Carlo shown here, though, accounts for this effect by applying a 2 ns smearing to the arrival time of the hits.

The comparison between the distribution of the reconstruction quality Λ in data (black) and Monte-Carlo (magenta for the muons and red for the neutrinos) is shown in Figure 6.2a for all upgoing events with angular error estimate $< 1°$. Figure 6.2b shows the comparison between the reconstructed zenith angles. The distributions of Λ during the selected time windows for each search are shown in Figure 6.3, from which it is possible to see that no bias is introduced when applying a cut on Λ on a reduced time window. This can also be seen in Table 6.3 where the number of

[1] http://antares.in2p3.fr/internal/dokuwiki/doku.php?id=run_by_run

selected events in data and MC are compared for different Λ-cuts.

When $\Lambda \lesssim 6.5$ a factor ~ 4 more events are found in the data than in simulation. This discrepancy is due to some runs with an exceptionally high optical noise which is not reproduced in simulations. This effect does not affect the event selection with the Λ-cuts applied in this analysis.

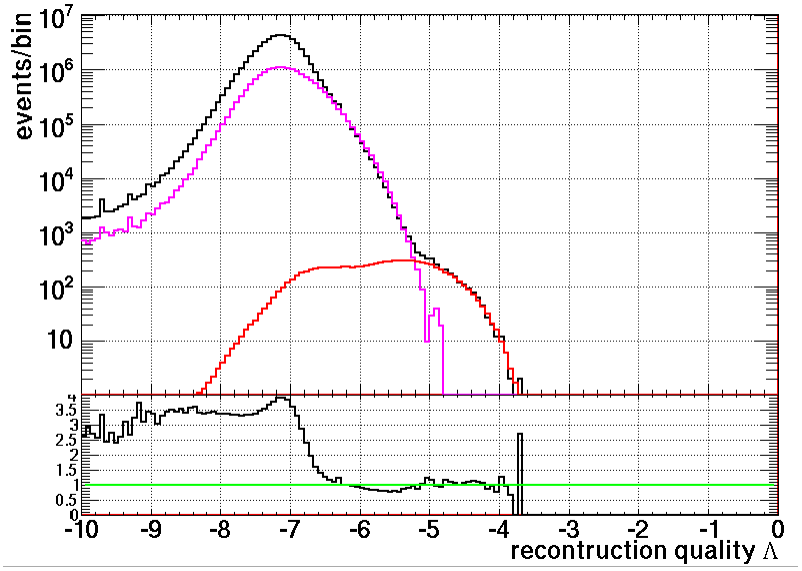

(a)

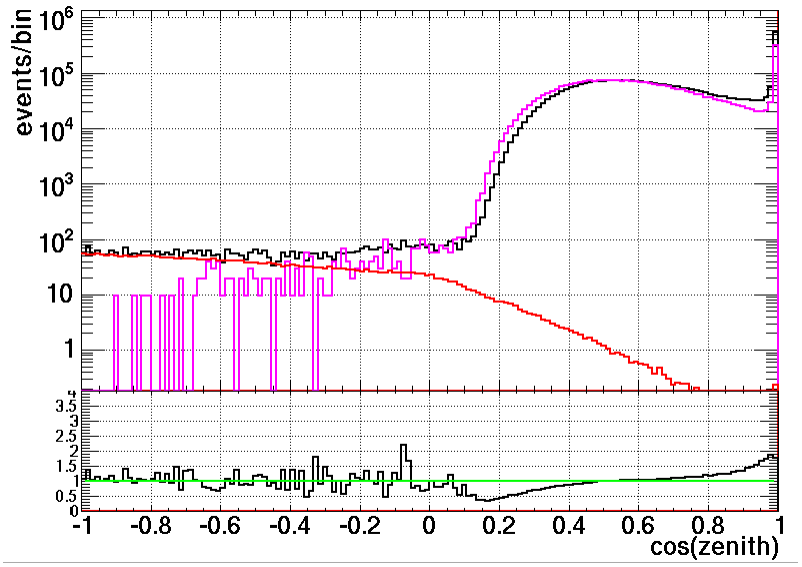

(b)

Figure 6.2: *Top:* Λ *distribution of upgoing tracks with* $\hat{\beta} < 1°$. *Bottom:* $\cos\theta$ *distribution of tracks with* $\Lambda > -5.2$ *and* $\hat{\beta} < 1°$. *Data are black, muons magenta and neutrinos red.*

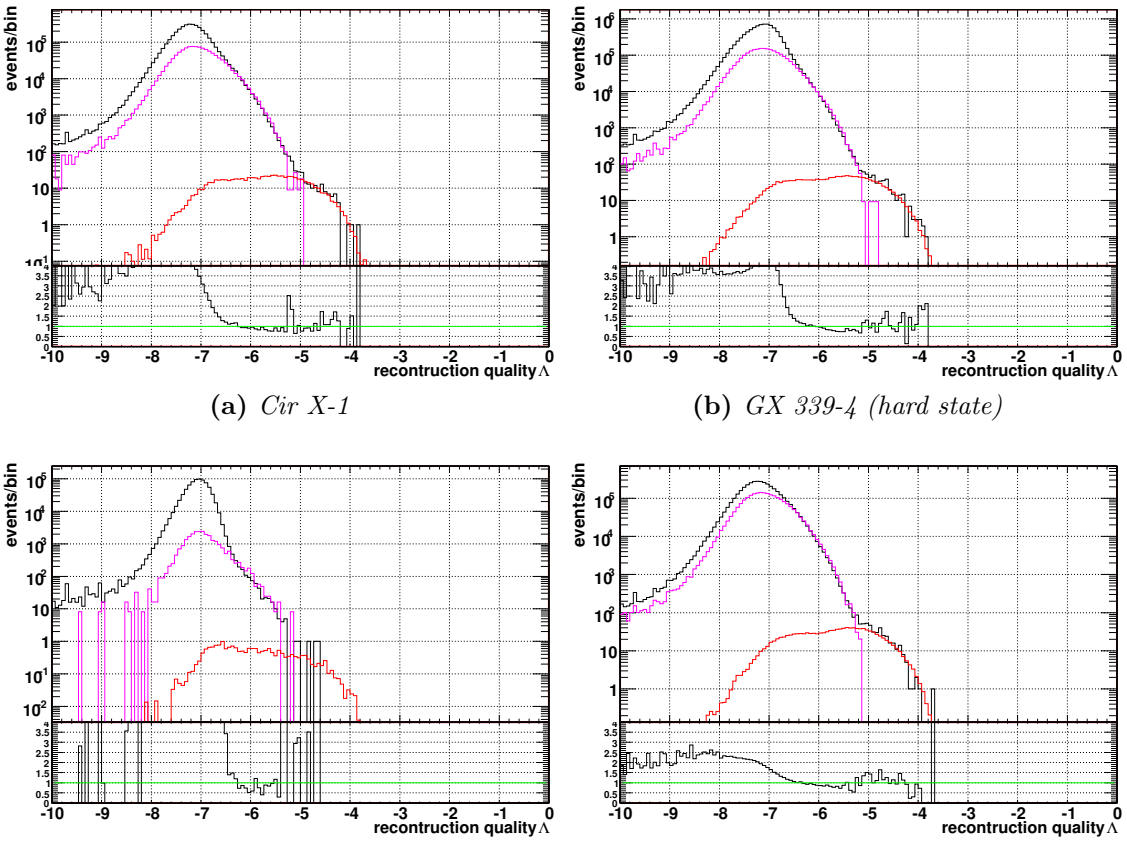

(a) *Cir X-1*

(b) *GX 339-4 (hard state)*

(c) *GX 339-4 (transition)*

(d) *H1743-322 (hard state)*

Figure 6.3: Λ *distributions for each neutrino search. Upgoing events with error estimate cut* $\hat{\beta} < 1°$. *Data are black, muons magenta and neutrinos red.*

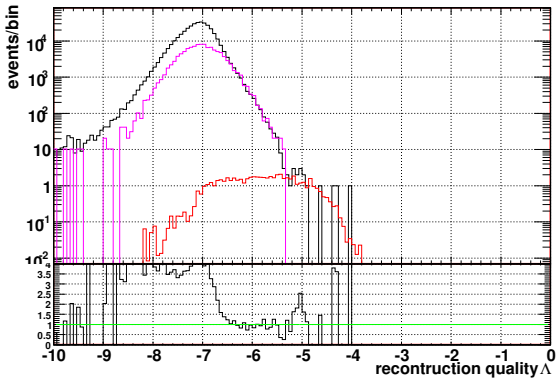

(e) *H1743-322 (transition)*

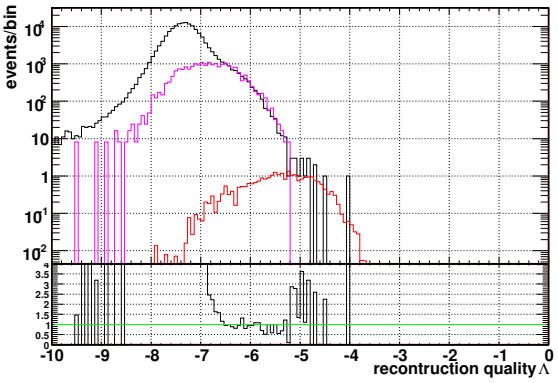

(f) *IGR J17091-3624*

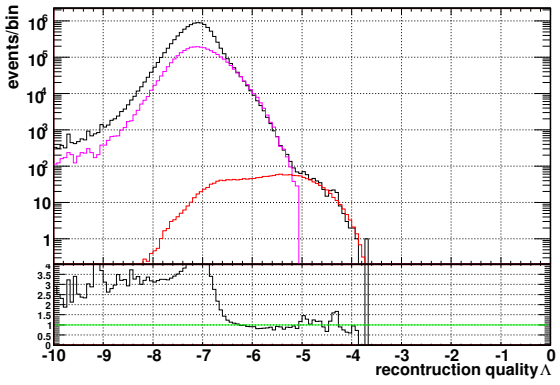

(g) *Cyg X-1 (hard state)*

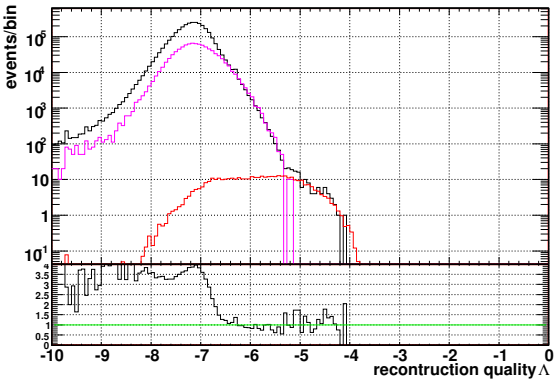

(h) *Cyg X-1 (transition)*

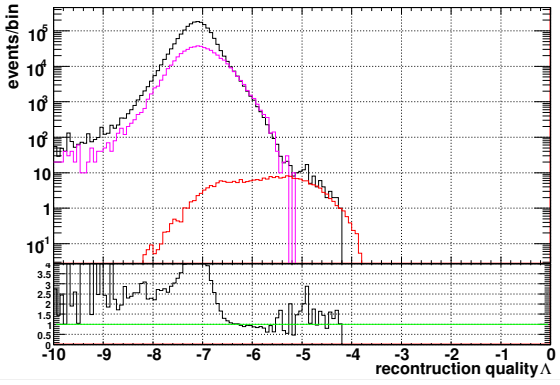

(i) *Cyg X-3*

Figure 6.3: Λ *distributions for each neutrino search. Upgoing events with error estimate cut* $\hat{\beta} < 1°$. *Data are black, muons magenta and neutrinos red. (cont.)*

Table 6.3: *Comparison between the number of selected events in data and Monte Carlo for each selected time window. The last column contains the ratio and its statistical error.*

source	Λ cut	N_{data}	$N_{\mu_{MC}}$	$N_{\nu_{MC}}$	N_{data}/N_{MC}
Cir X-1	-5.0	132	18.0	120.0	0.957±0.165
	-5.2	245	62.8	178.2	1.017±0.130
	-5.4	553	305.2	240.9	1.013±0.086
	-5.6	1553	1481.2	307.6	0.868±0.042
GX 339-4	-5.0	325	27.9	273.3	1.079±0.122
(hard state)	-5.2	506	93.0	399.9	1.027±0.091
	-5.4	1012	586.0	537.1	0.901±0.055
	-5.6	2736	2697.5	677.5	0.811±0.029
GX 339-4	-5.0	3	0.0	2.6	1.171±1.410
(transition)	-5.2	5	8.2	3.6	0.425±0.314
	-5.4	14	8.2	4.7	1.089±0.595
	-5.6	45	48.9	6.0	0.819±0.233
H1743-322	-5.0	273	0.0	233.3	1.170±0.147
(hard state)	-5.2	427	20.3	344.2	1.172±0.118
	-5.4	723	324.1	462.4	0.919±0.067
	-5.6	1748	1458.4	579.2	0.858±0.039
H1743-322	-5.0	7	0.0	8.4	0.836±0.605
(transition)	-5.2	15	0.0	12.5	1.201±0.650
	-5.4	21	10.3	17.2	0.763±0.312
	-5.6	79	72.0	23.0	0.832±0.179
IGR J17091-3624	-5.0	11	0.0	7.7	1.437±0.953
	-5.2	18	0.0	10.5	1.710±0.930
	-5.4	42	32.6	13.9	0.903±0.272
	-5.6	129	155.0	17.3	0.749±0.123
Cyg X-1	-5.0	414	0.0	354.2	1.169±0.120
(hard state)	-5.2	635	66.4	518.6	1.085±0.087
	-5.4	1256	635.9	692.0	0.946±0.052
	-5.6	3216	2828.4	866.4	0.870±0.029
Cyg X-1	-5.0	59	0.0	57.7	1.022±0.268
(transition)	-5.2	111	10.1	88.3	1.128±0.221
	-5.4	187	70.6	124.6	0.958±0.139
	-5.6	515	484.2	161.6	0.797±0.066
Cyg X-3	-5.0	66	0.0	42.2	1.563±0.433
	-5.2	95	10.0	62.6	1.308±0.288
	-5.4	151	60.0	86.2	1.033±0.169
	-5.6	335	250.1	108.4	0.935±0.100

6.3 Unbinned search method

The statistical method adopted to verify the presence of a point source of neutrinos among the candidate microquasars, or to set limits on their fluxes, is an unbinned likelihood method based on a likelihood ratio test (e.g. James, 2006, § 10). This is used to test the data against a hypothesis H_0, conventionally called the *null hypothesis*, or an alternative hypothesis H_1. In our case H_0 stands for: *"this outbursting microquasar is not a point source of neutrinos"*. Whereas the opposite applies to H_1. The test is performed by means of a variable, which can be any function of the data, called the *test statistic*, indicated as Q hereafter. The test statistic must have the property to assume different distributions in case H_0 or alternatively H_1 are true (see also Figure 6.4). If this condition is met, it is possible to define a region ω, called the *critical region*, so that if Q lies within ω the null hypothesis H_0 is rejected. The critical region can be adjusted in order to reach the desired level of significance α, which is the probability to reject H_0 if H_0 is true[2]:

$$P(Q \in \omega | H_0) \equiv \alpha \ . \tag{6.1}$$

This probability is set to 5.7×10^{-7} for a 5σ significance and 2.7×10^{-3} for a 3σ significance. In the same way one can define the *power* of the test as the probability to reject H_0 when H_1 is true:

$$P(Q \in \omega | H_1) \equiv power \ . \tag{6.2}$$

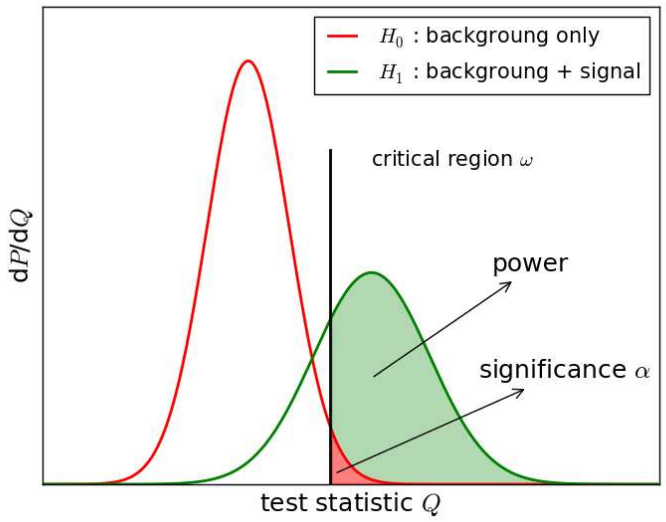

Figure 6.4: *Sketch of the main concepts of hypothesis testing. The test statistic has different distributions according to the model, H_0 or H_1, and can be used to discriminate between them. The significance α, which defines the test, is the probability to erroneously reject H_0. The* power *is the probability to correctly accept H_1.*

[2]This is also called an *error of the first kind* in textbooks.

Neyman and Pearson (Neyman et al., 1933) have demonstrated that if the two models H_0 and H_1 are completely specified, i.e. they have no unknown parameters, the test statistic with the greatest power is the likelihood ratio, whichever is the significance required. The likelihood ratio test statistic is defined as:

$$Q = -2 \log \frac{P(\text{data}|H_0)}{P(\text{data}|H_1)} \ . \tag{6.3}$$

If H_0 or H_1 are not completely specified, but depend on some unknown parameter, the maximized values of the likelihoods are used in Eq. 6.3. In our case the null hypothesis model corresponds to the flux of atmospheric neutrinos and misreconstructed atmospheric muons, which is fully defined from the data. The alternative model, that accounts for the background events plus the neutrinos coming from the hypothetical source, lacks the information on the intensity of the source, which translates in a number of signal events present in the data set. In this case the likelihood ratio is given by:

$$Q = -2 \log \frac{P(\text{data}|H_0)}{\max\{P(\text{data}|H_1)\}} \ , \tag{6.4}$$

where $\max\{P(\text{data}|H_1)\}$ is the likelihood of the data maximized w.r.t. the free parameters of the alternative model H_1.

Under the assumption that a point source emits neutrinos at a certain position in the sky and with a certain spectral shape, the log-likelihood as a function of the coordinates of the detected events can be written as (Heijboer, 2004):

$$\log(\mathcal{L}) = \sum_i \log[n_{sig}\mathcal{S}(\beta_i) + n_{tot}\mathcal{B}(\theta_i)] - n_{tot} \ , \tag{6.5}$$

where $\mathcal{S}$ is the point spread function (PSF, Figure 6.5), β is the angular distance from the source under study, $\mathcal{B}$ is the distribution of background events, here expressed in local coordinates, as a function of the zenith angle θ (Figure 6.6). The number of signal events n_{sig} is related to the intensity of the neutrino source, and is the quantity that we want to measure or put limits on. The sum iterates over the total number of events in the sky n_{tot}. In Eq. (6.5) $\mathcal{S}$ and $\mathcal{B}$ are normalized to 1. The quantities β_i and θ_i are linked to each other by the time of the event, this was not put explicitly in (6.5) to simplify the reading. The information on the assumed spectral index for the neutrino emission from the source is contained in the PSF, which is normally calculated assuming an energy dependence[3] of the neutrino flux as $\propto E_\nu^{-2}$.

The test statistic is defined as

$$Q = \max\{\log \mathcal{L}(n_{sig})\} - \log \mathcal{L}(n_{sig} = 0) \tag{6.6}$$

which represents the logarithm of the ratio between the likelihood maximized w.r.t. n_{sig} over the likelihood calculated in the background only hypothesis assuming $n_{sig} = 0$.

[3]Although in some cases the spectral index can be left free and fitted together with the flux intensity n_{sig}.

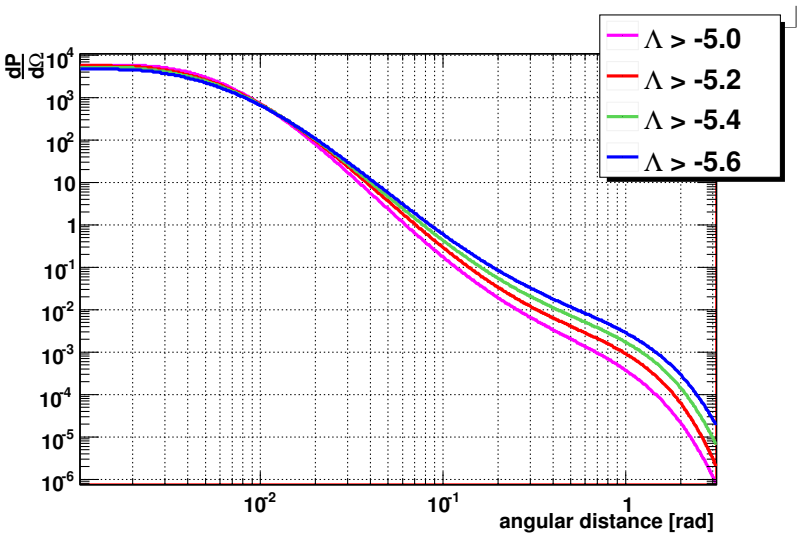

Figure 6.5: *Point spread functions calculated for a spectrum* $\propto E^{-2}$ *and for different values of the* Λ*-cut. Obtained from Monte Carlo. The curves in the plot are normalized to 1 over the whole solid angle and are used in the likelihood calculation (*$\mathcal{S}$ *in Eq. 6.5).*

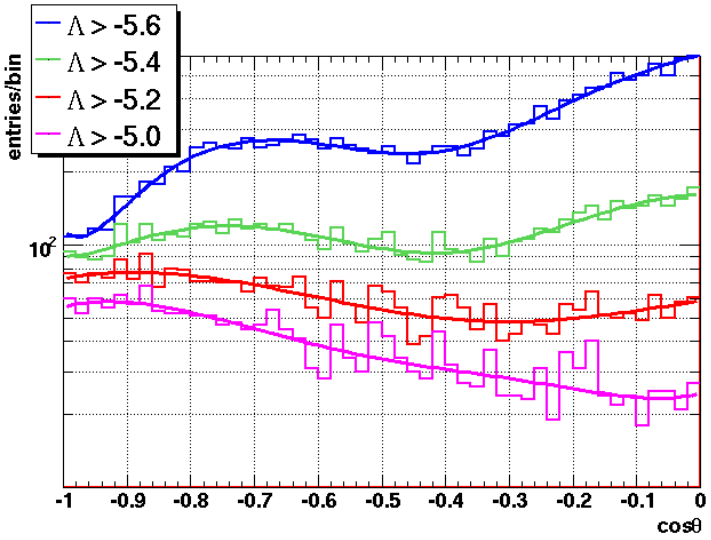

Figure 6.6: *The histograms represent the* $\cos\theta$ *distribution of the selected events in the data for different cuts on* Λ*. The smooth curves are suitable parameterizations and are used in the likelihood calculation (*$\mathcal{B}$ *in Eq. 6.5), as well as to generate random directions in pseudo-experiments (§ 6.3.1). The events with* $\cos\theta = -1$ *are upgoing, those with* $\cos\theta = 0$ *are horizontal.*

6.3.1 Pseudo-experiment generation

The distribution of the test statistic is calculated by means of a toy Monte-Carlo that was set up to generate a large number of pseudo-experiments. In this way, a large sample of possible background fluctuations is reproduced and the significance of the test statistic obtained from the data can be calculated. A pseudo-experiment consists of a set of neutrino events in equal number to those selected in the data for a specific neutrino search (see Table 6.2), but whose directions have been randomized. The randomization of neutrino directions is done as follows:

1. for each event in the data the $\cos\theta$ and ϕ are randomly generated according to the distribution in the data, using the parameterizations shown in Figure 6.6 and 6.7,

2. the time of the event is randomized within the start and stop time of the data run it belongs to,

3. the right ascension and declination are then calculated from the above.

To compute the distribution of the test statistic in the presence of one or more signals, up to 30 signal events were injected in the background only sky maps around the source under study, distributing them according to the PSF shown in Figure 6.5. A typical sky map is shown in Figure 6.8.

Since each signal event is generated in equatorial coordinates, in order to calculate the corresponding background flux in the likelihood (Eq. 6.5) it is necessary to assign them a zenith angle. The latter is randomly generated from the distribution of the zenith angle at which the source is seen by ANTARES. This depends on the source declination, two examples are shown in Figure 6.9.

For each pseudo-experiment, the likelihood in Eq. 6.5 is maximized w.r.t. n_{sig} in order to calculate the test statistic. The value of n_{sig} which maximizes the likelihood represents an estimate of the actual number of injected signals. Distributions of the fitted n_{sig} and the corresponding maximized Q-value are shown in Figure 6.10, in the background only and background plus signal cases. The fitter finds on average the right value of n_{sig} with an error of a few percent, meaning that all the normalizations were correctly taken into account in the likelihood method.

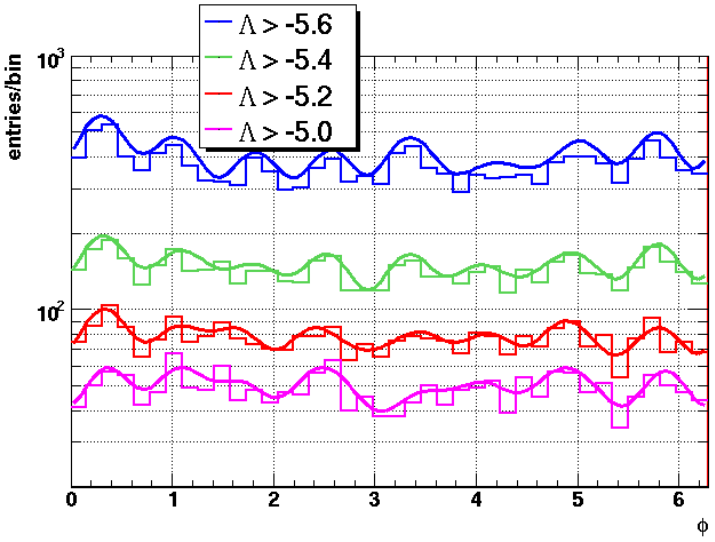

Figure 6.7: *The histograms represent the ϕ distribution of the selected events in the data for different cuts on Λ. The smooth curves are suitable parameterizations and are used to generate random directions in pseudo-experiments (§ 6.3.1).*

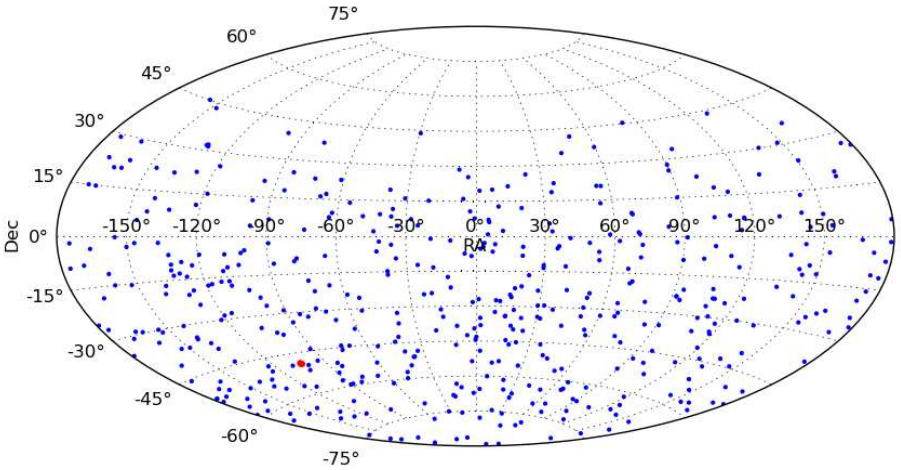

Figure 6.8: *Example of a sky map issued from a pseudo-experiment. The blue points come from the randomization of the ANTARES background, the red spot represents 3 signal events added around the coordinates of GX 339−4.*

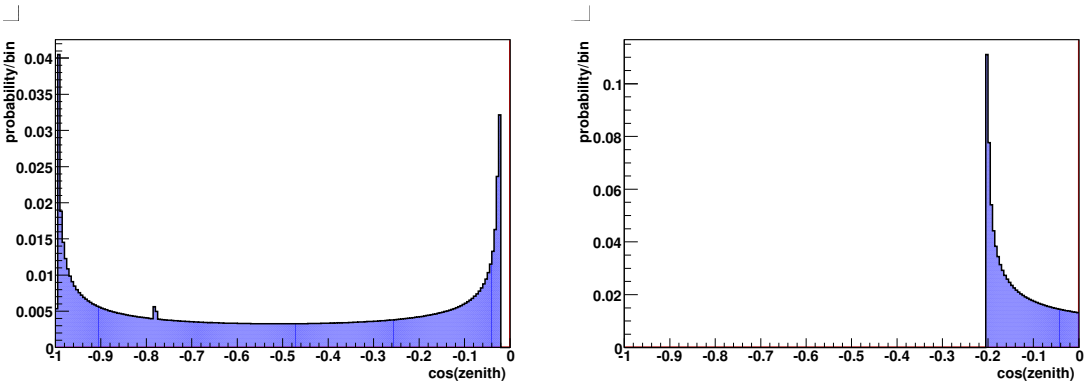

(a) *dec* $= -48.79°$ *(as for GX 339-4)* **(b)** *dec* $= 35.20°$ *(as for Cygnus X-1)*

Figure 6.9: *Distributions of* $\cos\theta$ *at which ANTARES observes two sources at two different declinations, over a time lapse of one day. These are used to randomly assign a zenith angle to injected signal events in pseudo experiment generation.*

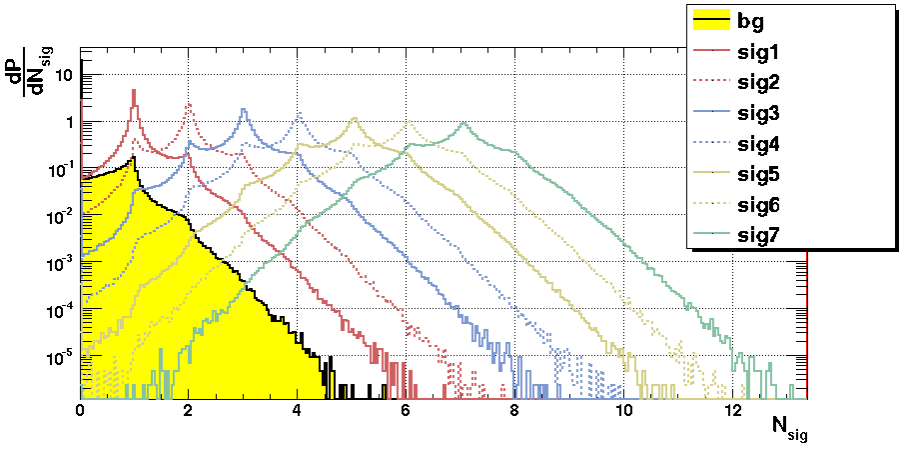

(a)

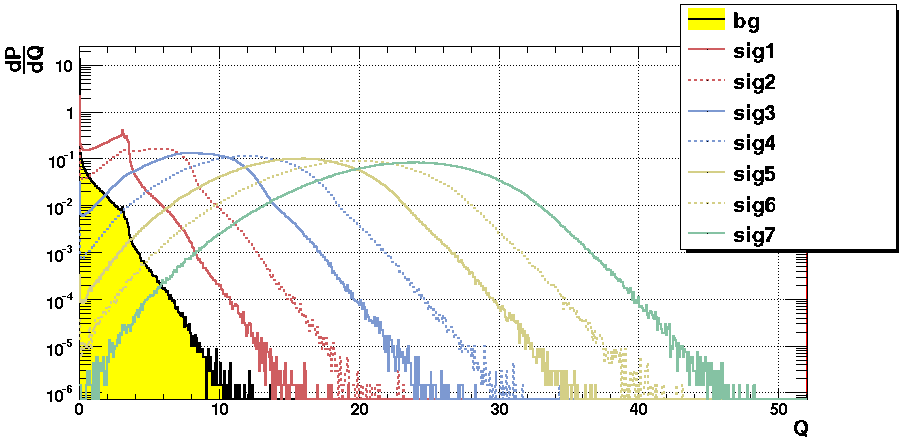

(b)

Figure 6.10: *Distributions of the fitted* n_{sig} *(a) and the corresponding maximized likelihood ratio Q (b) for background only PEs and with one or more injected signals (case of GX 339-4, dec=*$-48.79°$*).*

6.3.2 Neutrino flux calculation

In this work, microquasars are assumed to emit a flux of neutrinos that has the same energy dependence as the one obtained from the shock acceleration mechanism, and can be expressed as:

$$\frac{\mathrm{d}^3 N}{\mathrm{d}E\,\mathrm{d}S\,\mathrm{d}t} = \phi \cdot \left(\frac{E}{GeV}\right)^{-2} \mathrm{GeV}^{-1}\mathrm{cm}^{-2}\mathrm{s}^{-1} \ . \tag{6.7}$$

Once the energy dependence is fixed, the flux is completely defined by the normalization factor ϕ, which is the quantity that will be measured or on which limits will be put. The conversion between the number of detected signals n_{sig} and the flux normalization ϕ depends on the interplay of different quantities for each neutrino search, which are:

- the total observation time, which depends on the selected time window and the visibility factor,
- the source declination, which defines the distribution of the zenith angles at which the source is observed, and is important to account for the detector's effective area dependence on the zenith angle,
- the quality cut applied to select the events, since a looser cut will let more signal pass and thus increase the effective area w.r.t. a more stringent cut.

All these contributions are taken into account using the Monte Carlo simulations. The principle is to calculate the number of expected events for an arbitrarily chosen normalization ϕ, here set to $\phi_{-7} = 10^{-7}\mathrm{GeV}^{-1}\mathrm{cm}^{-2}\mathrm{s}^{-1}$, and then use a simple relation of proportionality to reverse the relation using the expression:

$$\phi = \frac{\phi_{-7}}{n_{sig,-7}} \times n_{sig} \ , \tag{6.8}$$

where $n_{sig,-7}$ is the mean number of signals expected from the Monte Carlo using the flux normalization ϕ_{-7}.

In practice, this is done by plotting the $\cos\theta$ of neutrino and anti-neutrino events with a weight:

$$W_{\nu,-7} = (2\pi)^{-1} \times (\Delta\Omega)^{-1} \times 0.5 \times 10^{-7} \times E_\nu^{-2} \times W_{generation} \tag{6.9}$$

where $(2\pi)^{-1}$ averages over the ϕ angle, $(\Delta\Omega)^{-1}$ is the inverse of the solid angle size of each bin in the histogram and accounts to remove the angular phase space factor from the weight, 0.5 accounts for the two components from neutrinos and anti-neutrinos and $W_{generation}$ is the generation weight in units GeV cm^{-2} s^{-1}. The histogram obtained is then convoluted with the distribution of $\cos\theta$ at which the source is observed by ANTARES, which depends on the source declination (Figure 6.9). The result is finally multiplied by the observation livetime. The contributions from the 5 line and the 9/10/12 lines configuration periods are calculated separately and the results are summed up at the end.

The acceptance for the 2007-2010 period is shown in Figure 6.11. The constants obtained with the same method for each neutrino search considered in this analysis are shown in Table 6.4, these values will be used in the following.

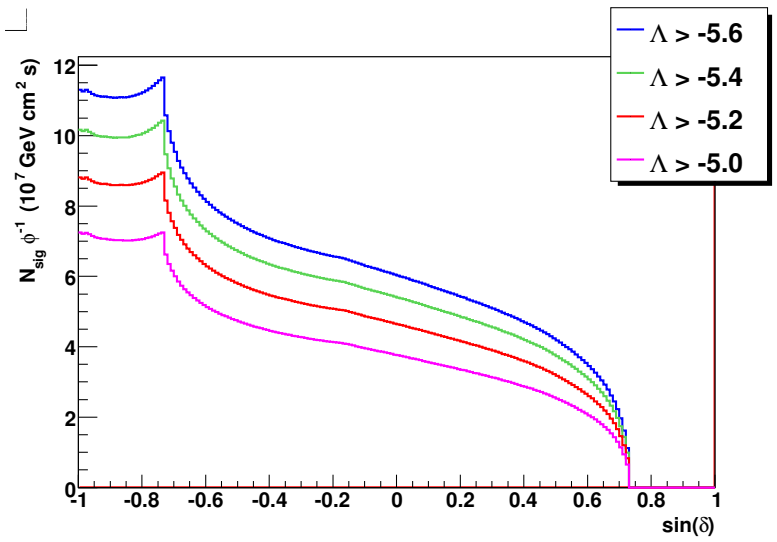

Figure 6.11: *Number of expected neutrino events from a source with flux* $10^{-7}\left(\frac{E}{GeV}\right)^{-2} GeV^{-1}\,cm^{-2}\,s^{-1}$ *during the 2007-2010 data taking as a function of the source declination. These values refer to time integrated neutrino search and will not be used in this analysis.*

Table 6.4: *Number of expected neutrino events from the selected sources and periods supposing a flux* $10^{-7}\left(\frac{E}{GeV}\right)^{-2} GeV^{-1}\,cm^{-2}\,s^{-1}$ *. These values will be used to calculate the flux normalizations according to the relation in Eq. 6.8.*

	$\Lambda > -5.0$	$\Lambda > -5.2$	$\Lambda > -5.4$	$\Lambda > -5.6$
Circinus X-1	0.69	0.85	0.98	1.09
GX 339-4 (HS)	1.17	1.45	1.68	1.88
GX 339-4 (TS)	0.023	0.029	0.034	0.038
H1743-322 (HS)	0.79	0.96	1.12	1.25
H1743-322 (TS)	0.042	0.051	0.059	0.066
IGR J17091-3624	0.037	0.046	0.053	0.059
Cygnus X-1 (HS)	1.64	2.07	2.44	2.75
Cygnus X-1 (TS)	0.35	0.44	0.53	0.59
Cygnus X-3	0.20	0.25	0.30	0.34

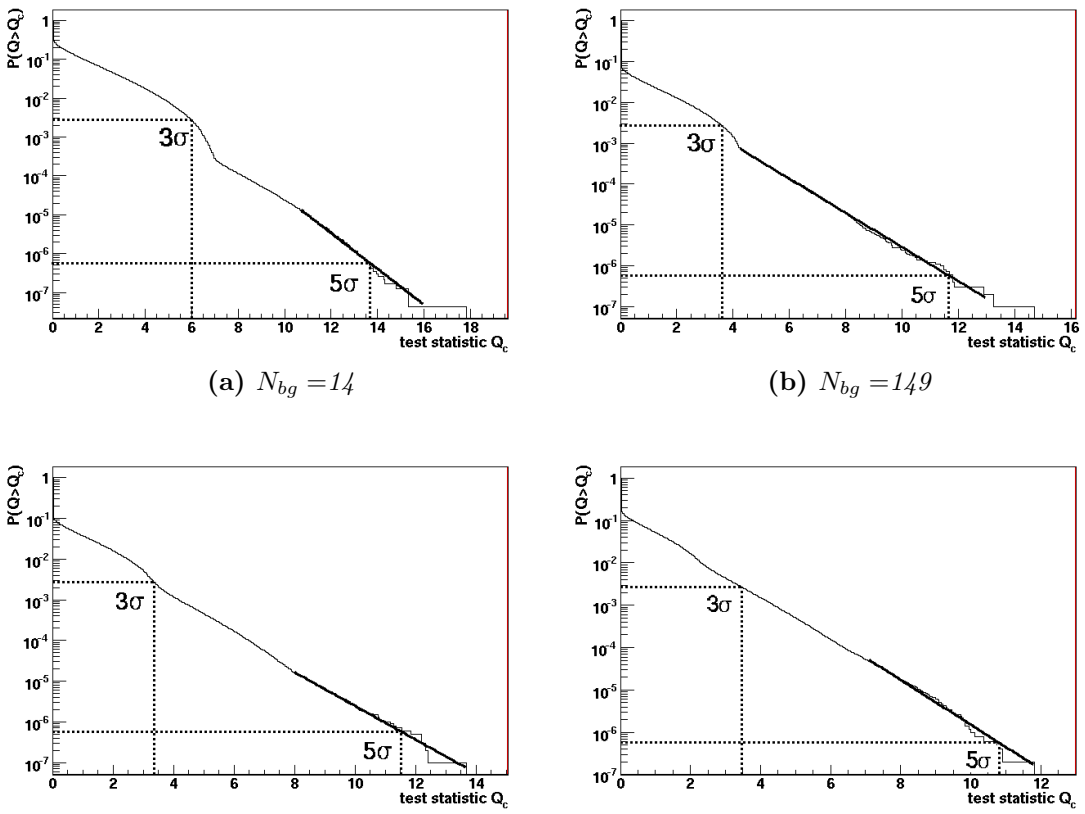

(a) N_{bg} =14

(b) N_{bg} =149

(c) N_{bg} =433

(d) N_{bg} =1254

Figure 6.12: *Background only cumulative distributions of the test statistic Q for different background events N_{bg} in the randomized sky maps. The solid straight line is an exponential fit to the tail of the distribution used to estimate the 5σ Q-value.*

6.3.3 Discovery potential and choice of the cut on Λ

The critical Q-value needed for a 5σ discovery or a 3σ evidence is calculated from the cumulative distribution of the test statistic in the background only case (the differential one being the yellow histogram in figure 6.10b). Some representatives of these distributions are shown in Figure 6.12, each with a different number of background events randomized in the sky map (cf. Table 6.2). From the plots in Figure 6.12 one can see that a little bump is present when the number of background events is small, feature that disappears as the number of events increases. This is due to the less relative importance of the background term in the likelihood in Eq. 6.5 when few events are present in the sky map, so that events generally look more signal like and have more chances to get a $Q > 0$. In these cases the correct asymptotic behavior at higher Q-values is restored when a high number of pseudo-experiments is generated. In the specific, a number pseudo-experiments of the order of $\sim 10^8$ has been generated in case of few background events. The corresponding $Q_c^{3\sigma}$ is obtained directly from the histogram, whilst an exponential fit is performed to the tail of the distribution in order to obtain the $Q_c^{5\sigma}$, due to the less statistic in this zone.

In order to calculate the flux needed to obtain a 5σ or 3σ critical Q-value, it is

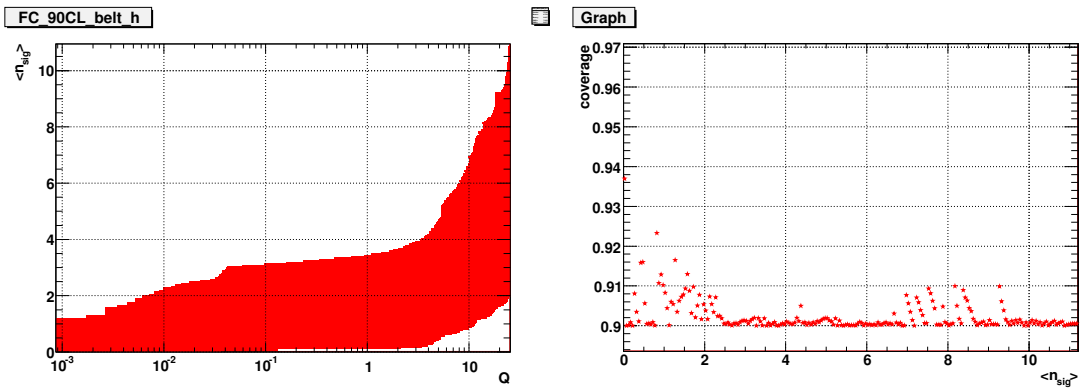

(a) (b)

Figure 6.13: *Feldman-Cousins 90%CL belt (a), note the Q in log scale, and coverage of the acceptance intervals (b). The coverage is stable up to 5σ levels.*

first necessary to compute the correspondent average number of signal events $\langle n_{sig} \rangle$ and then convert it using Eq. 6.8 and the constants in Table 6.4. The probability of getting a Q-value equal or higher than a certain critical value Q_c as a function of the average number of detected signals can be calculated using the probability distributions of Q, which are computed for a fixed n_{sig} as those in Figure 6.10b, and convoluting them with a Poissonian, as:

$$P(Q > Q_c|\langle n_{sig} \rangle) = \sum_{n_{sig}} P(Q > Q_c|n_{sig}) \frac{e^{-\langle n_{sig} \rangle} \langle n_{sig} \rangle^{n_{sig}}}{n_{sig}!} \ . \tag{6.10}$$

When estimating the average number of signals needed for a discovery or an evidence from equation (6.10), the $\langle n_{sig} \rangle$ corresponding to a probability of 0.5 is taken. The values obtained for the neutrino searches considered in this analysis are listed in Table 6.5 for different values of the cut on Λ. The final cuts to be used in the analysis are chosen in order to minimize the flux needed for a 5σ discovery, which is not the same for all the searches. In particular, a cut $\Lambda > -5.4$ is preferred in those cases where the observation livetime is less than a month or so. Whereas the cut $\Lambda > -5.2$ is applied in all other cases. The selected cuts are indicated with an arrow in Table 6.5, these will be used in the final search.

6.3.4 Limit setting method

The unified approach by Feldman and Cousins (Feldman et al., 1997) has been adopted to set upper limits on the neutrino flux normalization in the case no discovery is made. In Figure 6.13 is presented an example of the confidence belt together with the coverage obtained for each horizontal acceptance interval. This shows that the method has a proper behavior at low Q-values and a stable coverage up to the 5σ level and beyond.

Table 6.5: *Critical values of the test statistic, average number of signal events and relative flux normalizations needed for a 5σ or a 3σ deviation from the background only hypothesis. The average number of signal events, and thus the flux normalizations, are obtained considering a 50% probability for a discovery or evidence.*

source	Λ cut	$Q_{5\sigma}$	$\langle n_{sig}\rangle_{5\sigma}$	$\phi_{5\sigma}$	$Q_{3\sigma}$	$\langle n_{sig}\rangle_{3\sigma}$	$\phi_{3\sigma}$
Cir X-1	-5.0	12.80	3.40	4.700E-07	4.32	1.60	2.212E-07
→	-5.2	11.44	3.70	4.173E-07	3.56	1.60	1.804E-07
	-5.4	11.25	4.50	4.384E-07	3.27	2.00	1.949E-07
	-5.6	11.24	5.80	5.072E-07	3.33	2.60	2.274E-07
GX 339−4 (HS)	-5.0	11.77	3.65	3.112E-07	3.53	1.60	1.364E-07
→	-5.2	11.53	4.25	2.937E-07	3.37	1.85	1.278E-07
	-5.4	11.63	5.20	3.091E-07	3.38	2.30	1.367E-07
	-5.6	12.23	7.15	3.808E-07	3.51	3.10	1.651E-07
GX 339−4 (TS)	-5.0	14.12	2.10	8.852E-06	6.71	1.10	4.637E-06
	-5.2	13.88	2.45	8.335E-06	6.20	1.15	3.912E-06
→	-5.4	13.67	2.80	8.202E-06	6.00	1.45	4.248E-06
	-5.6	13.05	3.25	8.549E-06	4.96	1.60	4.209E-06
H1743−322 (HS)	-5.0	11.03	3.45	4.255E-07	3.50	1.55	1.912E-07
→	-5.2	11.15	4.05	4.081E-07	3.39	1.85	1.864E-07
	-5.4	11.49	4.80	4.174E-07	3.35	2.15	1.870E-07
	-5.6	11.20	5.90	4.601E-07	3.56	2.70	2.106E-07
H1743−322 (TS)	-5.0	14.02	2.50	5.370E-06	6.48	1.40	3.007E-06
	-5.2	13.39	2.80	4.914E-06	5.92	1.50	2.633E-06
→	-5.4	13.32	3.00	4.544E-06	5.62	1.55	2.348E-06
	-5.6	12.35	3.40	4.618E-06	4.72	1.70	2.309E-06
IGR J17091−3624	-5.0	13.86	2.40	6.539E-06	6.21	1.25	3.406E-06
	-5.2	13.33	2.65	5.874E-06	5.77	1.35	2.992E-06
→	-5.4	11.78	2.90	5.552E-06	5.06	1.55	2.967E-06
	-5.6	12.48	3.65	6.283E-06	4.37	1.70	2.926E-06
Cyg X-1 (HS)	-5.0	11.81	3.60	2.197E-07	3.66	1.60	9.765E-08
→	-5.2	11.60	4.40	2.128E-07	3.32	1.95	9.429E-08
	-5.4	10.81	5.50	2.257E-07	3.46	2.55	1.046E-07
	-5.6	11.36	8.40	3.068E-07	3.38	3.90	1.424E-07
Cyg X-1 (TS)	-5.0	12.96	2.84	8.067E-07	5.28	1.40	3.963E-07
	-5.2	12.83	3.30	7.412E-07	4.51	1.55	3.481E-07
→	-5.4	11.54	3.75	7.142E-07	3.59	1.65	3.143E-07
	-5.6	11.22	5.15	8.726E-07	3.25	2.25	3.812E-07
Cyg X-3	-5.0	12.89	2.85	1.443E-06	5.28	1.45	7.342E-07
	-5.2	12.78	3.30	1.316E-06	4.53	1.55	6.180E-07
→	-5.4	11.36	3.65	1.213E-06	3.62	1.60	5.319E-07
	-5.6	10.89	4.75	1.401E-06	3.17	2.15	6.340E-07

Systematic uncertainties

The limits have been calculated taking into account two sources of systematic uncertainties: one related to the angular resolution and the other related to the acceptance of the detector. The evaluation of systematics on the angular resolution has been conducted with a Monte Carlo study in which the detector performances have been degraded by smearing the hit times at the OM-level (Adrián-Martínez et al., 2011a). By varying the width of the time smearing from 0 to 3ns and checking the comparison with the data, it has been deduced a 1σ systematic uncertainty of 15% on the angular resolution, which is introduced in this analysis by smearing the direction in celestial coordinates of the signal events in pseudo-experiments. To constrain the systematic uncertainty on the acceptance, the atmospheric neutrino data have been compared to a simulation in which the efficiency of each OM is reduced. A 15% effect was observed, which is applied as the systematic uncertainty on the acceptance in the limit calculations. These systematic uncertainties take into account a broad variety of effects which may arise from possible timing offsets at the OM-level, mis-alignments of the detector units or inaccuracies in the light propagation model. A systematic uncertainty due to a rotation of the detector's reference frame is not accounted for in this procedure. The absolute pointing of the detector is known up to a level of 0.13° in azimuth and 0.06° in zenith (Halladjian, 2010). This effect is also taken into account by independently smearing the direction in local coordinates of signal events in pseudo-experiments. The effect of all the sistematic uncertainties considered here is to increase the sensitivity, i.e. the median 90% confidence level upper limit obtained in the background only case, by $\sim 10\%$.

6.4 Results of the data unblinding

The unblinded sky map of the 3058 neutrino events selected in the whole set of data, using a cut $\Lambda > -5.2$ and without applying any time cut, is shown in Figure 6.14, together with the positions in the sky of the microquasars considered in this analysis. When applying a cut $\Lambda > -5.4$, a total of 5709 neutrino candidates are selected.

Having applied the unbinned algorithm to the unblinded data for all of the 9 searches, no significant deviation from the background only hypothesis has been observed, as resumed in Table 6.6. For only one search was there an event close to a source within the time window; this was for the state transitions of H1743−322 (Figure 6.15). One neutrino event was detected during the 2009 outburst 2.3° away from the source, while the H1743−322 was about to transit from the hard to the soft state. Although the event is quite distant from the source, more than 4 times the angular resolution, the likelihood method has fitted a $n_{sig} = 0.66$, with a test statistic $Q = 0.41$. This is due to the low expected background, since only 27 events are present in the whole sky during this search. Background only pseudo experiments obtain an equal or higher value of the test statistic with a probability of 0.17 for this particular search, equivalent to a 1.36σ pre-trial effect. When taking into account the 9 trials, the probability that an equivalent or higher significance is issued by any of the searches is 0.80, thus the event is compatible with the background hypothesis.

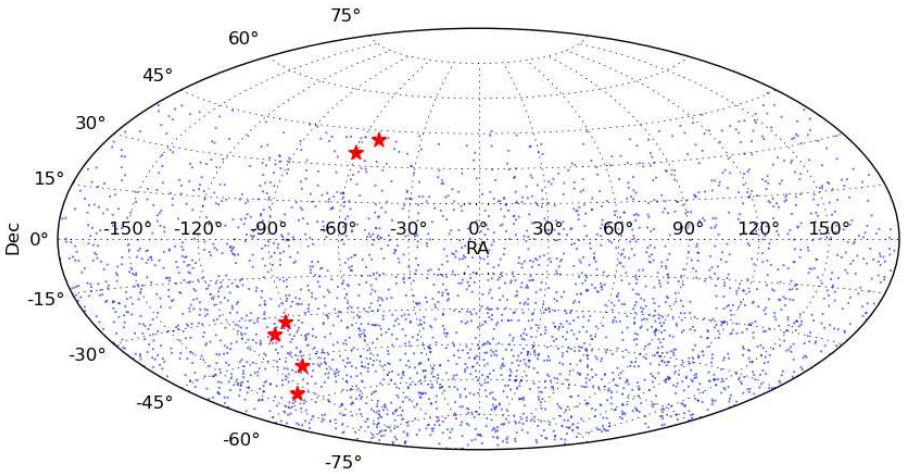

Figure 6.14: *Unblinded sky map of the 3058 neutrino candidates selected with the cut $\Lambda > -5.2$ in the whole ANTARES data taking period between 2007 and 2010 (813 days of live time). The red stars indicate the position of the microquasars considered in this analysis. For each neutrino search done with a cut $\Lambda > -5.2$ a sub-sample of these neutrinos is used. For searches where a cut $\Lambda > -5.4$ is applied, a total of 5709 candidate neutrino events are selected.*

Table 6.6: *Table resuming the results of the likelihood ratio algorithm for all the 9 searches. Together with the final test statistic value Q and number of fitted signal events n_{sig}, are shown the distance of the closest neutrino event and the number of background events expected within 3° from the source. HS and TS indicate the searches during hard states and transitional states, respectively.*

	Q	n_{sig}	closest ν	$N_{bg}^{exp}(< 3°)$
H1743−322(TS)	0.41	0.66	2.3°	0.04
Cyg X-1 (HS)	0.0016	0.08	1.4°	0.86
Cir X-1	0	0	5.7°	0.35
GX 339−4 (HS)	0	0	2.8°	0.66
GX 339−4 (TS)	0	0	11 °	0.02
H1743−322 (HS)	0	0	4.6°	0.61
IGR J17091−3624	0	0	12 °	0.05
Cyg X-1 (TS)	0	0	6.4°	0.27
Cyg X-3	0	0	6.9°	0.20

The 90% confidence level upper limits on the fluence, which is the energy per unit area, are shown in figure Figure 6.16. They have been calculated supposing a neutrino flux $\propto E_\nu^{-2}$ as

$$\mathcal{F}_\nu^{90\%\,CL} = \phi_\nu^{90\%CL} \Delta T_{search} \int_{10^2\ \mathrm{GeV}}^{10^8\ \mathrm{GeV}} E_\nu \cdot E_\nu^{-2}\, \mathrm{d}E_\nu \tag{6.11}$$

where $\phi_\nu^{90\%CL}$ is the upper limit on the neutrino flux normalization and ΔT_{search} the livetime of the search. The bounds of the integral correspond to the energy range of the Monte Carlo neutrino simulation used to calculate the PSF.

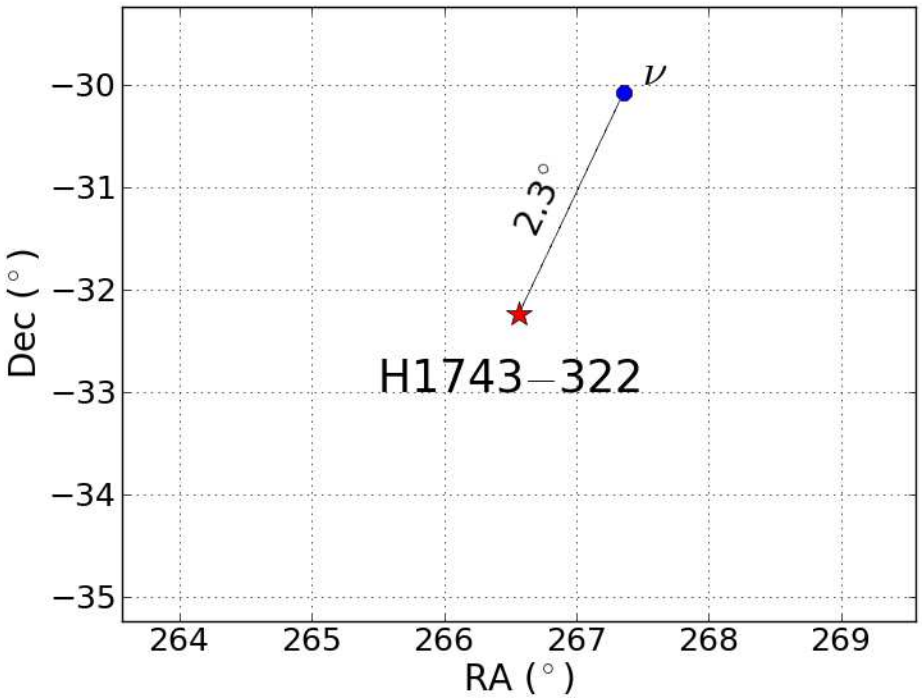

(a)

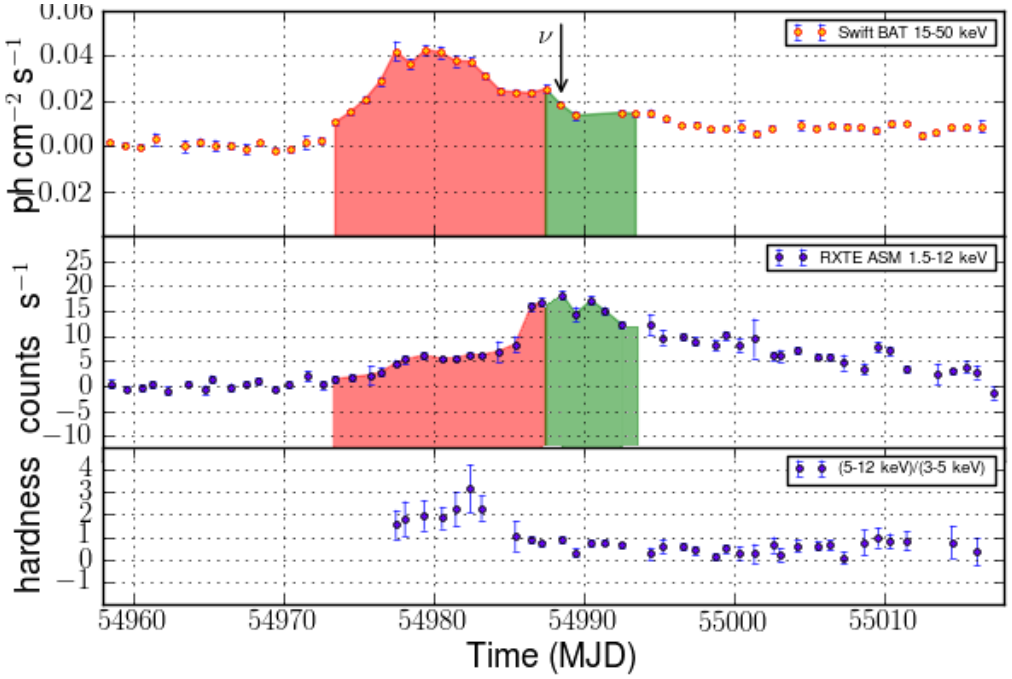

(b)

Figure 6.15: *Top: zoom of the neutrino sky map around H1743−322 (red star) relative to the search during state transitions. One neutrino event (blue dot) was detected 2.3 ° away from the source. Bottom: X-ray light curve of H1743−322 during the outburst in which the neutrino was detected. The arrow indicates the detection time. The red and green areas correspond to the hard and transitional state selection respectively.*

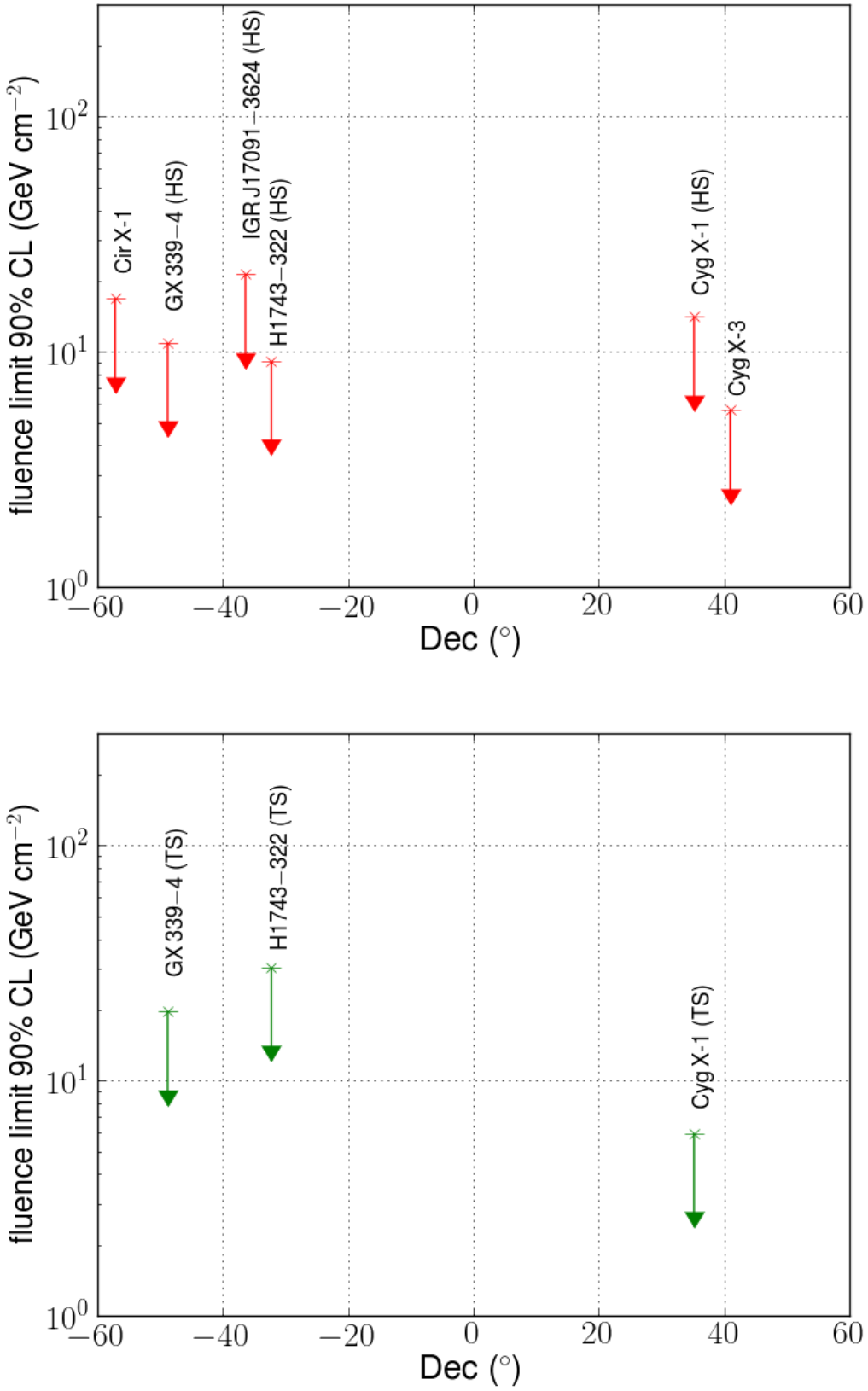

Figure 6.16: *Feldman-Cousins 90% confidence level upper limits on the neutrino fluence for a flux* $\propto E_\nu^{-2}$*. The upper plot refers to all the searches during the hard state plus those for Cir X-1 and Cyg X-3. The bottom plot refers to all the searches performed during the hard to soft transition.*

The limits on the fluences shown in Figure 6.16 can not be compared directly with the expectations of the model by Levinson et al. (2001) reported by Distefano et al. (2002) (c.f. §4.7.1), since the latter express the neutrino emission in terms of the energy flux f_ν, without associating it to a particular spectral shape. Moreover, the model predicts neutrino emission only up to 100 TeV, while the spectrum obtained from Monte Carlo simulations extends up to 10^8 GeV. In order to compare the neutrino flux predictions with the results just shown, it is necessary to make some more stringent hypothesis on the energy dependence of the neutrino flux to make it adhere to the model's scenario. The spectral shape that is chosen here to compare with the predictions of the model is the following:

$$\frac{\mathrm{d}N}{\mathrm{d}E_\nu} \propto E_\nu^{-2} \exp\left(-\frac{E_\nu}{10^5 \text{ GeV}}\right) , \tag{6.12}$$

with an exponential cutoff at 100 TeV, to take into account the limitation in the acceleration process included in the model. The change in the flux shape also influences the result of the limit on the flux normalization $\phi_\nu^{90\%CL}$, giving a value which is a factor ~ 2.1 higher than that obtained without cutoff. This has been estimated by calculating the $\phi_\nu^{90\%CL}$ considering a neutrino flux as that of Eq. 6.12 for the case of GX 339−4 during hard states and comparing it with the result obtained without cutoff.

The upper limit on the neutrino energy flux resulting from the spectrum in Eq. 6.12 is calculated as

$$f_\nu^{90\%CL} = 2.1\phi^{90\%CL} \int_{10^2 \text{ GeV}}^{10^8 \text{ GeV}} E_\nu \cdot E_\nu^{-2} \exp\left(-\frac{E_\nu}{10^5 \text{ GeV}}\right) \mathrm{d}E_\nu \tag{6.13}$$

where the factor 2.1 accounts for the limit increase when introducing the cutoff. The results obtained under these new hypotheses, compared with the predictions by Distefano et al. (2002) are shown in Figure 6.17. The upper limit on the fluence is just given by multiplying Eq. 6.13 by the livetime of the observation.

The prediction of f_ν for the source H1743−322, which is not given in Distefano et al. (2002), has been calculated using the near-infrared observation by Baba et al. (2003) during the 2003 outburst. They detected a magnitude 13.6 in the 2MASS K_s-band, corresponding to a flux density of 2.4 mJy at a frequency of 1.4×10^{14} Hz, which allows the calculation of the model expectation of the energy flux f_ν using Eq. 8 in Distefano et al. (2002). The prediction for IGR J17091−3624 is not given in the paper, nor measurements were found to estimate it, for which reason the point is not included in Figure 6.17.

In the cases of GX 339−4 and Cyg X-3 the limit set is very close to the expectation, though not yet sufficient to start constraining the parameters of the model. To estimate the time needed by ANTARES to constrain the model, it can be supposed that the limit set decreases linearly with the observation livetime. This approximation can be considered valid since the product between the limit obtained and the corresponding observation livetime averaged among all the neutrino searches in this analysis is: $\langle f_\nu^{90\%CL} \times \Delta T_{search} \rangle = (2.72 \pm 1.39) \times 10^{-7}$ erg cm^{-2} s^{-1} day. Using this relation to estimate the time evolution of the limit set, one obtains that ∼20 days

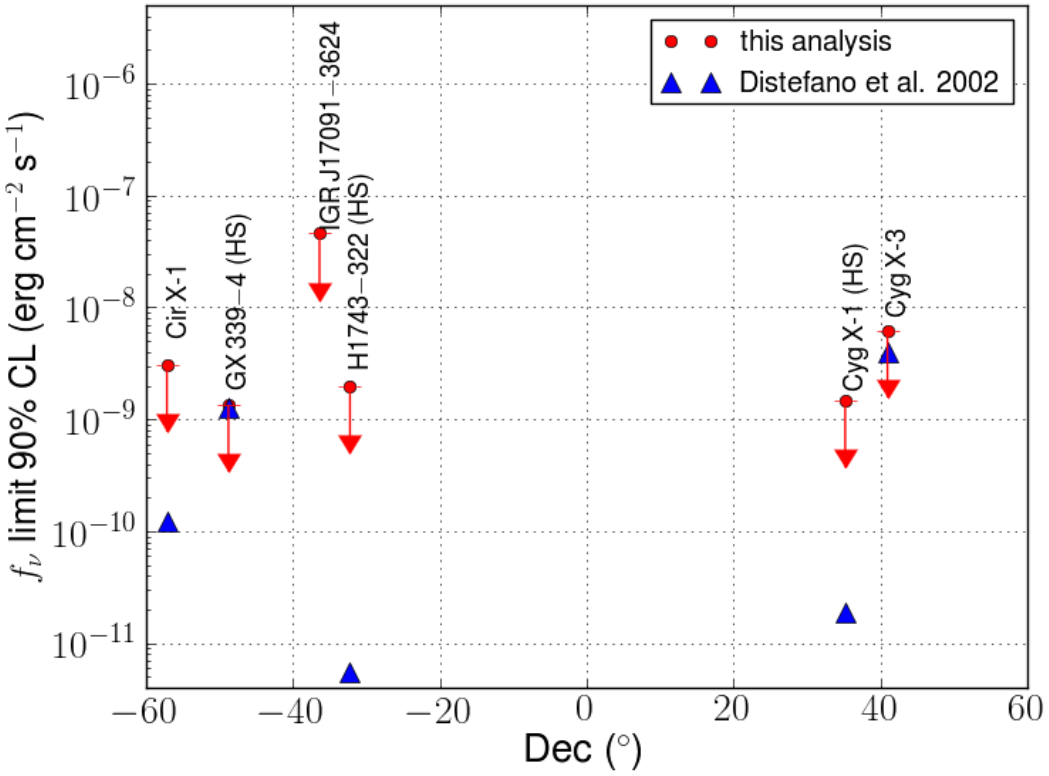

Figure 6.17: *Feldman-Cousins 90% confidence level upper limits on the energy flux in neutrinos f_ν obtained from this analysis, considering a flux $\propto E^{-2}\exp(-E_\nu/100$ TeV), compared with the expectations from Distefano et al. (2002). The model expectation for IGR J17091−3624 is not included in the plot since no infrared measurements were found to calculate it.*

more of livetime would be sufficient to start constraining the model for GX 339−4 and Cyg X-3. Moreover, the data that will be collected from 2011 to 2016, when ANTARES is foreseen to end its operation, will allow an improvement of all the limits by more than a factor 2.

6.5 Sensitivity expectations for KM3NeT

The result that has been obtained by analyzing ANTARES data can be used to extrapolate the future sensitivity of KM3NeT (§ 2.3.7) to microquasars, when performing a time dependent neutrino search during outbursts. This calculation needs to take into account the increased effective area of the KM3NeT detector with respect to ANTARES, which can be approximated as being greater by roughly a factor of 50. This will result in a proportionally increased number of detected neutrinos, both background and signal. To make a realistic extrapolation as a function of the operation time of the detector, it is necessary to take into account the efficiency in the data taking, i.e. the ratio between the effective livetime of the collected data and the time the detector is actually operated. This has been considered as being 65%,

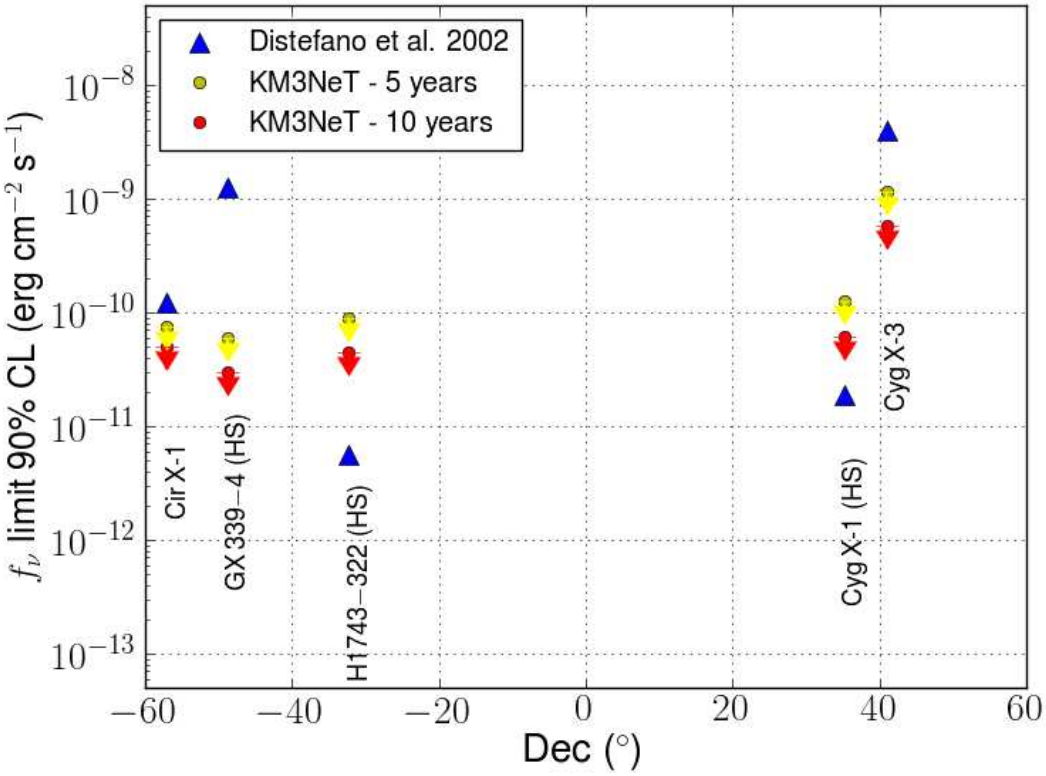

Figure 6.18: *Expected sensitivity (Feldman-Cousins 90% confidence level) on the energy flux in neutrinos f_ν for the KM3NeT detector after a 5-years and a 10-years operation time. The limits have been obtained considering a flux $\propto E^{-2}\exp(-E_\nu/100\ \mathrm{TeV})$ and are compared with the expectations from Distefano et al. (2002).*

as for the ANTARES data set used in this thesis. Also, the fraction of outbursting livetime has been accounted for, for each microquasar, on the basis of what was obtained in this analysis. The same pseudo experiment generation scheme described in § 6.3.1 has been adapted to the case of KM3NeT, considering operation times of 5 and 10 years. The resulting sensitivities on the energy flux in neutrinos f_ν for the microquasars studied in this analysis are shown in Figure 6.18 and compared with the predictions by Distefano et al. (2002). For the systems Cir X-1, GX 339−4 and Cyg X-3 the KM3NeT detector will allow, in the worst hypothesis, a deep constraining of the parameters characterizing the model by Levinson et al. (2001) or, if the predictions are correct, a discovery within the end of its operations.

Summary and conclusions

The detection of astrophysical sources of high energy neutrinos may shed light on the longstanding problem concerning the production sites and acceleration mechanisms of cosmic rays. The search for such sources is naturally oriented towards those astrophysical objects in which high energy processes are observed to take place.

In order to explore the neutrino sky, the ANTARES collaboration has built and is currently operating an underwater neutrino telescope in the Mediterranean Sea. The detector was completed in 2008 with its full configuration with 12 detection lines, whereas physics data taking started earlier in 2007 when the detector was composed of only 5 lines.

This thesis presented a search for neutrino emission from microquasars with the ANTARES telescope. Microquasars are galactic binary systems in which a compact object, i.e. a black hole or a neutron star, accretes mass from a companion star. The accretion flow of matter is responsible for the thermal (soft) X-ray emission, whereas the synchrotron radiation emitted by the relativistic electrons in the jets is observed by ground based radio telescopes. In the hypothesis that a population of hadrons is also accelerated in the jets together with the electrons, neutrinos could be produced by their interaction with the dense radiation field in the acceleration region. The target photons may be provided by the synchrotron radiation originated in the jet itself or by the thermal X-rays produced in the disc.

The search for neutrinos from microquasars was conducted in this work with a multi-messenger approach. In microquasars harbouring a black hole, the X-ray and radio bands follow a correlated pattern during outbursts. More specifically, a mildly relativistic steady jet is observed during hard X-ray states, a major ejection is observed during transitions from a hard to a soft X-ray state, whereas the jet is not observed during the soft state. This scheme was applied using the data from the X-ray monitors RXTE/ASM and Swift/BAT to define the periods in which the black hole microquasars were supposed to accelerate a relativistic jet. In the case of a neutron star microquasar a custom time selection was applied. In another case, the data from the gamma ray telescope Fermi/LAT were used to define the outbursting periods. A total of 6 microquasars were selected for the analysis. For 3 black hole microquasars among the selected ones, the search for neutrinos was split between the hard state and the state transition periods.

The analysis was applied to the data collected by ANTARES between 2007 and 2010. The criteria to set a discovery or an evidence were defined using an unbinned method based on a likelihood ratio test. The quality cuts for the event selection in the data were optimized in order to minimize the flux needed for a discovery. Among the neutrino searches on nine microquasars, none has brought a significant deviation

from the background expectations. The most significant search was that concerning H1743−322 during state transitions, which obtained a post-trial p-value of 80%. The upper limits to the fluences were calculated supposing a neutrino spectrum $\propto E_\nu^{-2}$. To compare with the model expectations from Distefano et al. (2002), a neutrino flux was assumed with an exponential cutoff at 100 TeV. The model could not be constrained for any of the searches, though the upper limits obtained on the energy flux in neutrinos were very close to the model expectations in the cases of GX 339−4 (hard state) and Cyg X-3. ANTARES will be able to constrain the model for these sources with a future analysis that will include more data (and outbursts). Moreover, the data that will be collected until the foreseen end of ANTARES operations in 2016 will allow an improvement of the limits set by this analysis by more than a factor 2.

Finally, the future construction and operation of KM3NeT, the km^3 neutrino telescope foreseen to be built in the Mediterranean Sea, will significantly improve the sensitivity on the neutrino sky that is now observed by ANTARES.

Bibliography

Abdo, A. A. et al. (2009a). "Detection of 16 Gamma-Ray Pulsars Through Blind Frequency Searches Using the Fermi LAT". In: *Science* 325, pp. 840– (cit. on p. 96).

— (Nov. 2009b). "Fermi/LAT observations of LS 5039". In: ApJ 706, pp. L56–L61 (cit. on p. 73).

— (Aug. 2009c). "Fermi LAT Observations of LS I +61°303: First Detection of an Orbital Modulation in GeV Gamma Rays". In: ApJ 701, pp. L123–L128 (cit. on p. 73).

— (2009d). "Modulated High-Energy Gamma-Ray Emission from the Microquasar Cygnus X-3". In: *Science* 326, pp. 1512– (cit. on p. 73).

— (2010). "Fermi Large Area Telescope First Source Catalog". In: ApJS 188, pp. 405–436 (cit. on p. 96).

— (June 2011). "Observations of the Young Supernova Remnant RX J1713.7−3946 with the Fermi Large Area Telescope". In: ApJ 734, 28, p. 28 (cit. on p. 11).

Abraham, J. et al. (Aug. 2008). "Observation of the Suppression of the Flux of Cosmic Rays above 4×10^{19}eV". In: *Physical Review Letters* 101.6, 061101, p. 061101 (cit. on p. 6).

Abreu, P. et al. (Dec. 2010). "Update on the correlation of the highest energy cosmic rays with nearby extragalactic matter". In: *Astroparticle Physics* 34, pp. 314–326 (cit. on p. 7).

Adrián-Martínez, S. et al. (Dec. 2011a). "First Search for Point Sources of High-energy Cosmic Neutrinos with the ANTARES Neutrino Telescope". In: ApJ 743, L14, p. L14 (cit. on pp. 30, 31, 118).

— (Oct. 2011b). "Measurement of the Group Velocity of Light in Sea Water at the ANTARES Site". In: *ArXiv e-prints* (cit. on p. 18).

— (Nov. 2011c). "Search for Neutrino Emission from Gamma-Ray Flaring Blazars with the ANTARES Telescope". In: *ArXiv e-prints* (cit. on pp. 30, 32).

Ageron, M. et al. (Mar. 2012). "The ANTARES telescope neutrino alert system". In: *Astroparticle Physics* 35, pp. 530–536 (cit. on p. 57).

Aggouras, G. et al. (Nov. 2006). "Recent results from NESTOR". In: *Nuclear Instruments and Methods in Physics Research A* 567, pp. 452–456 (cit. on p. 33).

Agrawal, V. et al. (Feb. 1996). "Atmospheric neutrino flux above 1 GeV". In: Phys. Rev. D 53, pp. 1314–1323 (cit. on p. 38).

Aguilar, J. A. et al. (Apr. 2011a). "A fast algorithm for muon track reconstruction and its application to the ANTARES neutrino telescope". In: *Astroparticle Physics* 34, pp. 652–662 (cit. on pp. 47, 52).

Aguilar, J. A. et al. (Jan. 2011b). "Search for a diffuse flux of high-energy ν_μ with the ANTARES neutrino telescope". In: *Physics Letters B* 696, pp. 16–22 (cit. on pp. 30, 32).

Aharonian, F. et al. (2005). "Discovery of Very High Energy Gamma Rays Associated with an X-ray Binary". In: *Science* 309, pp. 746–749 (cit. on p. 73).

— (Apr. 2006). "A detailed spectral and morphological study of the gamma-ray supernova remnant ¡ASTROBJ¿RX J1713.7-3946¡/ASTROBJ¿ with HESS". In: A&A 449, pp. 223–242 (cit. on p. 11).

Albert, J. et al. (June 2006). "Variable Very-High-Energy Gamma-Ray Emission from the Microquasar LS I +61 303". In: *Science* 312, pp. 1771–1773 (cit. on p. 73).

— (Nov. 2007a). "Observation of VHE γ-rays from Cassiopeia A with the MAGIC telescope". In: A&A 474, pp. 937–940 (cit. on p. 11).

— (2007b). "Very High Energy Gamma-Ray Radiation from the Stellar Mass Black Hole Binary Cygnus X-1". In: ApJ 665, pp. L51–L54 (cit. on p. 73).

Aleksić, J. et al. (Sept. 2010). "Magic Constraints on γ-ray Emission from Cygnus X-3". In: ApJ 721, pp. 843–855 (cit. on p. 73).

ANTARES Collaboration, M. Ageron, et al. (2011). "ANTARES: the first undersea neutrino telescope". In: *Nucl. Instrum. Meth.* A656, pp. 11–38 (cit. on p. 22).

ANTARES Collaboration, J. A. Aguilar, et al. (2005). "Transmission of light in deep sea water at the site of the ANTARES neutrino telescope". In: *Astroparticle Physics* 23, pp. 131–155 (cit. on p. 18).

Antonioli, P. et al. (Oct. 1997). "A three-dimensional code for muon propagation through the rock: MUSIC". In: *Astroparticle Physics* 7, pp. 357–368 (cit. on p. 39).

Auger, P. et al. (1939). "Extensive Cosmic-Ray Showers". In: *Reviews of Modern Physics* 11, pp. 288–291 (cit. on p. 3).

Aynutdinov, V. et al. (Apr. 2009). "The BAIKAL neutrino experiment - Physics results and perspectives". In: *Nuclear Instruments and Methods in Physics Research A* 602, pp. 14–20 (cit. on p. 20).

Baba, D. and T. Nagata (Apr. 2003). "IGR J17464-3213 = XTE J17464-3213". In: IAU Circ. 8112 (cit. on p. 122).

Bailey, D. J. L. (2004). "Monte Carlo tools and analysis methods for understanding the ANTARES experiment and predicting its sensitivity to dark matter." PhD thesis. University of Oxford (cit. on pp. 37, 39).

Balbus, S. A. and J. F. Hawley (July 1991). "A powerful local shear instability in weakly magnetized disks. I - Linear analysis. II - Nonlinear evolution". In: *ApJ* 376, pp. 214–233 (cit. on p. 64).

— (Jan. 1998). "Instability, turbulence, and enhanced transport in accretion disks". In: *Reviews of Modern Physics* 70, pp. 1–53 (cit. on p. 64).

Barr, G. D. (1987). "The Separation of Signals and Background in a Nucleon Decay Experiment." PhD thesis. University of Oxford (cit. on p. 37).

Becherini, Y. et al. (Feb. 2006). "A parameterisation of single and multiple muons in the deep water or ice". In: *Astroparticle Physics* 25, pp. 1–13 (cit. on p. 39).

Becker, J. K. (2008). "High-energy neutrinos in the context of multimessenger astrophysics". In: *Phys. Rep.* 458, pp. 173–246 (cit. on p. 10).

Bednarek, W., G. F. Burgio, and T. Montaruli (2005). "Galactic discrete sources of high energy neutrinos". In: *New Astron. Rev.* 49, pp. 1–21 (cit. on p. 10).

Belloni, T., S. Motta, and T. Muñoz-Darias (2010). *ATel 2577* (cit. on p. 89).

Bergman, D. R. and The High Resolution Fly's Eye Collaboration (Mar. 2007). "Observation of the GZK Cutoff Using the HiRes Detector". In: *Nuclear Physics B Proceedings Supplements* 165, pp. 19–26 (cit. on p. 6).

Blümer, J., R. Engel, and J. R. Hörandel (Oct. 2009). "Cosmic rays from the knee to the highest energies". In: *Progress in Particle and Nuclear Physics* 63, pp. 293–338 (cit. on p. 5).

Bosch-Ramon, V., J. M. Paredes, and G. E. Romero (2006). "Leptonic emission from microquasar jets: from radio to very high-energy gamma-rays". In: *Populations of High Energy Sources in Galaxies*. Ed. by E. J. A. Meurs & G. Fabbiano. Vol. 230. IAU Symposium, pp. 91–92 (cit. on p. 74).

Bosch-Ramon, V., G. E. Romero, and J. M. Paredes (Feb. 2006). "A broadband leptonic model for gamma-ray emitting microquasars". In: A&A 447, pp. 263–276 (cit. on p. 74).

Bossard, G. et al. (Mar. 2001). "Cosmic ray air shower characteristics in the framework of the parton-based Gribov-Regge model NEXUS". In: Phys. Rev. D 63.5, 054030, p. 054030 (cit. on p. 39).

Bowyer, S. et al. (1965). "Cosmic X-ray Sources". In: *Science* 147, pp. 394–398 (cit. on p. 92).

Bradt, H. L. and B. Peters (Dec. 1948). "Investigation of the Primary Cosmic Radiation with Nuclear Photographic Emulsions". In: *Physical Review* 74, pp. 1828–1837 (cit. on p. 3).

Calvelo, D. E. et al. (Jan. 2012). "Millimetre observations of a sub-arcsecond jet from Circinus X-1". In: MNRAS 419, pp. L54–L58. URL: http://adsabs.harvard.edu/abs/2012MNRAS.419L..54C (cit. on p. 85).

Capitanio, F. et al. (July 2010). "A Failed outburst of H1743-322". In: *X-ray Astronomy 2009; Present Status, Multi-Wavelength Approach and Future Perspectives* 1248, pp. 149–150 (cit. on p. 91).

Cassinelli, J. P. (1979). "Stellar winds". In: *ARA&A* 17, pp. 275–308 (cit. on p. 62).

Chen, Y. P. et al. (2010). "The 2009 outburst of H 1743-322 as observed by RXTE". In: *AAP* 522, A99+ (cit. on p. 92).

Cooper-Sarkar, A. (2010). "Proton Structure from HERA to LHC". In: *ArXiv e-prints* (cit. on pp. 14, 15).

Cooper-Sarkar, A., P. Mertsch, and S. Sarkar (2011). "The high energy neutrino cross-section in the Standard Model and its uncertainty". In: *ArXiv e-prints* (cit. on p. 15).

Corbel, S., R. P. Fender, et al. (2000). "Coupling of the X-ray and radio emission in the black hole candidate and compact jet source GX 339-4". In: A&A 359, pp. 251–268 (cit. on p. 71).

Corbel, S., P. Kaaret, et al. (Oct. 2005). "Discovery of X-Ray Jets in the Microquasar H1743-322". In: ApJ 632, pp. 504–513 (cit. on p. 91).

Corbel, S., T. Tzioumis, et al. (2007). *ATel 1007* (cit. on p. 89).

Corbel, S., T. Tzioumis, et al. (Oct. 2008). "Renewed radio activity from H1743-322 observed with the ATCA". In: *The Astronomer's Telegram* 1766, p. 1 (cit. on p. 91).

de Jong, M. (2009). *ANTARES-SOFT-2009-001, ANTARES internal note* (cit. on p. 42).

Dickey, J. M. (Oct. 1983). "A new distance to Cygnus X-3". In: ApJ 273, pp. L71–L73 (cit. on p. 95).

Distefano, C. et al. (Aug. 2002). "Neutrino Flux Predictions for Known Galactic Microquasars". In: ApJ 575, pp. 378–383 (cit. on pp. 74, 122–124, 128).

Esin, A. A., J. E. McClintock, and R. Narayan (1998). "Advection-dominated accretion model of X-ray Nova Muscae in outburst." In: *Eighteenth Texas Symposium on Relativistic Astrophysics*. Ed. by A. V. Olinto, J. A. Frieman, & D. N. Schramm, pp. 741–743 (cit. on p. 70).

Feldman, Gary J and Robert D Cousins (1997). "A Unified Approach to the Classical Statistical Analysis of Small Signals". In: *Physical Review D* 57.7, p. 40. URL: http://arxiv.org/abs/physics/9711021 (cit. on p. 116).

Fender, R. (2002). "Relativistic Outflows from X-ray Binaries ('Microquasars')". In: *Relativistic Flows in Astrophysics*. Ed. by A. W. Guthmann, M. Georganopoulos, A. Marcowith, & K. Manolakou. Vol. 589. Lecture Notes in Physics, Berlin Springer Verlag, p. 101 (cit. on p. 73).

Fender, R. P. (Apr. 2003). "Uses and limitations of relativistic jet proper motions: lessons from Galactic microquasars". In: MNRAS 340, pp. 1353–1358. URL: http://adsabs.harvard.edu/abs/2003MNRAS.340.1353F (cit. on p. 70).

Fender, R. P., J. Homan, and T. M. Belloni (2009). "Jets from black hole X-ray binaries: testing, refining and extending empirical models for the coupling to X-rays". In: *MNRAS* 396, pp. 1370–1382 (cit. on p. 72).

Fender, R. et al. (2004). "An ultra-relativistic outflow from a neutron star accreting gas from a companion". In: *Nature* 427, pp. 222–224 (cit. on p. 85).

Fermi, ENRICO (Apr. 1949). "On the Origin of the Cosmic Radiation". In: *Phys. Rev.* 75 (8), pp. 1169–1174 (cit. on p. 8).

Gaisser, T. K., F. Halzen, and T. Stanev (1995). "Particle astrophysics with high energy neutrinos". In: *Phys. Rep.* 258, pp. 173–236 (cit. on p. 10).

Gallo, E., S. Corbel, et al. (2004). "A transient large-scale relativistic radio jet from GX 339-4". In: *MNRAS* 347 (cit. on p. 88).

Gallo, E., R. P. Fender, and G. G. Pooley (2003). "A universal radio-X-ray correlation in low/hard state black hole binaries". In: MNRAS 344, pp. 60–72 (cit. on p. 72).

Gehrels, N. et al. (Aug. 2004). "The Swift Gamma-Ray Burst Mission". In: ApJ 611, pp. 1005–1020 (cit. on p. 78).

Giacconi, R. et al. (June 1967). "An X-Ray Survey of the Cygnus Region". In: ApJ 148, p. L119 (cit. on p. 95).

Ginzburg, V. L. and S. I. Syrovatskii (1964). *The origin of cosmic rays*. London: Pergamon (cit. on p. 10).

Giuliani, A. et al. (Dec. 2011). "Neutral Pion Emission from Accelerated Protons in the Supernova Remnant W44". In: ApJ 742, L30, p. L30 (cit. on p. 11).

Gregory, P. C. and P. P. Kronberg (Oct. 1972). "Discovery of Giant Radio Outburst from Cygnus X-3". In: Nature 239, pp. 440–443 (cit. on p. 95).

Greisen, K. (Apr. 1966). "End to the Cosmic-Ray Spectrum?" In: *Physical Review Letters* 16, pp. 748–750 (cit. on pp. 1, 5).

Grimm, H.-J., M. Gilfanov, and R. Sunyaev (Sept. 2002). "The Milky Way in X-rays for an outside observer. Log(N)-Log(S) and luminosity function of X-ray binaries from RXTE/ASM data". In: A&A 391, pp. 923–944 (cit. on p. 60).

Halladjian, G. (2010). "Recherche de neutrinos cosmiques de haute-énergie émis par des sources ponctuelles avec ANTARES". PhD thesis. Université de la méditérranée Aix-Marseille II (cit. on p. 118).

Hanlon, W. (2008). "The energy spectrum of ultra high energy cosmic rays measured by the high resolution Fly's Eye observatory in stereoscopic mode". PhD thesis. University of Utah (cit. on p. 4).

Hasinger, G. and M. van der Klis (Nov. 1989). "Two patterns of correlated X-ray timing and spectral behaviour in low-mass X-ray binaries". In: A&A 225, pp. 79–96 (cit. on p. 72).

Heck, D. et al. (Feb. 1998). *CORSIKA: a Monte Carlo code to simulate extensive air showers.* Ed. by Heck, D., Knapp, J., Capdevielle, J. N., Schatz, G., & Thouw, T. (cit. on p. 39).

Heijboer, A. (2004). "Track Reconstruction and Point Source Search with ANTARES". PhD thesis. Universiteit van Amsterdam (cit. on pp. 44, 101, 108).

Hess, V. F. (1912). "Über Beobachtungen der durchdringenden Strahlung bei sieben Freiballonfahrten." In: *Phys. Zeit.* 13, p. 1084 (cit. on p. 3).

Hörandel, J. R. (2004). "Models of the knee in the energy spectrum of cosmic rays". In: *Astroparticle Physics* 21, pp. 241–265 (cit. on p. 5).

Hunstead, D. et al. (2009). *ATel 1960* (cit. on p. 89).

Hynes, R. I. et al. (Feb. 2003). "Dynamical Evidence for a Black Hole in GX 339-4". In: ApJ 583, pp. L95–L98 (cit. on p. 88).

— (July 2004). "The Distance and Interstellar Sight Line to GX 339-4". In: ApJ 609, pp. 317–324 (cit. on p. 88).

Ingelman, G., A. Edin, and J. Rathsman (Apr. 1997). "LEPTO 6.5 - A Monte Carlo generator for deep inelastic lepton-nucleon scattering". In: *Computer Physics Communications* 101, pp. 108–134 (cit. on p. 37).

James, F. (2006). *Statistical Methods in Experimental Physics: 2nd Edition.* Ed. by James, F. World Scientific Publishing Co (cit. on p. 107).

Jonker, P. G. et al. (2010). "Following the 2008 outburst decay of the black hole candidate H 1743-322 in X-ray and radio". In: *MNRAS* 401, pp. 1255–1263 (cit. on p. 92).

Kalemci, E. et al. (2007). *ATel 1348 and references therein* (cit. on p. 92).

Kaluzienski, L. J. and S. S. Holt (Aug. 1977). "Variable X-Ray Sources". In: IAU Circ. 3099, p. 3 (cit. on p. 91).

Kaluzienski, L. J., S. S. Holt, et al. (Sept. 1976). "Evidence for a 16.6 day period from Circinus X-1". In: ApJ 208, pp. L71–L75 (cit. on p. 85).

Kennea, J. A. and F. Capitanio (2007). *ATel 1140* (cit. on p. 92).

Klein, S. R. (June 2009). "IceCube: A Cubic Kilometer Radiation Detector". In: *IEEE Transactions on Nuclear Science* 56, pp. 1141–1147 (cit. on p. 21).

Klimushin, S. I., E. V. Bugaev, and I. A. Sokalski (2001). "Precise parametrizations of muon energy losses in water." In: *International Cosmic Ray Conference*. Vol. 3. International Cosmic Ray Conference, p. 1009 (cit. on p. 16).

Kopper, C. (2010). "Performance Studies for the KM3NeT Neutrino Telescope". PhD thesis. Friedrich-Alexander-Universit at Erlangen-Nurnberg (cit. on p. 51).

Krimm, H. A. (2006). *ATel 968* (cit. on p. 89).

Kuulkers, E. et al. (Apr. 2003). "Igr J17091-3624". In: *The Astronomer's Telegram* 149, p. 1 (cit. on p. 92).

Lauqué, R., J. Lequeux, and Nguyen-Quang-Rieu (Jan. 1973). "Cygnus X-3-21-cm absorption reexamined". In: Nature 241, p. 94 (cit. on p. 95).

Levine, A. M. et al. (Sept. 1996). "First Results from the All-Sky Monitor on the Rossi X-Ray Timing Explorer". In: ApJ 469, p. L33 (cit. on p. 78).

Levinson, A. and E. Waxman (Oct. 2001). "Probing Microquasars with TeV Neutrinos". In: *Physical Review Letters* 87.17, 171101, p. 171101 (cit. on pp. 12, 74, 122, 124).

Linares, M. et al. (Aug. 2010). "The Return of the Bursts: Thermonuclear Flashes from Circinus X-1". In: ApJ 719, pp. L84–L89 (cit. on p. 85).

Ling, Z., S. N. Zhang, and S. Tang (Apr. 2009). "Determining the Distance of Cyg X-3 with its X-Ray Dust Scattering Halo". In: ApJ 695, pp. 1111–1120 (cit. on p. 95).

Linsley, J. (Feb. 1963). "Evidence for a Primary Cosmic-Ray Particle with Energy 10^{20} eV". In: *Physical Review Letters* 10, pp. 146–148 (cit. on p. 3).

Liu, Q. Z., J. van Paradijs, and E. P. J. van den Heuvel (2006). "Catalogue of high-mass X-ray binaries in the Galaxy (4th Edition)". In: A&A 455, pp. 1165–1168 (cit. on p. 61).

— (2007). "A catalogue of low-mass X-ray binaries in the Galaxy, LMC, and SMC (Fourth Edition)". In: A&A 469, p. 807 (cit. on p. 61).

Longair, M. S. (1992). *High Energy Astrophysics*. Cambridge U.K.: Cambridge University Press (cit. on pp. 8, 67).

Mannheim, K. (1993). "The proton blazar". In: *Astron. & Astrophys.* 269, pp. 67–76 (cit. on p. 12).

Markert, T. H. et al. (Sept. 1973). "Observations of the Highly Variable X-Ray Source GX 339-4". In: ApJ 184, p. L67 (cit. on p. 88).

Marshall, H. L., C. R. Canizares, and N. S. Schulz (Jan. 2002). "The High-Resolution X-Ray Spectrum of SS 433 Using the Chandra HETGS". In: ApJ 564, pp. 941–952 (cit. on p. 70).

Martí, J., J. M. Paredes, and M. Peracaula (Aug. 2001). "Development of a two-sided relativistic jet in Cygnus X-3". In: A&A 375, pp. 476–484 (cit. on p. 95).

McClintock, J. E. and R. A. Remillard (2006). "Compact Stellar X-ray Sources". In: ed. WHG Lewin, M van der Klis, Cambridge Univ. Chap. 4 (cit. on p. 71).

McClintock, J. E., R. A. Remillard, et al. (June 2009). "The 2003 Outburst of the X-Ray Transient H1743-322: Comparisons with the Black Hole Microquasar XTE J1550-564". In: ApJ 698, pp. 1398–1421 (cit. on p. 91).

Meier, D. L., S. Koide, and Y. Uchida (Jan. 2001). "Magnetohydrodynamic Production of Relativistic Jets". In: *Science* 291, pp. 84–92 (cit. on p. 69).

Migneco, E. et al. (Nov. 2006). "Status of NEMO". In: *Nuclear Instruments and Methods in Physics Research A* 567, pp. 444–451 (cit. on p. 33).

Mirabel, I. F. et al. (Mar. 1997). "The Superluminal Source GRS 1915+105: A High Mass X-Ray Binary?" In: ApJ 477, p. L45 (cit. on p. 70).

Mirabel, I. F. (2004). "The AGN-MICROQUASAR-GRB connection". In: *35th COSPAR Scientific Assembly*. Ed. by J.-P. Paillé. Vol. 35, p. 1027 (cit. on p. 59).

Mirabel, I. F. and L. F. Rodríguez (1992). "A double sided radio jet from the compact Galactic Centre annihilator 1E1740.7-2942". In: Nature 358, pp. 215–217 (cit. on p. 59).

— (1994). "A superliminal source in the Galaxy". In: Nature 371, pp. 46–48 (cit. on pp. 59, 68).

Moffat, A. F. J. et al. (1988). "Spectroscopic evidence for rapid blob ejection in Wolf-Rayet stars". In: *ApJ* 334, pp. 1038–1043 (cit. on p. 64).

Moin, A. et al. (2011). "e-VLBI observations of Circinus X-1: monitoring of the quiescent and flaring radio emission on au scales". In: *MNRAS* 414, pp. 3551–3556 (cit. on p. 85).

Motta, S., T. Belloni, and J. Homan (2009). "The evolution of the high-energy cut-off in the X-ray spectrum of GX 339-4 across a hard-to-soft transition". In: *MNRAS* 400, pp. 1603–1612 (cit. on p. 89).

Motta, S., T. Belloni, T. Muñoz-Darias, et al. (2010). *ATel 2593* (cit. on p. 89).

Murdin, P. et al. (July 1980). "Binary model of Circinus X-1. I - Eccentricity from combined X-ray and radio observations". In: A&A 87, pp. 292–298 (cit. on p. 85).

Nakahira, S. et al. (2010). *ATel 2774* (cit. on p. 92).

Navas, S. and L. Thompson (1999). *ANTARES-SOFT-1999-011, ANTARES internal note* (cit. on p. 39).

Neyman, J. and E. S. Pearson (1933). "On the Problem of the Most Efficient Tests of Statistical Hypotheses". In: *Royal Society of London Philosophical Transactions Series A* 231, pp. 289–337 (cit. on p. 108).

Nicolson, G. D. (2007). *ATel 985* (cit. on p. 86).

Pandey, M. et al. (Feb. 2006). "GMRT observations of the field of INTEGRAL X-ray sources - I". In: A&A 446, pp. 471–483 (cit. on p. 92).

Parsignault, D. R. et al. (Oct. 1972). "Observations of Cygnus X-3 by Uhuru". In: Nature 239, p. 123 (cit. on p. 95).

Piran, T. (June 1999). "Gamma-ray bursts and the fireball model". In: Phys. Rep. 314, pp. 575–667 (cit. on p. 12).

Porcas, R. W. (1987). "Summary of known superluminal sources". In: *Superluminal Radio Sources*. Ed. by J. A. Zensus & T. J. Pearson, pp. 12–25 (cit. on p. 68).

Presani, E. (2011). "Neutrino Induced Showers From Gamma-Ray Bursts". PhD thesis. Universiteit van Amsterdam (cit. on p. 57).

Puls, J., J. S. Vink, and F. Najarro (2008). "Mass loss from hot massive stars". In: *A&A Rev.* 16, pp. 209–325 (cit. on pp. 62, 63).

Rees, M. J. (July 1966). "Appearance of Relativistically Expanding Radio Sources". In: Nature 211, pp. 468–470 (cit. on p. 68).

Rodriguez, J. et al. (2011). *(in prep.)* (Cit. on p. 94).

Romero, G. E. et al. (2003). "Hadronic gamma-ray emission from windy microquasars". In: *AAP* 410, pp. L1–L4 (cit. on pp. 12, 74).

Rupen, M. P., A. J. Mioduszewski, and V. Dhawan (Apr. 2003). "Possible radio counterpart to IGR J17091-3624". In: *The Astronomer's Telegram* 152, p. 1 (cit. on p. 92).

Rybicki, G. B. and A. P. Lightman (1979). *Radiative processes in astrophysics*. New York, Wiley-Interscience, 1979. 393 p. (cit. on p. 66).

Sabatini, S. et al. (2010). "Episodic Transient Gamma-ray Emission from the Microquasar Cygnus X-1". In: ApJ 712, pp. L10–L15 (cit. on p. 73).

Saito, T. Y. et al. (July 2009). "Microquasar observations with the MAGIC telescope". In: *ArXiv e-prints* (cit. on p. 73).

Scapparone, E. (Feb. 1999). "HEMAS: a Monte Carlo code for hadronic, electromagnetic and TeV muon components in air shower". In: *ArXiv Physics e-prints* (cit. on p. 39).

Schein, M., W. P. Jesse, and E. O. Wollan (Apr. 1941). "The Nature of the Primary Cosmic Radiation and the Origin of the Mesotron". In: *Physical Review* 59, pp. 615–615 (cit. on p. 3).

Shakura, N. I. and R. A. Sunyaev (1973). "Black holes in binary systems. Observational appearance." In: *A&A* 24, pp. 337–355 (cit. on p. 64).

Shidatsu, M. et al. (Nov. 2011). "X-Ray and Near-Infrared Observations of GX 339-4 in the Low/Hard State with Suzaku and IRSF". In: PASJ 63, p. 785 (cit. on p. 88).

Simpson, J. A. (1983). "Elemental and Isotopic Composition of the Galactic Cosmic Rays". In: *Annual Review of Nuclear and Particle Science* 33, pp. 323–382 (cit. on p. 6).

Stanev, T. et al. (2000). "Propagation of ultrahigh energy protons in the nearby universe". In: *Phys. Rev. D* 62.9, p. 093005 (cit. on p. 7).

Steiner, J. F., J. E. McClintock, and M. J. Reid (Jan. 2012). "The Distance, Inclination, and Spin of the Black Hole Microquasar H1743-322". In: ApJ 745, L7, p. L7 (cit. on p. 91).

Still, M., C. Brocksopp, and P. Casella (2009). *ATel 1954* (cit. on p. 89).

Strohmayer, T. and L. Bildsten (2006). "Compact Stellar X-ray Sources". In: ed. WHG Lewin, M van der Klis, Cambridge Univ. Chap. 3 (cit. on p. 60).

Strom, R. G., J. van Paradijs, and M. van der Klis (Jan. 1989). "Discovery of a double radio source associated with Cygnus X-3". In: Nature 337, pp. 234–236 (cit. on p. 95).

Sunyaev, R. A. and L. G. Titarchuk (June 1980). "Comptonization of X-rays in plasma clouds - Typical radiation spectra". In: *A&A* 86, pp. 121–138 (cit. on p. 66).

Tananbaum, H. et al. (Oct. 1972). "Observation of a Correlated X-Ray Transition in Cygnus X-1". In: ApJ 177, p. L5 (cit. on p. 92).

Tavani, M. et al. (2009). "Extreme particle acceleration in the microquasar CygnusX-3". In: Nature 462, pp. 620–623 (cit. on pp. 73, 97).

The KM3NeT Consortium (2010). *Technical Design Report for a Deep-Sea Research Infrastructure in the Mediterranean Sea Incorporating a Very Large Volume Neutrino Telescope, available at http://www.km3net.org/TDR/TDRKM3NeT.pdf* (cit. on pp. 33, 35).

van Kerkwijk, M. H. et al. (Feb. 1992). "Infrared helium emission lines from Cygnus X-3 suggesting a Wolf-Rayet star companion". In: Nature 355, pp. 703–705 (cit. on p. 95).

Véron-Cetty, M.-P. and P. Véron (Aug. 2006). "A catalogue of quasars and active nuclei: 12th edition". In: A&A 455, pp. 773–777 (cit. on p. 7).

Waxman, E. and J. Bahcall (1997). "High Energy Neutrinos from Cosmological Gamma-Ray Burst Fireballs". In: *Physical Review Letters* 78, pp. 2292–2295 (cit. on p. 12).

Webster, B. L. and P. Murdin (Jan. 1972). "Cygnus X-1-a Spectroscopic Binary with a Heavy Companion ?" In: Nature 235, pp. 37–38 (cit. on p. 92).

Wijers, R. A. M. J., M. J. Rees, and P. Meszaros (1997). "Shocked by GRB 970228: the afterglow of a cosmological fireball". In: *MNRAS* 288, pp. L51–L56 (cit. on p. 12).

Williams, P. K. G. et al. (2011). "The 2010 May Flaring Episode of Cygnus X-3 in Radio, X-rays, and γ-rays". In: ApJ 733, pp. L20+ (cit. on p. 97).

Yamaoka, K. et al. (2009). *ATel 2364 and references therein* (cit. on p. 92).

Zatsepin, G. T. and V. A. Kuz'min (Aug. 1966). "Upper Limit of the Spectrum of Cosmic Rays". In: *Soviet Journal of Experimental and Theoretical Physics Letters* 4, p. 78 (cit. on pp. 1, 5).

Zdziarski, A. A. et al. (July 2004). "GX 339-4: the distance, state transitions, hysteresis and spectral correlations". In: MNRAS 351, pp. 791–807 (cit. on p. 88).

Acknowledgements

This work would not have been possible without the kind and essential help and contribution of many people.

My thesis advisor, John Carr, certainly deserves the warmest thanks for having proposed me this exciting topic and for always being helpful: all of his suggestions have been of great value and his support essential for me to complete this work. A big and special thanks also goes to Damien Dornic for his invaluable help, for closely following me during the last period of my thesis and for being one of the referees of the analysis. Thank you Paschal, Vincent, Jürgen, Jean Pierre, Heide, Stephanie, Jose, Manuela, Colas and the whole ANTARES group at CPPM for letting me work in a stimulating and collaborative environment, for being a constant source of information about any slightest detail of the detector and for creating the working environment anybody dreams of. Also thanks to all the members of the ANTARES collaboration for the dynamic and inspiring atmosphere during each collaboration meeting and for always being helpful. In particular I would like to thank Thomas Eberl and Claudio Kopper for helping me stand during my first steps in understanding the SeaTray framework. Also thanks to Antoine Kouchner and Jörn Wilms for being the referees of this analysis. Thanks again to Jörn Wilms and Victoria Grinberg for discussions about X-ray binaries and Cyg X-1. A special thank to Carla Distefano for the discussions about the models for neutrino emission from microquasars.

I also would like to thank all the PhD students, postdocs, researchers and the whole personnel of CPPM for participating to the great atmosphere during pauses, coffee breaks and *pots*. This also was a great help!

I finally want to thank my family for their constant support and love. This thesis is dedicated to them.